OCM 2017

3rd INTERNATIONAL CONFERENCE ON

Optical Characterization of Materials

MARCH 22nd–23rd, 2017
KARLSRUHE | GERMANY

J. BEYERER | F. PUENTE LEÓN | T. LÄNGLE (Eds.)

KIT Scientific Publishing

Jürgen Beyerer | Fernando Puente León | Thomas Längle (eds.)

OCM 2017

3rd International Conference on Optical Characterization of Materials

March 22nd – 23rd, 2017
Karlsruhe | Germany

OCM 2017

3rd International Conference on Optical Characterization of Materials

March 22nd – 23rd, 2017
Karlsruhe | Germany

edited by
Jürgen Beyerer | Fernando Puente León | Thomas Längle

KIT Scientific Publishing

Veranstalter

Fraunhofer Institut of Optronics,
System Technologies and Image Exploitation IOSB
c/o Karlsruhe Center for Material Signatures KCM
Fraunhoferstraße 1, 76131 Karlsruhe

Dieser Tagungsband ist auch als Onlineversion abrufbar unter
http://dx.doi.org/10.5445/KSP/1000063696

Impressum

Karlsruher Institut für Technologie (KIT)
KIT Scientific Publishing
Straße am Forum 2
D-76131 Karlsruhe

www.ksp.kit.edu

Print on Demand 2017 – Gedruckt auf FSC-zertifiziertem Papier

ISBN 978-3-7315-0612-6
DOI 10.5445/KSP/1000063696

Preface

The state of the art in optical characterization of materials is advancing rapidly. New insights into the theoretical foundations of this research field have been gained and exciting practical developments have taken place, both driven by novel applications and innovative sensor technologies that are constantly emerging. The big success of the international conferences on Optical Characterization of Materials in 2013 and 2015 proves the necessity of a platform to present, discuss and evaluate the latest research results in this interdisciplinary domain. Due to that fact, the international conference on Optical Characterization of Materials (OCM) took place the third time in March 2017.

The OCM 2017 was organized by the Karlsruhe Center for Spectral Signatures of Materials (KCM) in cooperation with the German Chapter of the Instrumentation & Measurement Society of IEEE. The Karlsruhe Center for Spectral Signatures of Materials is an association of institutes of Karlsruhe Institute of Technology (KIT) and the business unit Automated Visual Inspection of the Fraunhofer Institute of Optronics, System Technologies and Image Exploitation IOSB.

Despite the conference's young age, the organizing committee has had the pleasure to evaluate a large amount of abstracts. Based on the submissions, we selected 20 talks complemented by 12 poster presentations and several practical demonstrations.

The present book is based on the conference held in Karlsruhe, Germany from March 22–23, 2017. The aim of this conference was to bring together leading researchers in the domain of Characterization of Materials by spectral characteristics from UV (240 nm) to IR (14 µm), multispectral image analysis, X-ray methods, polarimetry, and microscopy. Typical application areas for these techniques cover the fields of, e.g., food industry, recycling of waste materials, detection of contaminated materials, mining, process industry, and raw materials.

The editors would like to thank all of the authors that have contributed to these proceedings as well as the reviewers, who have invested a generous amount of their time to suggest possible improve-

ments of the papers. The help of Henning Schulte and Johannes Meyer in the preparation of this book is greatly appreciated. Last but not least, we thank the organizing committee of the conference, led by Britta Ost, for their effort in organizing this event. The excellent technical facilities and the friendly staff of the Fraunhofer IOSB greatly contributed to the success of the meeting.

March 2017

Jürgen Beyerer
Fernando Puente León
Thomas Längle

General Chairs

Prof. Dr.-Ing. habil. J. Beyerer	Fraunhofer IOSB Karlsruhe
Prof. Dr.-Ing. F. Puente León	Karlsruhe Institute of Technology

Program Chair

apl. Prof. Dr.-Ing. T. Längle	Karlsruhe

Program Committee

M. Sc. S. Bauer	Karlsruhe
Dr. M. Bücking	Schmallenberg
Dr.-Ing. R. Gruna	Karlsruhe
Prof. Dr.-Ing. M. Heizmann	Karlsruhe
Prof. Dr.-Ing. O. Kanoun	Chemnitz
Prof. Dr.-Ing. habil. H. Z. Kuyumcu	Berlin
M. Sc. J. Meyer	Karlsruhe
Dipl.-Ing. D. Nüßler	Wachtberg
Dr. R. Ostertag	Würzburg
Prof. Dr.-Ing. T. Pretz	Aachen
Dipl.-Inf. M. Richter	Karlsruhe
Prof. Dr. F. Salazar Bloise	Madrid
Dr. H. Schmidt	Kulmbach
Dipl.-Ing. Dipl.-Wirt.-Ing. H. Schulte	Karlsruhe
Dr.-Ing. M. Taphanel	Karlsruhe
Prof. Dr.-Ing. H. Wotruba	Aachen
Prof. Dr. B. Zagar	Linz

Contents

Spectral Data Processing

Spectral Applications

Recycling and Environment

Employing NIR-SWIR hyperspectral imaging to predict the smokiness of scotch whisky

Julius Tschannerl[1], Jinchang Ren[1,3], Frances Jack[2], Stephen Marshall[1] and Huimin Zhao[3,4]

[1] University of Strathclyde, Hyperspectral Imaging Centre, Dept of EEE 16 Richmond St, Glasgow G1 1XQ, UK
[2] Scotch Whisky Research Institute, The Robertson Trust Building, Research Avenue North, EH14 4AP Edinburgh, UK
[3] Guangzhou Key Laboratory of Digital Content Processing and Security Technologies, Guangzhou, 510665, China
[4] School of Electronic Information, Guangdong Polytechnic Normal University, Guangzhou, China

Abstract Scotch Whisky makes a significant contribution to the UK's food and drinks export. The flavour of this high quality spirit is derived naturally from the whisky making process, with smoky aromas being a key character of certain Scotch whiskies. The level of smokiness is determined by the amount of phenolic compounds in the spirit. Phenols are introduced by exposing the barley malt to peat smoke during the kilning process. The current techniques to determine the levels of phenols, such as High Performance Liquid Chromatography (HPLC), are time consuming as they require distillation of the malt prior to analysis. To speed up this process and enable real-time detection before processing, the possibilities of Near-infrared to Short-wave-infrared (NIR-SWIR) Hyperspectral Imaging (HSI) to detect these phenols directly on malted barley are explored. It can be shown that via regression analysis, various levels of phenol concentration used as working levels for whisky production could be estimated to a satisfying degree. To further optimise industrial application, a hyperspectral band selection algorithm is applied that yields good results and reduces computational cost and may open possibilities to employ multispectral rather than hyperspectral cameras in future applications.

Keywords: Hyperspectral imaging, scotch whisky, near-infrared.

1 Introduction

Over the last couple of years, an increasing interest in Hyperspectral Imaging (HSI) for applications other than remote sensing can be observed. Applications include e.g. food inspection [1], medical applications [2] and artwork inspection [3]. The main reason for its popularity is its rapid data acquisition and the non-destructive nature of the same. As opposed to regular spectroscopy techniques, data is acquired at a relatively high frame rate incorporating not only spectral but also spatial information. HSI is able to gain information about the chemical composition of the imaged objects without altering the integrity of the objects. The potential as a non-destructive, real-time chemical analysis technique stirs an increasing industrial interest in HSI as it can be seemlessly integrated into the processing chain.

Scotch whisky is a high quality spirit drink exclusively produced in Scotland in a manner specified by law. According to data collected by the Scotch Whisky Association from January to December 2014, 99 million cases of 12 40 % vol. bottles were exported which made up around a quarter of the UK food and drink exports [4]. These figures justify a high interest in maintaining its high quality standards.

One distinct feature of certain Scotch Whiskies are their smoky characteristics. Large parts of Scotland are covered by peat bogs. Dried peat has a long history of being used as a fuel in Scotland. Exposing malted barley that is used for whisky production during the kilning process to the smoke of burning peat introduces the typical smoky aroma. The smoking process can be seen in Figure 1.1. Phenolic compounds in the smoke adhere to the surface of the grain and carry through the process into the spirit. The phenol levels are used as a marker to the degree of smokiness of whisky. The following eight phenolic compounds can be found in scotch whisky. Phenol, Guaiacol, m/p-Cresol, o-Cresol, 4-Methyl-Guaiacol, 4-Ethyl Guaiacol and 4-Ethyl Phenol. The levels are measured in mg/kg or ppm respectively and measured is the total number, i.e. the sum of the concentrations of the individual compounds. Phenol levels are varied depending on desired smokiness. It is important from a flavour point of view to be able to control these levels, to avoid having to blend final spirits to obtain the aroma required. Measuring the levels of phenols in malt currently requires a pre-processing step. The malted barley is finely ground, water added

(a) (b)

Figure 1.1: (a) Burning peat (b) Barley being exposed to peat smoke.

and then steam distilled. The levels of phenols in the distillate are measured using High Performance Liquid Chromatography (HPLC) or other colorimetric methods. It would be of significant benefit to the whisky industry to be able to determine the phenol levels directly in the malted barley, before any processing has been applied.

Phenolic compounds in grapes have previously successfully been detected by HSI [5]. This work aims to explore possibilities of determining phenol levels in malted barley by means of Near-infrared to Shortwave-infrared (NIR-SWIR) HSI in a potentially industry based application. In addition to a detection before processing of the malt, HSI offers a potential real-time detection of phenol levels, whereas HPLC needs at least a couple of days in a lab to be performed. To show this, the following things are explored in this study: By means of HSI and multivariate data analysis, it is attempted to determine different levels of phenol concentration in barley malt. To further optimise the process for industrial application, a band selection algorithm is evaluated for suitability on this data that enables faster processing and multispectral data acquisition in future applications.

2 Sample preparation and data acquisition

As mentioned above, the peatiness of the barley is measured in ppm. This study looked initially at difference between extreme samples; unpeated malt with 0 ppm phenols versus heavily peated malt containing 120–130 ppm total phenols. The desired working levels for the actual whisky production ranges from 0 to about 50 ppm where these levels are usually divided into three classes as follows:

1. **Lightly peated:** 1 – 5 ppm
2. **Medium peated:** 6 – 15 ppm
3. **Heavily peated:** 16 – 50 ppm

These levels are created by mixing unpeated barley malt with the very heavily peated to equivalent parts. The concentration of the very heavily peated malt is determined by HPLC. Where HPLC measures the average concentration of phenols in a batch of barley grains, HSI can only measure spectra on various spatial points. As seen in Figure 1.1, the barley is spread out in a large pool and smoked from below and each individual grain is exopsed to the smoke to a different degree. The amount of phenols that adhere to the surface also vary within one grain depending on its orientation and batches with a low amount of phenols only include very little grains with phenols on the surface. This needs to be considered when measuring the concentration with an imaging device as only the surface of the grains can be measured.

For initial tests of detectability, a batch of grains with no phenols and barley with a concentration of about 120 ppm have been produced and imaged. Three different batches of barley with 3, 12 and 30 ppm have then been created to cover the three working levels of phenols. The barley has been placed in a tray as seen in Figure 1.2 and imaged with a pushbroom NIR-SWIR HSI camera. The camera has a spectral range of 900 – 1700 nm and scans 320 pixels with 256 bands per line. The samples have been illuminated with two halogen lightbulbs on each side which have been diffused to minimise specular reflections and shadows. However, due to the curved surface of the grains, differences in intensity and different spectral reflections cannot be completely avoided. Six different samples of each level have been imaged. Since the measured phenols will most likely vary strongly between the

pixels, the mean of subsets of all pixels per sample was taken. The subsets consist of randomly selected pixels within each samples to avoid localised effects of phenol accumulation or absence. 50 subsets per sample have been generated, resulting in 300 observations per phenol level.

3 Spectral pre-processing

To compensate for variations in the lighting between different samples and spatial variations along the scanned line, the raw measured signal **S** can be calibrated and converted to percent reflectance spectra **R** with the following formula, shown in [6]:

$$\mathbf{R} = \frac{\mathbf{S} - \mathbf{D}}{\mathbf{W} - \mathbf{D}} \times 100\,\% \tag{1.1}$$

D is a dark current image acquired by minimising the camera's sensor exposure to any radiation. This is to estimate the sensor's shot noise. **W** is a white reference imaged acquired by imaging e.g. a Spectralon plaque which exposes almost lambertian scattering over the desired spectral range. This helps to approximate the maximum reflectance measured at each wavelength.

A number of spectral pre-processing techniques have been analysed in [7] for NIR spectra including various techniques for de-noising [8]. Most popular ones include conversion to Standard Normal Variate (SNV) and 1st and 2nd derivatives using Savitzky-Golay filters. SNV transforms the data to zero mean and unit variance. This removes an additive baseline and can in theory be used to compensate for slight intensity variations due to shadow effects on uneven surfaces and compensate for scattering effects [7]. In practice however, no general optimal pre-processing procedure can be established and most researchers try various combinations and use the ones that yield the best results for the specific application. In this case, pre-treatment with SNV yielded the best regression results, as is later shown in Section 5.

The SNV of a reflectance spectrum $\mathbf{R}$ is defined as follows:

$$\mathbf{R}_{SNV} = \frac{\mathbf{R} - \boldsymbol{\mu}}{\sigma} \tag{1.2}$$

where $\boldsymbol{\mu}$ represents the mean and σ the standard deviation of all measured spectra.

4 Band selection

One major disadvantage of hyperspectral data is its high dimensionality. While it is often desired to maintain a relatively high spatial resolution for optimal identification of the measured objects, the spectral information can in most cases be reduced. Hyperspectral cameras cover a wide, continuous range of spectral bands but in many applications, only certain wavelengths are of particular interest. Additonally, adjacent bands usually carry redundant information and the well known curse of dimensionality may even decrease the discriminability if too many bands are included. Different feature extraction techniques [9–11], predominantly Principal Component Analysis (PCA) and variations [12] have widely been successfully applied to hyperspectral data to reduce the dimensionality. The disadvantage of feature extraction however is that new features are generated by e.g linearly combining spectral bands and the resulting features are no longer physically interpretable and linked to specific chemical properties of the imaged objects.

Various feature selection techniques have been developed over the last decades [13] that try to select an optimal subset of features for a specific application. In [14] a new unsupervised band selection algorithm for hyperspectral images is introduced. Based on information theory, the following criterion is defined to evaluate the fitness of a selected subset of features:

$$\max \left(\sum_{m=1}^{s} H(X_{i_m}) - \frac{2}{s-1} \sum_{1 \le m_1 < m_2 \le s} I(X_{i_{m_1}}; X_{i_{m_2}}) \right) \tag{1.3}$$

where s is the number of desired features, $H(X_{i_m})$ the entropy of the mth feature in the subset X_i and $I(X_{i_{m_1}}; X_{i_{m_2}})$ the mutual information

between the two features. The criterion maximises the information carried by each feature in the subset individually while minimising the redundant information carried by the whole subset. The criterion is therefore called Maximum-Information-Minimum-Redundancy (MIMR). To optimise the maximisation function, an adapted version of the Clonal Selection Algorithm (CSA) is employed as a heuristic. As shown in [14], the MIMR-CSA algorithm outperforms state of the art algorithms in classification applications for hyperspectral remote sensing data. Its suitability for regression is to be tested here.

5 Data analysis and results

To visually inspect if there are any spectral differences in the NIR detectable, three batches of unpeated malt and heavily peated barley with a phenol concentration of about 120 ppm have been imaged and the mean spectra pre-processed with SNV have been plotted. This can be seen in Figure 1.2. The spectra show a very similar shape but differ in intensity in some spectral regions, especially in bands between 950 and 1120 nm. These differences are likely to be the result of slight shift into "red" of the peated barley. The smoked grains tend to be a bit more brown than the unsmoked grains.

Support Vector machines have been applied successfully to HSI data for classification in the past [15] and new techniques including multi-kernel learning [16] and deep-learning based approaches [17] show that there is more potential for improved algorithms. To estimate the phenol concentration, Support Vector Regression (SVR) has been applied. SVR has been chosen as it has shown good results for regression analysis on hyperspectral data in the past [18–20], is especially capable of handling non-linearities within the data [21] and only needs a relatively small training data set to deliver robust results [22]. A Radial Basis Function kernel (RBF) has been used whose parameters have been tuned via grid search. The goal here is not to determine the most effective regression method but to prove the feasibility of phenol level estimation through regression analysis. Although the division of phenol concentrations in three levels would imply a classification approach, future applications may include a more detailed estimation of the concentration rather than grouping it in high, medium and low levels. Thus,

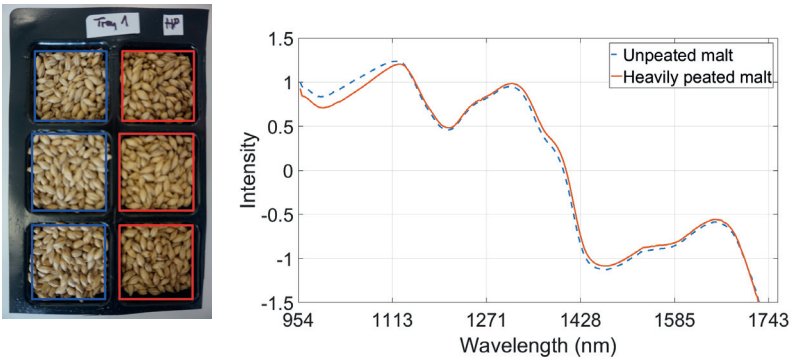

(a) (b)

Figure 1.2: (a) Barley samples. Unpeated grains are on the left column and very heavily peated on the right. (b) Spectra acquired by taking the mean over all three samples of each class and applying SNV as pre-treatment.

it is to determine the effectiveness of regression for this application. To evaluate the regression results, the Coefficient of Determination (r^2) has been calculated as follows:

$$r^2 = 1 - \frac{\sum_{i=1}^{n}(y_i - \hat{y}_i)^2}{\sum_{i=1}^{n}(y_i - \bar{y}_i)} \tag{1.4}$$

where y_i is the actual value, $\hat{y}_i$ the predicted value, $\bar{y}_i$ the mean of all original values and n the number of samples. Additionally, the Root Mean Squared Error (RMSE) has been calculated. A 20/80 % training/testing set has been used and split randomly. To compensate for statistic variations between the selected training sets, this process has been repeated 10 times. MIMR-CSA has been applied with an increasing number of features starting from two to 256. MIMR-CSA has been applied three times on each of those selected sets resulting in a total number of 30 repetitions per number of selected features. The results of the regression can be seen in Figure 1.3.

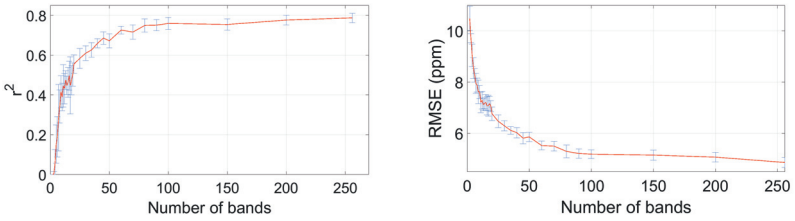

Figure 1.3: Regression results with increasing amount of selected features for phenol level prediction with SVR. (a) r^2 values stabilise around a value of 0.77 (b) The RMSE stabilises around a value of around 5 ppm.

6 Conclusion and future work

While it could be shown that some spectral differences between peated and unpeated barley can be detected with NIR-SWIR HSI, it is not yet clear if these differences derive from chemical absorption of the phenol, from physical scattering or from colour differences. Scattering effects have been tried to be minimised via spectral pre-processing. It could be shown that the measured spectra of three different phenol levels can to a certain extent be detected via regression analysis. It is likely that the differences detected are caused by colour information rather than spectral absorption of the phenols, but this cannot be verified at this stage. These three levels represent general working levels for whisky production. A minimum RMSE of about 5ppm is still a relatively high number considering the working range of the three classes. Additional samples, especially in more levels of concentration in between the current ones are likely to decrease this value. Applying a state-of-the-art band selection algorithm for hyperspectral data on this dataset showed that most information needed for regression lies in only about 75 of the 256 bands. This number is still too high for determining selected bands for a multispectral camera, but the computational cost can be drastically reduced. The presented results encourage us to put more work into the phenol detection via HSI.

7 Acknowledgements

This work is partially funded by the Institute of Brewing and Distilling. The images in Figure 1.1 are courtesy of the Scotch Whisky Research Institute.

References

1. D.-W. Sun, *Hyperspectral imaging for food quality analysis and control*. Academic, 2010.
2. G. Lu and B. Fei, "Medical hyperspectral imaging: a review." *Journal of biomedical optics*, vol. 19, no. 1, p. 10901, 2014.
3. A. Polak, T. Kelman, P. Murray, S. Marshall, D. J. Stothard, N. Eastaugh, and F. Eastaugh, "Use of infrared hyperspectral imaging as an aid for paint identification," *Journal of Spectral Imaging*, vol. 5, no. 1, pp. 1–10, 2016.
4. Scotch Whisky Association. (2015) Facts & Figures. Accessed: 09/12/2016. [Online]. Available: http://www.scotch-whisky.org.uk/what-we-do/facts-figures/
5. M. J. Jara-Palacios, F. J. Rodríguez-Pulido, D. Hernanz, M. L. Escudero-Gilete, and F. J. Heredia, "Determination of phenolic substances of seeds, skins and stems from white grape marc by near-infrared hyperspectral imaging," *Australian Journal of Grape and Wine Research*, vol. 22, no. 1, pp. 11–15, 2016.
6. H. Yao and D. Lewis, "Spectral Preprocessing and Calibration Techniques," in *Hyperspectral Imaging for Food Quality Analysis and Control*, 2010, pp. 45–78.
7. Å. Rinnan, F. van den Berg, and S. B. Engelsen, "Review of the most common pre-processing techniques for near-infrared spectra," pp. 1201–1222, 2009.
8. T. Qiao, J. Ren, Z. Wang, J. Zabalza, M. Sun, H. Zhao, S. Li, J. A. Benediktsson, Q. Dai, and S. Marshall, "Effective Denoising and Classification of Hyperspectral Images Using Curvelet Transform and Singular Spectrum Analysis," *IEEE Transactions on Geoscience and Remote Sensing*, vol. 55, no. 1, pp. 119–133, 2016.
9. J. Ren, J. Zabalza, S. Marshall, and J. Zheng, "Effective feature extraction and data reduction in remote sensing using hyperspectral imaging [Applications Corner]," *IEEE Signal Processing Magazine*, vol. 31, no. 4, pp. 149–154, 2014.

10. J. Zabalza, J. Ren, J. Zheng, H. Zhao, C. Qing, Z. Yang, P. Du, and S. Marshall, "Novel segmented stacked autoencoder for effective dimensionality reduction and feature extraction in hyperspectral imaging," *Neurocomputing*, vol. 185, pp. 1–10, 2016.

11. J. Zabalza, J. Ren, J. Zheng, J. Han, H. Zhao, S. Li, and S. Marshall, "Novel Two-Dimensional Singular Spectrum Analysis for Effective Feature Extraction and Data Classification in Hyperspectral Imaging," *IEEE Transactions on Geoscience and Remote Sensing*, vol. 53, no. 8, pp. 4418–4433, 2015.

12. J. Zabalza, J. Ren, M. Yang, Y. Zhang, J. Wang, S. Marshall, and J. Han, "Novel Folded-PCA for improved feature extraction and data reduction with hyperspectral imaging and SAR in remote sensing," *ISPRS Journal of Photogrammetry and Remote Sensing*, vol. 93, pp. 112–122, 2014.

13. V. Kumar and S. Minz, "Feature Selection: A literature Review," *Smart Computing Review*, vol. 4, no. 3, pp. 211–229, 2014.

14. J. Feng, L. Jiao, F. Liu, T. Sun, and X. Zhang, "Unsupervised feature selection based on maximum information and minimum redundancy for hyperspectral images," *Pattern Recognition*, vol. 51, pp. 295–309, 2016.

15. F. Melgani and L. Bruzzone, "Classification of Hyperspectral Remote Sensing Images With Support Vector Machines," *IEEE Transactions on Geoscience and Remote Sensing*, vol. 42, no. 8, 2004.

16. L. Fang, S. Li, W. Duan, J. Ren, and J. A. Benediktsson, "Classification of Hyperspectral Images by Exploiting Spectral & Spatial Information of Superpixel via Multiple Kernels," *IEEE Transactions on Geoscience and Remote Sensing*, vol. 53, no. 12, pp. 6663–6674, 2015.

17. J. Han, D. Zhang, X. Hu, L. Guo, J. Ren, and F. Wu, "Background Prior-Based Salient Object Detection via Deep Reconstruction Residual," *IEEE Transactions on Circuits and Systems for Video Technology*, vol. 25, no. 8, pp. 1309–1321, 2015.

18. T. Qiao, J. Ren, C. Craigie, J. Zabalza, C. Maltin, and S. Marshall, "Quantitative prediction of beef quality using visible and nir spectroscopy with large data samples under industry conditions," *Journal of Applied Spectroscopy*, vol. 82, no. 1, 3 2015.

19. ——, "Singular spectrum analysis for improving hyperspectral imaging based beef eating quality evaluation," *Computers and Electronics in Agriculture*, vol. 115, pp. 21–25, 2015.

20. M. Sun, D. Zhang, Z. Wang, J. Ren, B. Chai, and J. Sun, "What's Wrong with the Murals at the Mogao Grottoes: A Near-Infrared Hyperspectral Imaging Method." *Scientific reports*, vol. 5, p. 14371, 2015.

21. I. Steinwart and A. Christmann, *Support vector machines*. Springer, 2008.
22. C. J. C. Burges, *Geometry and invariance in kernel based methods*. Cambridge, MA: MIT Press, 1999.

Simultaneous detection of melamine and urea in gluten with a handheld NIR scanner

Zoltan Kovacs[1,2], George Bazar[1,3], Behafarid Darvish[1], Frederik Nieuwenhuijs[4], Isabel Hoffmann[1]

[1] Tellspec Inc.
Toronto, Ontario, Canada
[2] Szent Istvan University
Budapest, Hungary
[3] Kaposvar University
Kaposvar, Hungary
[4] Meelunie B.V.
Amsterdam, The Netherlands

Abstract The standard analytical methods for the determination of total protein content, which is an important measure of quality in many food products, can be easily miss leaded by adding nitrogen deriving from different source driving to serious adulteration of the various foods. Therefore, there is an immense need to develop rapid method to detect multiple adulterations with handheld instruments. The objective of the present work is to develop multivariate models for simultaneous prediction of melamine and urea in wheat gluten samples with a handheld NIR scanner. Wheat gluten samples from ten different manufacturers from different part of the world were mixed with melamine and urea in different ratios to provide a robust enough sample set for spectral data acquisition. In spite of the natural separation based on the geographical origin of the gluten samples it was possible to build accurate models for simultaneous quantification of common food adulterants, melamine and urea, in multiple mixtures of gluten. The results show Tellspec Enterprise Food Sensor as a rapid, cost effective and user friendly tool can be used for the determination of melamine and urea adulteration in wheat gluten down to 1 % concentration.

Keywords: Adulteration, near infrared spectroscopy, principal component analysis, partial least square regression.

1 Introduction

Protein content is very important in many food products due to its high impact on the sensory and rheological characteristics, moreover, due to its nutritional value [1]. Therefore, total protein content has been used as a measure of quality of many raw, intermediate and final products in the food industry. Standard analytical methods for total protein determination are based on measurement of nitrogen content (e.g. Kjeldahl, Dumas), thus, cannot distinguish if nitrogen derives from different source [2,3]. This fact leads to adulteration of the various foods with nitrogen reach compounds. Urea and melamine are known to be commonly used adulterants which can cause intoxication as the example showed in China in 2008. The addition of these chemicals cannot be detected by the standard methods. There are available analytical methods such as gas chromatography (GC), high-performance liquid chromatography (HPLC) and more [4–6] to quantify the specific adulterants but these methods are specific, expensive and laborious. Therefore, the development of cost-effective and rapid measurement techniques to identify and quantify melamine and urea as food adulterants are desired [7]. Mid- (MIR) and near-infrared (NIR) spectroscopy was found as an effective tool to detect melamine in dairy products, such as infant formula, milk powder, or liquid milk [8]. Surface enhanced Raman spectroscopy was also showed to be applicable to screen foods and detect melamine contamination in wheat gluten, chicken feed, cakes and noodle with lower than 1 % accuracy [9]. NIR spectroscopy combined with PLS-DA was also used to identify the presence of melamine in milk [10]. Yang et al. [11] showed mid-infrared spectroscopy can be used to quantify urea with linear model due to its molecular fingerprint in mid-infrared region. Near-infrared Raman spectroscopy was presented as applicable method for quantitative determination of urea adulteration in milk [12]. Several reports show NIR spectroscopy has been successfully applied for the detection and quantification of simultaneous detection of mixed adulterations, too [13]. However, there is an immense need to develop rapid method to detect multiple adulterations with handheld instruments. The objective of the present work was to develop multivariate models for simultaneous prediction of melamine and urea in wheat gluten samples based on data acquired with handheld NIR scanners and a user friendly mobile app.

2 Materials and Methods

Wheat gluten samples from ten different manufacturers were mixed with melamine (M) and urea (U) in different ratios to get total contamination from 0 to 18 % based on the following; M:U = 1:1 in 1, 2, 5, 10, 18 %; M:U = 2:1 in 2, 5, 10, 15 %; M:U = 1:2 in 2, 5, 10, 15 %; only U in 0.5, 1, 2, 4, 8 %; and only M in 0.5, 1, 2, 4, 8 % concentration. Total number of samples analyzed was 219. The samples were stored and scanned in plastic bags. The NIR spectra of the samples were collected with two Tellspec Enterprise Food Sensor g1 scanners (scanner 1 and scanner 2) (Tellspec Inc., Toronto, Ontario, Canada) in several sessions acquiring multiple spectra per sample in each session, with 2 nm spectral step in the 950–1630 nm spectral interval. Various sample pre-processing methods and multivariate data analyses techniques were used to process the spectral data. Principal component analysis (PCA) [14] was used to describe multidimensional patterns of the data and to discover outliers. Partial least squares regression (PLSR) was used for quantitative models [15] to evaluate the relationship between the melamine or urea concentration and NIR spectra. The PLSR models were optimized for both scanners separately by using cross-validation, where data of single samples with their repeats were left out of the calibration and were used for validation, iteratively. Finally, the trained models of scanner 1 were tested with data of scanner 2, and vice versa, to achieve independent prediction.

3 Results and Discussion

Smoothed (Savitzky-Golay filter) and normalized average spectra of pure melamine, urea and wheat gluten samples were calculated and plotted to test the performance of the handheld NIR scanners for the detection of the absorption peaks of the tested main chemicals (Fig. 2.1).

Average absorbance spectrum of melamine shows peaks at 1021, 1473, 1494 and 1522 nm, while that of urea at 1031, 1231, 1305, 1413, 1470, 1499 and 1529 nm and of wheat gluten at 1029, 1205 and 1506 nm which is in a good harmony with the results available in the corresponding references [16–18].

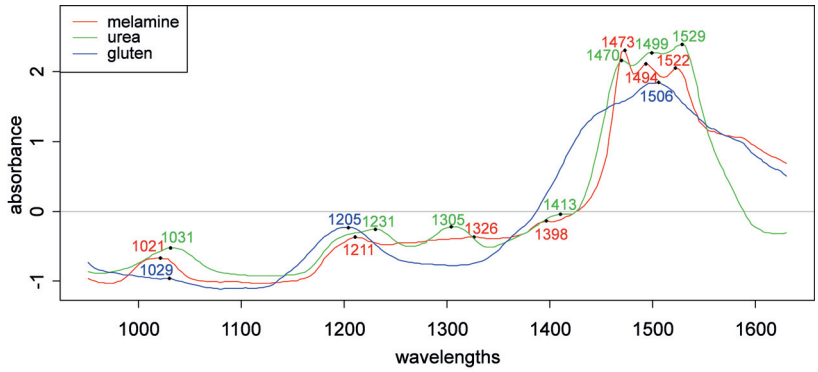

Figure 2.1: Smoothed (Savitzky-Golay filter) and normalized average spectra of pure melamine ($n_{melamine}$ = 50), urea (n_{urea} = 50) and wheat gluten (n_{gluten} = 1675) samples acquired with scanner 1 with their assigned absorption peaks.

The calculation of PCA models were performed both merging the data of scanner 1 and scanner 2 and separately to discover the multidimensional patterns of the spectral datasets. Results of PCA calculated on the averaged, smoothed (Savitzky-Golay filter) and pretreated spectra of pure and adulterated wheat gluten samples using the range between 950 and 1630 nm acquired with scanner 1 is shown in Fig. 2.1. Score plot of PC1 and PC2 presenting more than 60 % of the spectral variation presents good tendency of separation based on the total gluten content of the pure and adulterated wheat gluten samples (Fig. 2.2 a) mainly based on PC1. Separation of two main groups was observed in the PCA score plots in the case of data of both scanners (Fig. 2.2 b, for scanner 1). The grouping of samples was caused by the spectral differences of the wheat gluten samples originated from Europe and Asia.

Further analysis were performed coloring the PCA scores based on melamine or urea concentration and results showed separation based on the concentration of the adulterants in PC1 and PC2 plain similar to the result of separation of the different concentration wheat gluten. The wavelengths having highest importance of the separation of the samples containing different concentration of adulteration i.e. melamine and/or urea, can be discovered based on the loadings of the PCA mod-

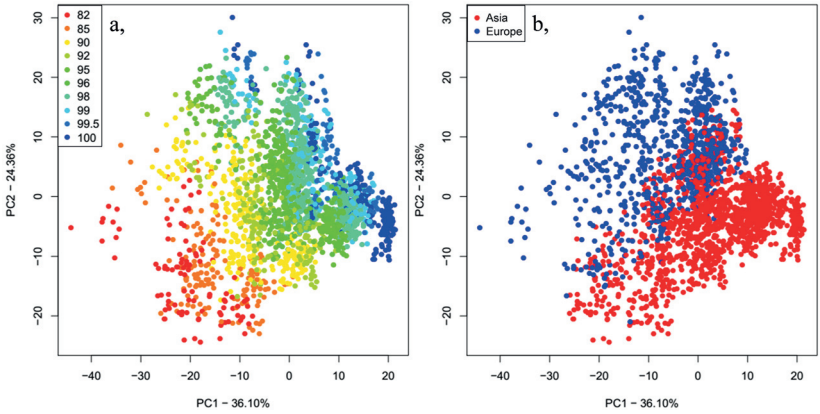

Figure 2.2: PCA score plots (PC1-PC2) of pure and adulterated wheat gluten samples calculated by the averaged, smoothed (Savitzky-Golay filter) and pretreated spectra of the 950–1630 nm range (n = 2314) acquired with scanner 1. a) Represents the score plot colored by wheat gluten concentration. b) Represents the score plot colored by origin of wheat gluten samples.

els (Fig. 2.3 for scanner 1). Loadings of PC1 and PC2 beside others highlights the importance of 1030, 1218, 1302, 1326, 1468, 1490 and 1532 nm which are in the ranges of the absorption peaks of the main components of the mixtures i.e. wheat gluten, melamine and urea.

The pattern encoded in the spectral dataset revealed by the exploratory data evaluation gives the rise to build regression models for simultaneous quantification of melamine and urea concentration in wheat gluten samples.

Results of the PLSR model built to predict melamine concentration based on data of scanner 1 is shown in Fig. 2.4 a,. High coefficient of determination (R^2) was found in model training (R^2tr = 0.9877) and as well as in cross-validation (R^2cv = 0.9858). The error of training (RMSEC) and cross-validation (RMSECV) were 0.3182 and 0.3429 %, respectively. The independent prediction performed with the data of scanner 2 (Fig. 2.4 b,) also proved the high accuracy and robustness of the model (R^2_{pr} = 0.9818 and RMSEP = 0.39 %). Similar results could be achieved with the model built on the data of scanner 2; parameters of the model, validation and prediction are R^2tr = 0.9815, RMSEC =

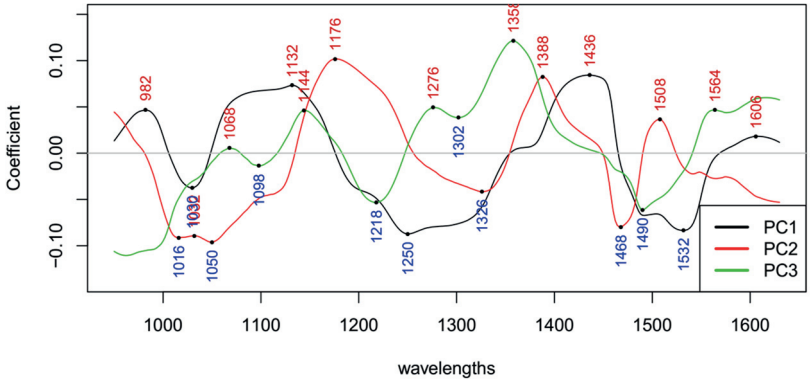

Figure 2.3: PCA loadings plot (PC1-PC3) of pure and adulterated wheat gluten samples calculated by the averaged, smoothed (Savitzky-Golay filter) and pretreated spectra of the 950–1630 nm range (n = 2314) acquired with scanner 1.

0.3927 % and R^2cv = 0.9798, RMSECV = 0.104 % and R^2_{pr} = 0.9775 and RMSEP = 0.43 %, respectively.

Models built to predict urea concentration were also found to be reliable. PLSR model built on the data of scanner 2 showed slightly better accuracy than that of scanner 1 (Fig. 2.5).

The coefficient of determination for the training (R^2tr) and for the cross-validation (R^2cv) were found 0.9163 and 8773, respectively (Fig. 2.5 a,), while for the independent prediction based on the data collected with scanner 1 (R^2_{pr}) was 0.9034 (Fig. 2.5 b,). The average prediction error of training (RMSEC = 0.8944 %) and cross-validation (RMSECV = 1.0597 %) as well as of independent prediction (RMSEP = 0.9607 %) confirmed that the determination of urea concentration in wheat gluten powder is also possible with 1 % average prediction error beside the changing concentration of melamine with the handheld food scanner.

Regression coefficient vectors of PLSR models provide information about the wavelengths of highest importance in the quantitative regression models (Fig. 2.6).

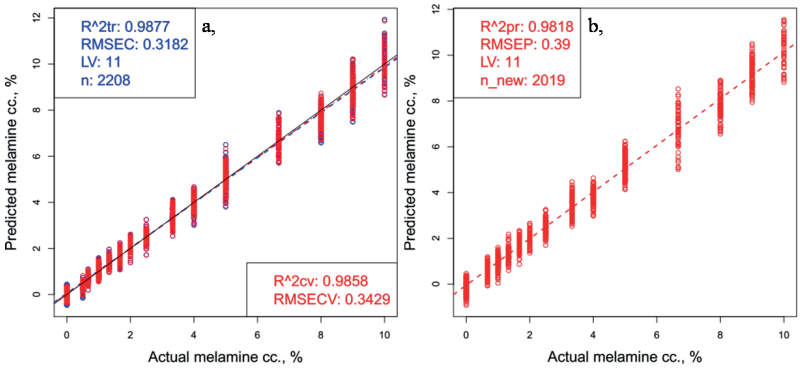

Figure 2.4: Calibration, cross- and independent validation of PLSR on melamine concentration in wheat gluten samples. a) Results of calibration model (blue color) and cross-validation (red color) built on data of scanner 1. b) Results of independent prediction based on data of scanner 2.

The coefficient vector of the regression model built for the determination of the melamine concentration in wheat gluten samples (Fig. 2.6 a,) proves the high importance of the wavelengths 1472, 1492 and 1522 nm which are the characteristic absorption peaks of melamine. The wavelengths found in the regression vector of the urea model (Fig. 2.6 b,) at 1042, 1224, 1304 nm and in the range between 1468 and 1538 nm also obviously present that the spectra of the adulterated wheat gluten samples acquired with the handheld food scanner hold the information of the absorption of urea.

4 Conclusions

Spectra of pure melamine, urea and wheat gluten samples showed that the handheld NIR scanner is applicable to accurately measure the characteristic absorption peaks of the tested chemicals. Results of principal component analysis presented good tendency of separation based on the total gluten content of the pure and adulterated gluten samples based on their NIR spectra. Separation of two main groups was ob-

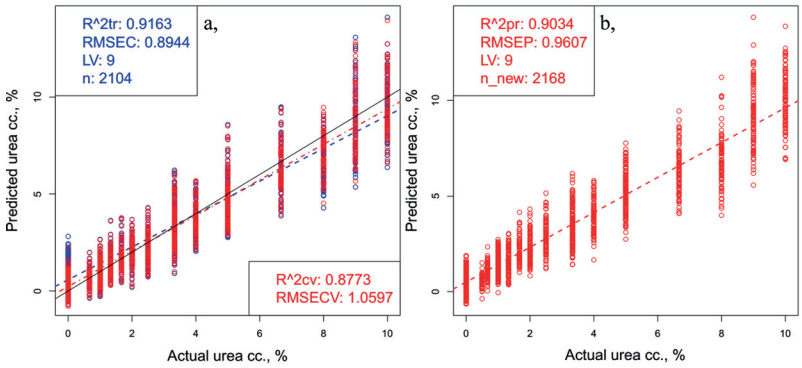

Figure 2.5: Calibration, cross- and independent validation of PLSR on urea concentration in wheat gluten samples. a) Results of calibration model (blue color) and cross-validation (red color) built on data of scanner 2. b) Results of independent prediction based on data of scanner 1.

served in the PCA score plots, which was caused by the spectral differences of the gluten samples originated from Europe and Asia. In spite of this natural separation it was possible to gain robust models to predict melamine and/or urea concentration accurately. Accurate models were built for simultaneous quantification of melamine and urea, in multiple mixtures of gluten. The achieved results prove that the Tellspec Enterprise Food Sensor as a rapid, cost effective and user friendly tool can be used for simultaneous quantification of the most common food adulterants in wheat gluten powders at or lower than 1 % adulteration level.

Acknowledgements

Authors would like to thank Meelunie B.V. for providing samples for this research; the team at Tellspec Inc and Tellspec LTD for data collection (Zsofia Pinter), data treatment (Behafarid Darvish), mobile app development (Jason Coulls), and cloud architecture (Mark Bloore); the HungarianNational Excellence Program of the Ministry of Human Capacities (ÚNKP-16-4, granted author: George Bazar) and the János

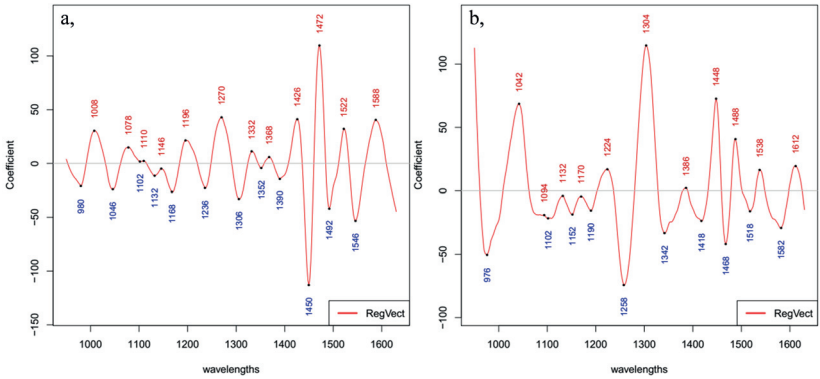

Figure 2.6: Regression coefficient vectors of PLSR models with the assigned wavelengths having the highest weight in the regression models. a) PLSR on melamine concentration in wheat gluten samples (Fig. 2.4). b) PLSR on urea concentration in wheat gluten samples (Fig. 2.5).

Bolyai Research Scholarship of the Hungarian Academy of Sciences (granted author: Zoltan Kovacs).

References

1. Domingo, E. et al., "Melamine detection in milk using vibrational spectroscopy and chemometrics analysis: A review. food research international, 60, pp.131–139."
2. Lin, M., "A review of traditional and novel detection techniques for melamine and its analogues in foods and animal feed. frontiers of chemical engineering in china, 3(4), pp.427–435."
3. Moore, J.C. et al., "Total protein methods and their potential utility to reduce the risk of food protein adulteration. comprehensive reviews in food science and food safety, 9(4), pp. 330–357."
4. Desmarchelier, A. et al., "Simultaneous quantitative determination of melamine and cyanuric acid in cow's milk and milk-based infant formula by liquid chromatography-electrospray ionization tandem mass spectrometry. journal of agricultural and food chemistry, 57(16), pp.7186–93."

5. Koh, G. et al., "Determination of melamine in milk powder using gas chromatography-high-resolution isotope dilution mass spectrometry. journal of separation science, 34(21), pp.3043–52."
6. Dallet, P. et al., "Determination of urea, allantoin and lysine pyroglutamate in cosmetic samples by hydrophilic interaction chromatography, journal of chromatography b, 742, pp. 447–452."
7. Mauer, L.J. et al., "Melamine detection in infant formula powder using near- and mid-infrared spectroscopy. journal of agricultural and food chemistry, 57(10), pp.3974–3980."
8. Balabin, R.M., Smirnov, S. V., "Melamine detection by mid- and near-infrared (mir/nir) spectroscopy: A quick and sensitive method for dairy products analysis including liquid milk, infant formula, and milk powder. talanta, 85(1), pp.562–568."
9. Lin, M. et al., "Detection of melamine in gluten, chicken feed, and processed foods using surface enhanced raman spectroscopy and hplc. journal of food science, 73(8), pp.t129–t134."
10. Liu, R. et al., "Discriminant analysis of milk adulteration based on near-infrared spectroscopy and pattern recognition. in r. j. nordstrom & g. l. coté, eds. international society for optics and photonics, p. 79060y."
11. Yang, R.-J., Liu, R., Xu, K.X., "Adulteration detection of urea in milk by mid-infrared spectroscopy."
12. Khan, K.M. et al., "Detection of urea adulteration in milk using near-infrared raman spectroscopy. food analytical methods, 8(1), pp. 93–102."
13. Qin, J., Chao, K., Kim, M.S., "Simultaneous detection of multiple adulterants in dry milk using macro-scale raman chemical imaging.food chemistry, 138(2), pp.998–1007."
14. Cowe, I.A. , McNicol, J.W., "The use of principal components in the analysis of near-infrared spectra. applied spectroscopy, 39(2), pp.257–266."
15. Naes, T. et al., "A user friendly guide to multivariate calibration and classification, chichester, uk: Nir publications."
16. Cantor, S.L., Gupta, A., Khan, M.A., "Analytical methods for the evaluation of melamine contamination. journal of pharmaceutical sciences, 103(2), pp.539–544."
17. González-Martín, I., Hernández-Hierro, J.M., "Detection and quantification of additives (urea, biuret and poultry litter) in alfalfas by nir spectroscopy with fibre-optic probe. talanta, 76(5), pp.1130–1135."

18. Bruun, S.W., Søndergaard, I., Jacobsen, S., "Analysis of protein structures and interactions in complex food by near-infrared spectroscopy. journal of agricultural and food chemistry, 55(18), pp.7234–7243."

Detection of beef aging combined with the differentiation of tenderloin and sirloin using a handheld NIR scanner

George Bazar[1,2], Zoltan Kovacs[1,3], Isabel Hoffmann[1]

[1] Tellspec Inc.
Toronto, Ontario, Canada
[2] Kaposvar University
Faculty of Agricultural and Environmental Sciences
Kaposvar, Hungary
[3] Szent Istvan University
Faculty of Food Science
Budapest, Hungary

Abstract There is an expressed need for non-destructive user-friendly tools that can help customers and various stakeholders of the food market to identify and qualify samples rapidly and accurately. The identification of high quality meat cuts and the determination of aging are important challenges where handheld near infrared spectroscopy can provide perfect solutions. The objective of this study was to develop multivariate models for differentiation of beef cuts and prediction of the aging time based on the NIR spectra acquired with a handheld Tellspec Enterprise Food Sensor. Sirloin and tenderloin samples were stored at 4°C in plastic bags for 10-day period during two experiments, and spectra were recorded daily. The investigated sirloin and tenderloin samples were separated in principal component analysis, and it was possible to use the principal components in a supervised classification (linear discriminant analysis) to build model on meat authentication. 85.37 % of the sirloin and tenderloin samples were classified correctly in independent validation tests. Multivariate calibration on aging was developed for the separate meat types. After omitting the first and last days of the experiments, accurate calibration models were built on the aging of beef samples. Accordingly, 1.1 or 1.5 days of precision was achieved during independent predictions for aging time of sir-

loin or tenderloin, respectively. Our results proved that the Tellspec Enterprise Food Sensor provides the possibility for rapid and non-destructive determination of meat type and stage of aging.

Keywords: Portable, near infrared spectroscopy, meat, classification, calibration, storage.

1 Introduction

The quality of beef highly depends on the cut [1] and aging time [2]. Consumers are willing to buy valid product of known origin if it has special palatability or nutritional merit, even if it has a higher price [3]. Among other motives, the high commercial value of meats which are more valued by consumers leads to an expressed need for fast, accurate and objective methods to identify the different types of meats by species and cuts, and to determine the post mortem aging time. Near infrared (NIR) spectroscopy as a cost effective analytical method is widely used in food industry for measurement of quality attributes. The NIR technique is a rapid and non-destructive method requiring little or no sample preparation, still, it provides high accuracy in many applications. Contrary to wet chemistry, no reagents are required and no waste is produced.The first application of NIR technique to detect properties of meat was reported five decades ago [4], and thirty years later on-line applications were developed for food industry [5]. NIR spectroscopy is among the most progressive methods frequently used for qualitative and quantitative analyses of various meats [6]. Nowadays, the miniaturized NIR spectrometers are used in many fields of research, however, there is still a vast need for simple low cost NIR instruments usable by non-technical personnel in everyday situations. The goal of the present study was to develop multivariate models for differentiation of different beef cuts and prediction of the aging time based on the NIR spectra acquired with a handheld scanner.

2 Materials and methods

Twelve slices of beef tenderloin (n = 6) and sirloin (n = 6) were stored at 4°C in sealed plastic bags over a 10-day period (Fig. 3.1). Meats

Figure 3.1: (a): Beef tenderloin; (b): sirloin samples of the experiment 1, prepared for storage.

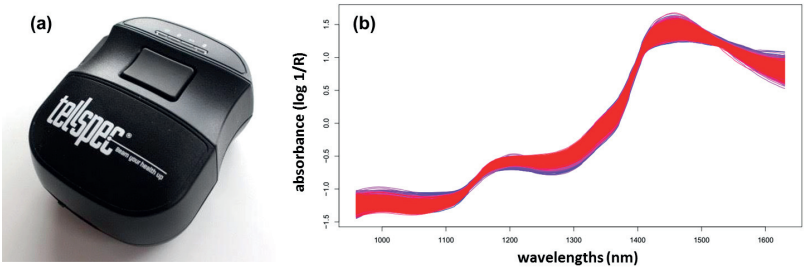

Figure 3.2: (a): The Tellspec Enterprise Food Sensor handheld NIR spectrometer; (b) the acquired spectra (n = 600) of tenderloin and sirloin samples of experiment 1.

were purchased from a Hungarian slaughter house, slices were cut and packed right after dissection, following a 24 hours post slaughter chilling. The experiment was performed twice with one month difference (experiment 1 and experiment 2) in order to validate the quantitative and qualitative NIR models using independent data (total n = 24).

The NIR spectrum of each slice was acquired through the plastic bag, using a Tellspec Enterprise Food Sensor (Tellspec Inc., Toronto, Ontario, Canada) (Fig. 3.2a). Spectra of each slice were recorded daily with 2 nm spectral step in the 950–1630 nm spectral interval, using the Tellspec application for mobile devices. Figure 3.2b shows the raw

spectra of experiment 1 (n = 600). Various sample pre-processing methods and multivariate data analysis techniques were used to process the spectral data [7]. Principal component analysis (PCA) was used to detect spectral outliers and describe the multidimensional pattern of the dataset [8]. Supervised classification models were built with linear discriminant analysis (LDA) to perform pre-defined grouping of tenderloin and sirloin samples based on the spectral properties [7]. Partial least squares regression (PLSR) was used to develop NIR calibration models on the aging [9]. Cross-validation was used for optimization of the models, when data of single days were left out of the calibration and were used for validation, iteratively. Independent validation was applied between the two experiments when models of one experiment were tested with the data of the other experiment. Data processing and evaluation was done with the R Project (www.r-project.org).

3 Results and discussion

Considerable spectral difference was observed between the NIR spectra of tenderloin and sirloin, and according to aging of the meat samples. Daily NIR data (smoothed and normalized) were evaluated with PCA to see the spectral differences of the two meat cuts. PCA score plot of Fig. 3.3a shows the separation of tenderloin and sirloin samples on one day. The separation is along PC1 that describes 92.5 % of the total spectral variation. PC1 loading was dominated by fat (C-H) absorption region around 1210 nm, showing the differences in intramuscular fat content of the two meat types. NIR data of the whole experiments were evaluated with PCA to check the spectral variation according to aging. Figure 3.3b shows the PCA score plot of the sirloin samples of experiment 1. Colors indicate the date of aging (from red to blue), showing that PC2 covering 17.8 % of total spectral variation highlights the spectral regions changing considerably during aging. PC2 loadings highlighted water absorption bands in 1380 and 1450 nm regions showing the changes of water structure.

The separation of the two cuts in the PCA score plot considering the whole dataset of experiment 1 is shown in Fig. 3.4a. The PCA scores were used as input variables to build the LDA models providing orthogonal variables for identification of sirloin or tenderloin spec-

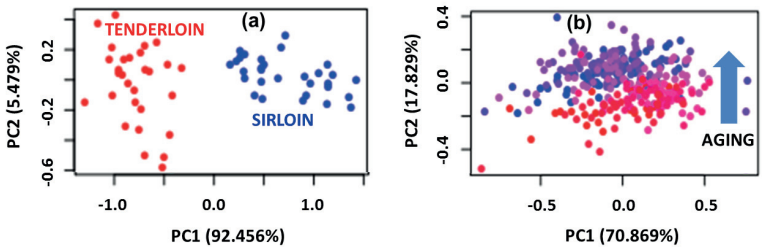

Figure 3.3: (a): PCA score plot showing data of one day with a clear separation of the tenderloin and sirloin samples along PC1; (b): PCA score plot of the sirloin samples of experiment 1 showing the trend of aging along PC2.

tra. The models were calculated on one of the two experiments and were tested with the data of the other experiment (Fig. 3.4b). The ratios of the correctly classified samples during the LDA model building processes were 93.55 % and 93.23 % for experiment 1 and experiment 2, respectively. The hit ratios of the two validation tests of the LDA models were 83.76 % and 86.97 %, respectively.

The PLSR calibration models on aging were prepared with sirloin and tenderloin spectra separately. Models were trained on one of the two experiments applying cross-validation based optimization where one day's data were left out iteratively, and spectra of the other experiment were used for independent predictions to validate the model. More accurate predictions were achieved for sirloin then for tenderloin. The root mean square error of prediction (RMSEP) was less than 2 days for sirloin, and 2.5 days for tenderloin. As Fig. 3.5 shows, non-linear change of the meat samples was observed during aging. Accordingly, PLSR models were built on the middle of the investigated period (2-9 days), and average accuracy (RMSEP) of the independent predictions improved to 1.13 days for sirloin and 1.48 days for tenderloin (Fig. 3.6).

4 Conclusions

The aging and the type of the meats have significant effect on the NIR spectra recorded with the handheld Tellspec Enterprise Food Sensor.

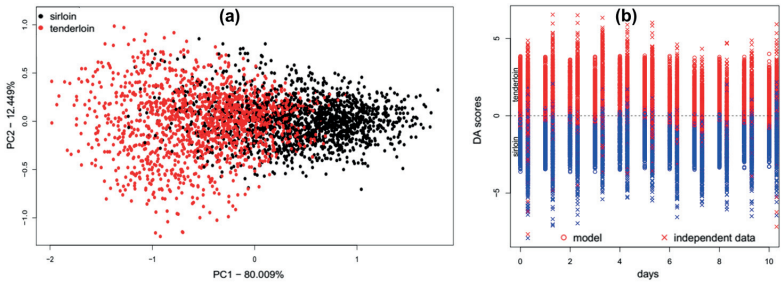

Figure 3.4: (a): PCA score plot of the beef spectra recorded in experiment 1, showing the difference of sirloin and tenderloin along PC1 that describes 80 % of the total spectral variation; (b): results of the classification of sirloin and tenderloin samples when the LDA model was built on the spectra of experiment 2, and it was validated with 86.97 % hit ratio using the independent samples of experiment 1.

The investigated sirloin and tenderloin samples were separated based on the spectral information related to C-H bonds, i.e. intramuscular fat. It was possible to use the principal components in a supervised classification to build model on meat authentication. 85.37 % of the sirloin and tenderloin samples were classified correctly in independent validation tests. Meat type has bigger effect on the NIR spectra when compared to the effect of meat aging, thus, it is reasonable to calibrate on aging within the separate meat types (sirloin or tenderloin). Due to the non-linear changes of meat during the aging process, it was possible to achieve calibration models on meat aging with an accuracy of 2 or 2.5 days for sirloin or tenderloin, respectively. To decrease the non-linearity, calibration models were built after omitting the initial and final days of the experiments. This resulted 1.1 or 1.5 days of precision during independent prediction for aging time of sirloin or tenderloin, respectively. Our results proved that the Tellspec Enterprise Food Sensor provides the possibility for rapid and non-destructive determination of meat type and days of storage, i.e. stage of aging.

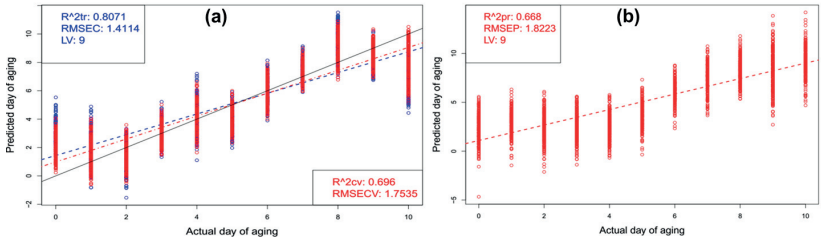

Figure 3.5: (a): Calibration (blue) and cross-validation (red) results of the PLSR model prepared on aging days of sirloin samples of experiment 2; (b): prediction results of the above mentioned PLSR model when sirloin samples of experiment 1 were used as independent sample set. (R^2tr/cv/pr: coefficient of determination in calibration training/cross-validation/independent prediction, RMSEC/RMSECV/RMSEP: root mean square error of calibration/cross-validation/prediction, LV: number of latent variables).

Acknowledgements

Authors would like to thank the team at Tellspec Inc and Tellspec LTD for data collection (Zsofia Pinter), data treatment (Behafarid Darvish), mobile app development (Jason Coulls), and cloud architecture (Mark Bloore); the HungarianNational Excellence Program of the Ministry of Human Capacities (ÚNKP-16-4, granted author: George Bazar) and the János Bolyai Research Scholarship of the Hungarian Academy of Sciences (granted author: Zoltan Kovacs).

References

1. Carmack, C.F. et al., "Sensory evaluation of beef-flavor-intensity, tenderness, and juiciness among major muscles. meat science, 39(1), pp.143–147."
2. Idolo Imafidon, G. and Spanier, A.M., "Unraveling the secret of meat flavor. trends in food science & technology, 5(10), pp.315–321."
3. Bázár, G. et al., "Identification of traditionally reared mangalica pig's meat by near infrared spectroscopy using generalised partial least squares in open source r project—a feasibility model study. journal of near infrared spectroscopy, 17(1), p.119."

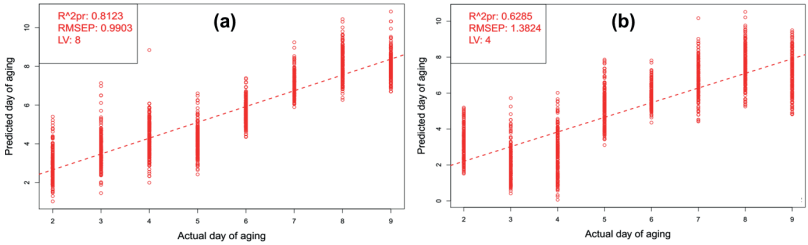

Figure 3.6: Independent prediction of aging days of the (a) sirloin and (b) tenderloin samples of experiment 2 using PLSR models trained on the NIR data of the sirloin or tenderloin samples of experiment1, repsectively. (R^2pr: coefficient of determination in prediction, RMSEP: root mean square error of prediction, LV: number of latent variables).

4. Ben-Gera, I. and Norris, K.H., "Direct spectrophotometric determination of fat and moisture in meat products. journal of food science, 33(1), pp.64–67."
5. Isaksson, T. et al., "On-line, proximate analysis of ground beef directly at a meat grinder outlet. meat science, 43(3), pp.245–253."
6. Prieto, N. et al., "Application of near infrared reflectance spectroscopy to predict meat and meat products quality: A review. meat science, 83(2), pp.175–186."
7. Naes, T. et al., "A user friendly guide to multivariate calibration and classification, chichester, uk: Nir publications."
8. Cowe, I.A. and McNicol, J.W., "The use of principal components in the analysis of near-infrared spectra. applied spectroscopy, 39(2), pp.257–266."
9. Geladi, P. and Kowalski, B.R., "Partial least-squares regression: a tutorial. analytica chimica acta, 185, pp.1–17."

Non-invasive assessment of the bioburden of minced pork using a hand-held fluorescence device

Christina Grimmler[1], Tamara Kuhfuß[1], Matthias Heiden[2], Heinar Schmidt[1]

[1] University of Bayreuth, Chair of Bioanalytical Sciences and Food Analysis, E.-C.-Baumann-Str. 20, 95326, Kulmbach
[2] Freshdetect GmbH, Kirchplatz 1, 82049 Pullach im Isartal

Abstract To speed-up monitoring of the hygienic status of meat, fast and non-invasive measuring techniques are required. The feasibility of a hand-held fluorescence device (freshdetect) was investigated to quantify the bioburden of minced pork meat. In total, 144 minced pork samples from 18 batches were stored at 2°C for up to 8 days. Fluorescence spectra, L*a*b* colour and total viable mesophilic plate counts (TVC) were measured in parallel during this period. Correlation of the fluorescence spectra with log(TVC/g) using partial least squares regression yielded cross-validated predictions with $R^2cv = 0.72$ and a prediction error of RMSECV = 0.97 log(TVC/g). Cross-validated limits of detection and quantification were determined as 1.03 and 3.38 log(TVC/g), respectively. This would allow for a quantification well below the alarm threshold of 5.7-6.7 log(TVC/g). The spectra correlated also well with storage time ($R^2cv = 0.81$), but less strong with L*a*b* colour.

Keywords: Meat inpection, fluorescence spectra, minced pork.

1 Introduction

Minced meat is a very perishable commodity requiring special attention with respect to hygiene requirements and control of bioburden. Conventional analysis of bioburden is based on destructive sampling and methods such as colony counts or flow cytometry which are labour

intensive, time consuming and expensive. With these restrictions, they are only suitable for a random monitoring, but not for on-line control. In this regard, spectroscopic methods are a promising alternative as they are fast, non-destructive and allow for on-line applications. A number of spectroscopic methods such as fluorescence, FT-IR, NIR or Raman have been shown to be suitable for an assessment of the microbial status of meat.

Fourier transform infrared (FT-IR) spectroscopy using attenuated-total reflectance (ATR) was proven to rate the microbial cell density on minced beef [1], minced pork [2] or beef fillets [3–5]. Quantification was shown using partial least squares regressions (PLSR) and artificial neural network (ANN) models. While FT-IR is fast and non-invasive, a number of drawbacks are limiting the applicability of the mid-infrared technology in practice. For example, the ATR crystal is brittle, toxic and water is strongly interfering. Complementary information to the mid-infrared is obtained with Raman spectroscopy, but avoiding interference from water and the material restrictions of IR. Microbial spoilage of pork was qualitatively detected with a handheld Raman scanner [6,7] and it was shown that PLSR models were able to predict microbial spoilage as accurately from Raman spectra as from the FT-IR spectra [8].

Similarly, NIR hyperspectral imaging was shown to allow for a prediction of bacterial surface counts [9–11]. With pork (n = 51) as example, NIR-hyerspectral imaging proved feasibility of predicting bioburden with $R^2cv = 0.82$ and a prediction error of 0.83 log(TVC/cm²) [10].

The prediction of bacterial surface counts by fluorescence spectroscopy is based on different fluorophors depending on the excitation wavelength [12–16]. With 280 and 380 nm, fluorescence of NAD(P)H, flavins, Lipids and porphyrins are excited and used for the correlations [14]. The authors obtained prediction errors below one log-unit, but the number of samples was very low (n = 28). Using synchronous fluorescence spectroscopy with excitation between 250 nm and 500 nm, aromatic amino acids were excited. Given a low number of samples (n = 21) rather optimistic prediction errors of 0.2 log TVC/cm² were reported [15]. Oto et al. have correlated tryptophan and NADPH fluorescences of pork (n = 23) with ATP content and bioburden based on excitation-emission matrices (EEM) resulting in cross-validated coefficients of determination of R^2cv of 0.84-0.88 [13].

Similarly, Yoshimura et al. employed EEM data exploiting signals of a variety of fluorophores to quantify bioburden of beef samples (n = 60) [12]. This work showed that five endogeneous fluorophors (tryptophan, NAD(P)H, retinol, flavins und porphyrins) were used in the predictive models. The authors achieved in a calibration range of 1.8 to 7.8 log(TVC/cm²) errors of prediction of 0.8 log(TVC/cm²). However, acquisition of excitation-emission matrices is time-consuming and thus difficult to transfer into a rapid application. An approach which is concentrating specifically on the fluorescence of porphyrins [16] has the advantage that the detection system can be less complicated and speed up the measurement. Schneider et al. have shown that protoporphyrin XI as well as the zinc and magnesium complexes thereof are suitable for a detection of meat spoilage [16,17].

To transfer these techniques from the laboratory to real-world processes, portable devices were developed. In a generic approach, the development of mobile instrumentation for fluorescence, reflectance and Raman spectroscopy was pursued [18]. Two prototype instruments were developed from this project: a handheld Raman probe head [6,19] and a prototype mobile fluorescence device [17]. The latter used a blue ray laser diode with emission at 405 nm for excitation and an 18 around 1 fibre-optic probe head for delivery and collection of the signals. The fluorescence signals were bandpass-filtered to 570–650 nm to detect specifically the fluorescence of porphyrins, namely protoporphyrin IX and Zn-protoporphyrin IX [17]. The freshdetect device is a further development of this fluorescence device. It is robust and handheld, uses 405 nm excitation, fibre-optic signal collection, and the fluorescence signals are recorded by a miniaturised spectrometer in the range 460 to 900 nm. Ait-Kaddour et al. developed a portable spectrofluorimeter based on three UV excitation wavelengths (280, 320 and 380 nm) delivered by a fibre-optic probe which was connected to a miniature spectrograph [14]. The authors investigated the quantification of spoilage of minced beef vacuum-packaged and stored at 5°C and 15°C over a period of eleven days on the basis of one mixed sample (n = 1) and 28 measuring days. Based on this small sample, quantification was shown feasible with cross-validated coefficients of determination ranging from 0.5 to 0.99.

The transfer to robust and portable devices, however, is still an ongoing challenge since they require in general a calibration for their specific

applications. Previous work has mainly focused on demonstrating the feasibility and evaluating performance. In general, however, data sets were too small to allow for robust predictions. Therefore, further work is required to enlarge the field of applications and to build up larger data sets for robust calibration of the devices.

The aim of this work was to show the feasibility of quantifying the bioburden of minced pork with a new prototype of the hand-held freshdetect device. Minced pork was chosen for the experiment because of its relevance as a very perishable commodity. Particularly with regard to the coarse mixture of lean meat and fat, the textural inhomogeneity of minced meat is a challenge for the detection method. As this inhomogeneity can also be monitored by the colour, the interdependence between fluorescence spectra, colour and bioburden was also investigated.

2 Materials and methods

To standardise origin and age of the meat, cuts from 18 female pigs, all crossbred of German landrace and Piétrain were obtained directly from an abattoir at day 1 after slaughtering. Cuts from the leg were chosen which are commercially used for minced meat. In total 18 batches (1 per animal) of minced pork were prepared from these cuts on day 1 after slaughtering using a Carneoline FW N/22/82 (Bizerba, Germany) mincing machine with 3 mm sieves. From these batches, 144 samples (8 per animal) were prepared in 6 measuring series and they were stored in petri dishes at 2°C from 1 to 8 days allowing for bacterial growth.

Fluorescence spectra, colour and total viable mesophilic plate counts (TVC) were daily measured during this period. Eight fluorescence spectra and 5 white light spectra were recorded per sample with the freshdetect device (Freshdetect GmbH, Germany) with an excitation wavelength of 405 nm or a white light LED and spectra were recorded from 460 nm to 900 nm. As a reference, colour readings with three repetitions each were taken at 5 different positions with a Minolta Chromameter CR-400 using the following settings: D65, 2° observation angle and normalization to a white standard (Y = 88.3, x = 0.3191, y = 0.3367). On each measuring day, microbial reference analyses were performed in duplicate with 5 cm^2 sub-samples which were taken from

Table 4.1: Summary results of the bioburden log(TVC/g) of 144 samples.

Parameter	log(TVC/g)
Minimum	2.67
Mean	5.13
Median	4.57
Maximum	10.43
Standard Deviation	1.80

the minced meat in the petri dishes. The subsamples were weighed, homogenized in peptone water and analysed with the plate count method according to §35 LMBG, DIN 10161 part 1.

Dark spectra were subtracted before fluorescence spectra were averaged per sample and normalized in intensity using the fluorescence at 612 nm of a lumilass-R7 filter as standard. The fluorescence spectra were pre-processed by Savitzky-Golay smoothing (order 0, filter width 15), standard normal variate (SNV) and mean-centering and then they were correlated with the logarithm of the bioburden using partial least squares regression (PLSR) using MATLAB 7.9.0 R2009b software (The Mathworks Inc., Natick, MA, USA) and PLS Toolbox 7.5 (Eigenvector Research Inc., Wenatchee, WA, USA). For cross-validation of the models, the random subset method with 10 data splits and 20 iterations was employed.

3 Results and discussion

The kinetics of bacterial growth during storage and the distribution of the bioburden per day are shown in Fig. 4.1. Data are not normal distributed (see Tab. 4.1). Therefore, the median is used to describe the trends. The initial bioburden of the samples started at 4.34 log(TVC/g) at day 1 and bacteria grew up to 7.40 log(TVC/g) on day 8 (Fig. 4.1). The bacterial growth was lagging during the first 3 days with 0.05 log units per day (dotted line). Exponential growth started at day 4 at a rate of 0.96 log units per day (dashed line, Fig. 4.1). On average, the critical threshold of 5.7 log(TVC/g) was reached at day 6.

The fluorescence spectra correlated well with bioburden, $R^2cal = 0.80$ (see Tab. 4.2 and Fig. 4.2). The cross-validated PLSR model ($R^2cv = 0.72$) was able to predict the logarithm of total viable counts with an

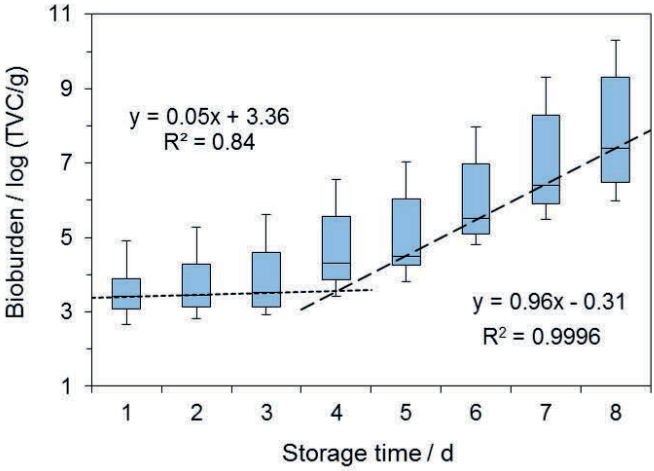

Figure 4.1: Bioburden of minced pork versus storage time at 2 °C. Lag and exponential phases are indicated by dotted and dashed lines.

RMSECV = 0.97 log (TVC/g) which is close to the error of the reference method. The congruence between calibration (filled circles) and cross-validation (open circles) was in general good. However, larger discrepancies were observed at bioburdens larger than 8 log(TVC/g). This could be due to an underrepresentation of such high bioburdens in the data set. On the other hand, bioburdens at this level are readily perceived organoleptically. In any case, the lower range, especially around and below the alarm thresholds, is most relevant for the application.

To estimate the suitability of this PLSR calibration, the limits of detection (LOD) and of quantification (LOQ) were calculated according to DIN 32465 at a 95% confidence level as LOD = 1.03 log(TVC/g) and LOQ = 3.38 log(TVC/g). This would allow for a quantification well below the alarm threshold.

The fluorescence spectra even correlated better with the storage time ($R^2cv = 0.81$), while the correlation with L*a*b* colour was less strong, see Tab. 4.2. A cross-correlation of the five parameters showed medium to strong interdependences between the parameters, see Tab. 4.3. Storage time showed strong positive correlation with bioburden and neg-

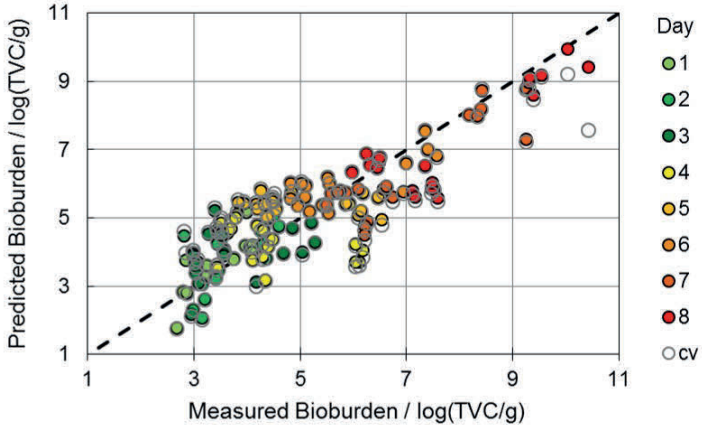

Figure 4.2: PLSR prediction of the bioburden using fluorescence spectra of the freshdetect device versus measured bioburden, filled circles: calibration, open circles: cross-validation, colours are encoding the storage time.

Table 4.2: Results of PLSR correlations of fluorescence spectra with bioburden (log(TVC/g)) and storage time (d) and of white light spectra with L*a*b* colour.

Parameter	Bioburden	Storage Time	L*	a*	b*
R^2_{cal}	0.80	0.85	0.59	0.58	0.23
R^2_{cv}	0.72	0.81	0.58	0.57	0.22
RMSEC	0.80	0.9	3.78	2.22	1.47
RMSECV	0.97	1.0	3.84	2.25	1.49
Latent Variables	8	6	5	5	4
Samples	144	144	144	144	144

ative correlation with the a* value. Bioburden was also moderately negative correlated with the a* value. The b* value was moderately correlated with storage time and a*, but faintly with bioburden. It is very likely that much of this interdependence is due to the measuring protocol which links ageing of the samples to the development of bioburden and changes of the colour parameters. On the other hand, the L* showed almost no correlation with bioburden or storage time. This could be interpreted as if there was no correlation or as the variance in the L* incurred by the coarse mixture of meat and fat was so high that a possible correlation with storage time or bioburden was lost.

Table 4.3: Correlation coefficients of the cross-correlations of bioburden, storage time and L*a*b* colour.

	Bioburden	Storage Time	L*	a*	b*
Bioburden	1				
Storage Time	0.77	1			
L*	0.07	-0.06	1		
a*	-0.46	-0.69	-0.51	1	
b*	-0.23	-0.52	0.1	0.57	1

The measuring and sampling protocol has to be changed to overcome some of these interdependences.

4 Summary

In this feasibility study which was based on 144 samples generated from 18 independent batches, the freshdetect device proved suitable for a non-invasive evaluation of the microbial status of minced pork. The LOD was determined as 1.03 log(TVC/g) and the LOQ as 3.38 log(TVC/g), respectively. Thus, the quantification of the bioburden was shown to be feasible with an error of 1.0 log(TVC/g) at a 95% probability level well below the alarm threshold of 5.7 log(TVC/g).

The results of this study are preliminary as only one crossbred (the most common one) was used as source of meat. The number of animals and independent samples, however, is larger than in most of the previously published studies. Furthermore, the measuring protocol has to be altered to reduce the interdependence of storage time with bacterial growth and changes in the colour. Future work will have to confirm the validity of the PLSR correlation with independent samples and to improve the robustness of the model by complementing the data set with samples covering more biological variance (different animals and origins).

Acknowledgement

This work was supported by Bundesministerium für Ernährung und Landwirtschaft under the project number 2816IP003 (DIP Agrar).

References

1. M. S. Ammor, A. Argyri, and G.-J. E. Nychas, "Rapid monitoring of the spoilage of minced beef stored under conventionally and active packaging conditions using Fourier transform infrared spectroscopy in tandem with chemometrics," *Meat Science*, vol. 81, no. 3, pp. 507–514, 2009.
2. O. Papadopoulou, E. Z. Panagou, C. C. Tassou, and G. J. E. Nychas, "Contribution of Fourier transform infrared (FTIR) spectroscopy data on the quantitative determination of minced pork meat spoilage," *Food Research International*, vol. 44, no. 10, pp. 3264–3271, 2011.
3. D. I. Ellis, D. Broadhurst, and R. Goodacre, "Rapid and quantitative detection of the microbial spoilage of beef by Fourier transform infrared spectroscopy and machine learning," *Analytica Chimica Acta*, vol. 514, no. 2, pp. 193–201, 2004.
4. E. Z. Panagou, F. R. Mohareb, A. A. Argyri, C. M. Bessant, and G.-J. E. Nychas, "A comparison of artificial neural networks and partial least squares modelling for the rapid detection of the microbial spoilage of beef fillets based on Fourier transform infrared spectral fingerprints," *Food Microbiology*, vol. 28, no. 4, pp. 782–790, 2011.
5. A. A. Argyri, E. Z. Panagou, P. A. Tarantilis, M. Polysiou, and G. J. E. Nychas, "Rapid qualitative and quantitative detection of beef fillets spoilage based on Fourier transform infrared spectroscopy data and artificial neural networks," *Sensors and Actuators B: Chemical*, vol. 145, no. 1, pp. 146–154, 2010.
6. H. Schmidt, K. Sowoidnich, and H.-D. Kronfeldt, "A prototype hand-held Raman sensor for the in situ characterization of meat quality," *Applied Spectroscopy*, vol. 64, no. 8, pp. 888–894, 2010.
7. K. Sowoidnich, H. Schmidt, H.-D. Kronfeldt, and F. Schwägele, "A portable 671nm Raman sensor system for rapid meat spoilage identification," *Vibrational Spectroscopy*, vol. 62, no. 0, pp. 70–76, 2012.
8. A. A. Argyri, R. M. Jarvis, D. Wedge, Y. Xu, E. Z. Panagou, R. Goodacre, and G.-J. E. Nychas, "A comparison of Raman and FT-IR spectroscopy for the prediction of meat spoilage," *Food Control*, vol. 29, no. 2, pp. 461–470, 2013.
9. L. Huang, J. Zhao, Q. Chen, and Y. Zhang, "Rapid detection of total viable count (TVC) in pork meat by hyperspectral imaging," *Food Research International*, vol. 54, pp. 821–828, 2013.
10. D. F. Barbin, G. ElMasry, D.-W. Sun, P. Allen, and N. Morsy, "Non-destructive assessment of microbial contamination in porcine meat using

NIR hyperspectral imaging," *Innovative Food Science and Emerging Technologies*, vol. 17, pp. 180–191, 2013.

11. M. Monroy, S. Prasher, M. O. Ngadi, N. Wang, and Y. Karimi, "Pork meat quality classification using visible/near-infrared spectroscopic data," *Biosystems Engineering*, vol. 107, no. 3, pp. 271–276, 2010.
12. M. Yoshimura, J. Sugiyama, M. Tsuta, K. Fujita, M. Shibata, M. Kokawa, S. Oshita, and N. Oto, "Prediction of aerobic plate count on beef surface using fluorescence fingerprint," *Food and Bioprocess Technology*, vol. 7, no. 5, pp. 1496–1504, 2014.
13. N. Oto, S. Oshita, Y. Makino, Y. Kawagoe, J. Sugiyama, and M. Yoshimura, "Non-destructive evaluation of ATP content and plate count on pork meat surface by fluorescence spectroscopy," *Meat Science*, vol. 93, pp. 579–585, 2013.
14. A. Ait-Kaddour, T. Boubellouta, and I. Chevallier, "Development of a portable spectrofluorimeter for measuring the microbial spoilage of minced beef," *Meat Science*, vol. 88, no. 4, pp. 675–681, 2011.
15. A. Sahar, T. Boubellouta, and E. Dufour, "Synchronous front-face fluorescence spectroscopy as a promising tool for the rapid determination of spoilage bacteria on chicken breast fillet," *Food Research International*, vol. 44, no. 1, pp. 471–480, 2011.
16. J. Schneider, J. Wulf, B. Surowsky, H. Schmidt, F. Schwägele, and O. Schlüter, "Fluorimetric detection of protoporphyrins as an indicator for quality monitoring of fresh intact pork meat," *Meat Science*, vol. 80, no. 4, pp. 1320–1325, 2008.
17. J. Durek, A. Fröhling, J. Bolling, R. Thomasius, P. Durek, and O. Schlüter, "Non-destructive mobile monitoring of microbial contaminations on meat surfaces using porphyrin fluorescence intensities," *Meat Science*, vol. 115, pp. 1–8, 2016.
18. G. Jordan, R. Thomasius, H. Schröder, J. S. Wulf, O. Schlüter, B. Sumpf, M. Maiwald, H. Schmidt, H. D. Kronfeldt, R. Scheuer, F. Schwägele, and K.-D. Lang, "Non-invasive mobile monitoring of meat quality," *Journal für Verbraucherschutz und Lebensmittelsicherheit*, vol. 4, no. 1, pp. 7–14, 2009.
19. H. Schmidt, K. Sowoidnich, M. Maiwald, B. Sumpf, and H.-D. Kronfeldt, "Hand-held Raman sensor head for in-situ characterization of meat quality applying a microsystem 671 nm diode laser," in *Proc. SPIE*, vol. 7312, 2009, pp. 73 120H–73 120H–8.

Optical identification of valuable materials on printed circuit board assemblies based on sensor fusion

Johannes Ruecker[1], Patrick Peper[1], Ulrich Bochtler[1], Peter J. Klar[2]

[1] University of Applied Sciences,
Würzburger Str. 45, 63743 Aschaffenburg, Germany
[2] Justus Liebig University,
Heinrich-Buff-Ring 16, 35392 Gießen, Germany

Abstract Increasing waste of electrical and electronic equipment (WEEE) is a major challenge of today's society. It affects society in several ways and needs to be solved to prevent loss of important materials and to reduce environmental contamination. Tackling this challenge requires affordable and reliable technological solutions, which enable recycling in a cheap and easy manner.

One step to be taken is the recycling of printed circuit board assemblies (PCBAs), which are common in many of the high level devices such as computers or mobile phones. PCBAs include a huge amount of different components and thus belong to the most heterogeneous waste a recycler has to handle. The approach described in this paper is directed towards a reduction of the diversity by identification of specific components on the PCBA, which contain specific materials of interest. These components are then available for automated, selective disassembly.

In this contribution classification results of a special descriptor developed for printed circuit boards are shown for three different classification algorithms. The descriptor is based on rather discriminative simple geometric and color features. The necessary data is obtained by a pilot setup, which is also described briefly, and processed with Waikato Environment for Knowledge Analysis (WEKA), a tool for processing big data.

Keywords: Machine learning, big data, descriptor, classification.

1 Introduction

During the last 20 years the amount of technology used daily has experienced a huge increase. This is not only manifested by the success of modern IT companies, but also by the massive amounts of personal electronic devices such as smartphones or computers used widely throughout the population. In particular, the timespan for new technologies to be in widespread use is decreasing, which can be seen by the rising number for tablet users which increased by a factor of 21.4 within the last seven years [1]. The downside of this development is the increase in waste from discarded technological products. Due to the wide distribution of such systems and their short life cycles this becomes an increasingly more severe problem. For instance in more than 86 % of the German households there is currently at least one personal computer [2]. The total amount of WEEE per person amounted to 21.6 kg in Germany in 2014 [3].

Parts of this waste contain high amounts of precious metals and rare earth elements, notably the electronic components like those on PCBAs. The current recycling rates for these elements from this type of electronic waste are rather low, which can be seen in [4]. The recycling rate of tantalum, for example, is close to zero, although tantalum is used in capacitors of a certain shape and type mounted typically to special PCBAs [5]. By specifically targeting such components in the extraction process, it will be possible to recover a fraction of the PCBA waste with a high yield of these elements, which then can be chemically reprocessed.

For this purpose, we developed a pilot plant for detecting specific types of components on PCBAs. It consists of a sensor system placed over a conveyor belt and is described in the following chapter. The output of the sensory unit is processed with different algorithms to automatically detect the type and position of certain components on the PCBA. The automatic detection process can be based on different approaches of machine learning. This contribution examines three typical ones with respect to their detection rate.

2 Measurement setup

The setup used for this study consists of an industrial camera and an entry level line scanner. Both units are synchronized and placed consecutively over a conveyor belt. The resolution of the camera is 6.5 pixels per mm. The line scanner reaches a resolution of 0.2 mm in z direction with a lateral resolution of 3 measurements per mm. The setup can be seen in figure 5.1 and is also described in detail in [6]. The calculation of the height of components on the PCBA is based on trigonometry and shown in [7].

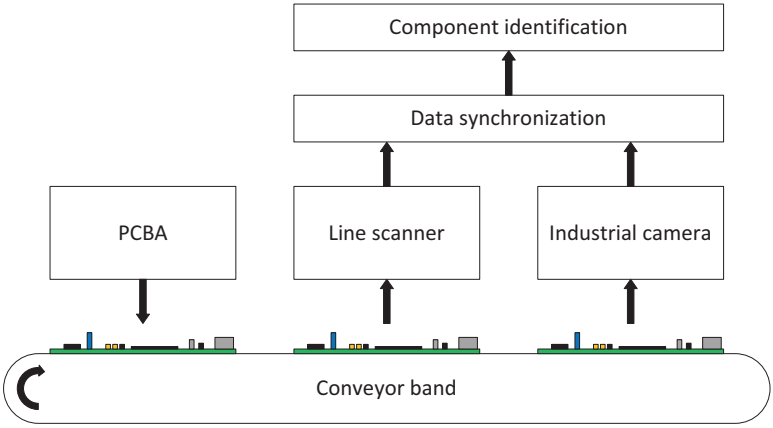

Figure 5.1: Scheme of the pilot plant.

3 Features and descriptors

The first step in detecting components on PCBs is to select a few distinct discriminative features to reduce the amount of data in the evaluation process. These features have to represent the components in a low-dimensional feature space in a way that the component classes are distinguishable among themselves. After testing complicated feature descriptors like Histogram of Oriented Gradients (HOG), Principle Component Analysis (PCA) or Local Binary Patters (LBP) the presented

approach was chosen. It yields good results with rather simple features based on shape, area overlap, total area, color, and height.

To extract the features of each component on the PCBA, the 2D and 3D data streams are cut, synchronized and preprocessed with different algorithms. The preprocessing of the images comprises a separation of the components from the PCB plane, a filtering using customized morphing operations, and the application of a Binary Large OBject (BLOB) algorithm. The preprocessing methodology is also described in detail in [8].

The output of these algorithms are point-clouds made up of individual 2D and 3D measurements, which can be exemplarily seen in figures 5.2a and b. Each cloud represents one component, for example a chip or a capacitor.

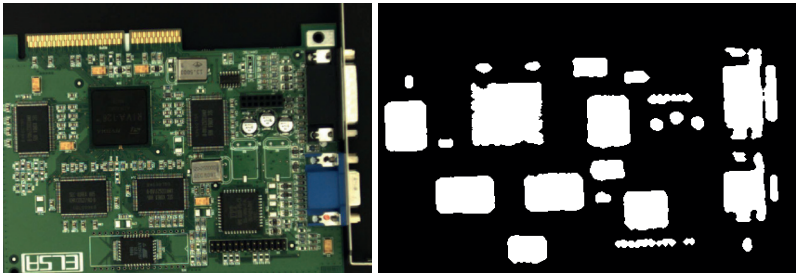

(a) Cut color image. (b) Morphed component binary image.

Figure 5.2: Preprocessed 2D and 3D data.

Based on these clouds the shape (i.e., rectangular or circular), the fitting in this shape, the average color (RGB), the cloud size and the mean height are calculated and put into a single descriptor pictured in figure 5.3a. The descriptor function is denoted as Φ and enables a distinct mapping to the subspace shown in figure 5.3b.

4 Classifiers

In machine learning applications a model is built in order to achieve the best possible classification. For this purpose, two data sets, namely train data and test data are required to create and validate the model.

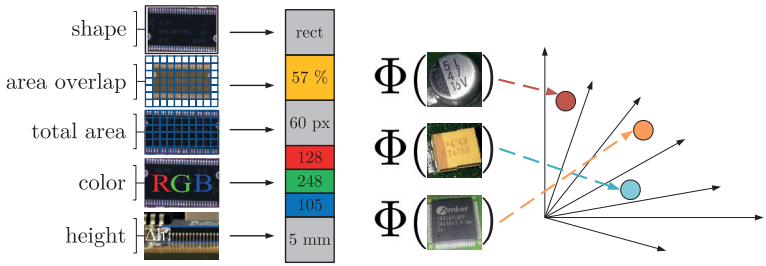

(a) Structure of the descriptor Φ. (b) Transformation into subspace.

Figure 5.3: Feature description and exemplary application.

While supervised learning algorithms get the true class to iteratively compute the actual model deviation, unsupervised ones seek for key features within data to classify autonomously. The training is performed using supervised learning methods to ensure sorting into predefined classes. To validate the created model test data is classified to measure the generalization error. A smaller deviation characterizes a better model.

The performances of the previously illustrated descriptors are compared using three different classification systems. Beside the classical approach with a Support Vector Machine (SVM) we also used an Artificial Neural Network (ANN) approach as well as the popular Random Forest (RF) approach. The SVM computes a hyperplane to separate the data into subspaces. Since the common SVM is only able to divide two class problems, a combination of SVMs is required to handle multi class problems. The basic scheme of an ANN is built out of three neuron layers, consisting of input (features), hidden (computation), and output (classes) layers. The neurons are connected with adaptable weights to incrementally improve the ANN. The RF is based on a variety of Decision Trees (DT) randomly built using fractions of the data set. A DT basically determines whether a sequence of conditions is fulfilled or not. The elected result of several diverging DTs declares the final result of the RF.

5 Results

The classification of the proposed descriptor yielded promising results. The evaluation was conducted using the software WEKA produced by the Waikato University of New Zealand. It allows for an easy and parallel evaluation of various classification algorithms [9]. For comparing the different classifiers one can choose from several options. The most common parameters are the receiver operating characteristics (ROC) and the corresponding area under the curve (AUC), respectively. Furthermore Cohen's kappa coefficient as well as the precision-recall curve (PRC) can be applied.

The ROC is a normalized curve with the true positives (TP) on the y-axis and the false positives (FP) on the x-axis. TPs are the members of a class A which are also correctly classified as member of A. FPs are members of other classes, e.g., B or C, but are classified as members of A. Usually, every classifier has some kind of hard threshold for separating the results into classes, which can be chosen. Each threshold leads to a different TP and FP rate. Therefore, varying the threshold generates the ROC curve. The AUC is now computed by calculating the area under the ROC curve using integration. The AUC typically varies from 0.5, which means guessing the classes, to 1, which stands for an excellent result. The kappa coefficient measures the agreement of a classifier with the ground truth with regard to the agreement by chance. The result is also normalized by the agreement by chance leading to a typical output range from 0 to 1, whereby 1 means total agreement. The PRC is a plot with the precision on the y-axis and the recall on the x-axis. Precision describes the ratio of TPs to the sum of TPs and FPs, whereas recall is the ratio of TPs of a class to the sum of its members. For evaluation the AUC is also calculated. The values range from 0 to 1 with 1 denoting a perfect result. The results are shown in tables 5.1 and 5.2. Table 5.1 shows the confusion matrix for the classification result of the proposed descriptor using a RF and five distinct classes. In table 5.2 the outcome for all three classifiers is characterized by the values of κ, ROC AUC, and PRC AUC. Both the ROC AUC and PRC AUC yield class-wise results. Therefore, only worst class results are displayed. Overall, the best outcome (highest values) is obtained for the classifier RF. The results were based on a total of 939 instances using two thirds for training and one third for testing.

Table 5.1: Confusion matrix generated by RF for five classes and unclassified.

a	b	c	d	e	f	← classified as
45	0	0	0	0	0	a = electrolytic capacitor
0	8	0	0	0	0	b = tantalum capacitor
0	1	118	1	3	3	c = integrated circuit
0	0	0	7	2	1	d = oscillator
0	0	1	0	47	4	e = plug
3	0	2	0	7	66	f = unclassified

It is evident that the RF yields the best results. It is also the fastest classification algorithm and can be parallelized easily. In a probable business case, i.e., the identification of tantalum capacitors, the classification rate is even better. The main reason for this behavior is the existence of only one class and its opposite. Compared with the multi class classification the RF reaches 0.93 for κ and 0.99 for ROC AUC and PRC AUC. The next steps to be taken are a testing of features with a medium complexity, e.g., histograms, and an expansion of the database.

Table 5.2: Comparison of classifiers.

	κ	ROC AUC	PRC AUC
RF	0.88	0.98	0.93
SVM	0.84	0.92	0.67
ANN	0.79	0.86	0.70

6 Summary

In order to cope with the global future demand of rare earths, it is urgent to raise the corresponding recycling rates. This paper proposed an approach for the recovery of valuable materials from PCBAs. It is based on a targeted optical identification of components containing valuable resources on PCBAs. These may then be selectively removed from the PCBA yielding a recyclable amount of materials. This approach requires the setting up of an automated selective disassembly plant. The identification can be based on an automatized recognition

plant using 2D and 3D sensors. The synchronized and preprocessed data is transformed into a subspace such that the quantity of information is reduced. The transformation is performed by the presented feature descriptor Φ, which consists of only the relevant component attributes (shape, fitting, area, color and height). This data functions as input for machine learning algorithms (SVM, ANN and RF) to evaluate their classification rate. In the application of the descriptor function Φ for PCBAs, the RF leads to the best results for a data set consisting of five distinct classes and unclassified components.

A future industrial implementation of this detection methodology combined with an automated disassembly plant represents a promising step towards the recycling of rare earths, especially the critical tantalum.

References

1. eMarketer. (2016) Anzahl der Tablet-Nutzer in Deutschland von 2010 bis 2015 und Prognose bis 2020 (in Millionen). [Online]. Available: {https://de.statista.com/statistik/daten/studie/256712/umfrage/anzahl-der-tablet-nutzer-in-deutschland/}
2. Statistisches Bundesamt. (2015) Anteil der privaten Haushalte in Deutschland mit einem Computer im Zeitraum 1998 bis 2015 (Stand: 1. Quartal 2015). [Online]. Available: {https://de.statista.com/statistik/daten/studie/2596/umfrage/ausstattungsgrad-privater-haushalte-mit-einem-pc-seit-1998/}
3. United Nations University. (2015) Elektroschrott-Aufkommen in ausgewählten Ländern. [Online]. Available: {https://de.statista.com/infografik/2278/elektroschrott-aufkommen-in-ausgewaehlten-laendern/}
4. T. E. Graedel et al. (2011) UNEP Working Group on the Global Metal Flows, Recycling Rates of Metals, A Status Report. [Online]. Available: {http://www.unep.org/resourcepanel/portals/24102/pdfs/metals_recycling_rates_110412-1.pdf}
5. J. Wang, J. Ruecker, H.-X. Hesch, U. Bochtler, and P. J. Klar, "Analyse von elektronischen Altgeräten im Hinblick auf verbesserte Recyclingverfahren," in *Jahrestreffen der ProcessNet Fachgruppen Energieverfahrenstechnik und Abfallbehandlung und Wertstoffrückgewinnung*, DECHEMA e.V., Ed., 2016.
6. J. Ruecker, H.-X. Hesch, U. Bochtler, and P. J. Klar, "An Empirical Approach for More Effective Recycling of Electronic Components in WEEE," in *7th*

Sensor-Based Sorting & Control 2016, T. Pretz and H. Wotruba, Eds. Herzogenrath: Shaker, 2016, pp. 249–258.

7. T. Koch, M. Breier, and L. Wei, "Heightmap generation for printed circuit boards (PCB) using laser triangulation for pre-processing optimization in industrial recycling applications," in *Industrial Informatics (INDIN), 2013 11th IEEE International Conference on*, 2013, pp. 48–53. [Online]. Available: http://ieeexplore.ieee.org/stamp/stamp.jsp?arnumber=6622856
8. J. Ruecker, H.-X. Hesch, U. Bochtler, and P. J. Klar, "Automated Segmentation of Electronic Components on Waste Printed Circuit Boards," in *7th Sensor-Based Sorting & Control 2016*, T. Pretz and H. Wotruba, Eds. Herzogenrath: Shaker, 2016, pp. 179–185.
9. Machine Learning Group at the University of Waikato. (2016) Weka 3: Data Mining Software in Java. [Online]. Available: {http://www.cs.waikato.ac.nz/ml/weka/}

Quality inspection on recycled coarse aggregates using laser-induced breakdown spectroscopy

Han Xia[1] and Maarten C. M. Bakker[1]

Delft University of Technology, Group of Resources & Recycling,
Stevinweg 1, 2628 CN Delft

Abstract Single-shot LIBS was applied for inline quality inspection of RCA (4–12 mm) transported on a conveyor belt at 0.5 m/s and 30 tonnes/hour under industrial operational conditions. Major granular contaminants, e.g. brick, gypsum, rebar, plastic and wood were classified of which classification errors were within the regulated contamination limits (e.g. 0.2–2 cm^3/kg for float and 1–5 *wt*% for sink contaminants). To this end, we first designed a LIBS prototype (without auto-focusing) with a large depth field ($\pm$ 4 mm) complying with the stream surface height fluctuations to increase the single-shot sampling rate up to 95 %. Second, PLS-DA classification model was validated using manually prepared material batches. The quality (cm^3/kg or *wt*%) of new concrete cast using these material batches, e.g. mechanical strengths were correlated with the LIBS data (number of classified LIBS spectra). It is shown that the LIBS technology is potentially capable of providing efficient, automated real-time quality inspection on RCA in-situ.

Keywords: LIBS, single-shot, inline, classification, recycling, aggregate.

1 Introduction

Construction and demolition waste (C&DW) is characterized by high volumes ($>$ 300 Mt/year in EU27 in 2012 [1]) at low material value per

[1] Eurostat

unit mass. In general, the profit margins in industrial C&DW recycling and the markets for the recyclable materials are under pressure [2]. This may largely be attributed to the fact that the quality of the recovered materials by the traditional industrial recycling processes is uncertain at best. This applies especially to RCA that can potentially be reused in the manufacturing of new concrete, which secondary materials are the main target in this work. The way forward to a successful concrete recycling operation is to maintain high throughputs in processing while assuring a consistent RCA product quality that can be proven to comply with accepted standards. This strategy will lead to higher volumes of RCA's to become available as cost effective, high-quality secondary building materials for new concrete production.

To realise the strategy, reliable and efficient quality control technology is required in-situ, i.e. in conjunction with the primary process. The control technology must automatically and continuously check the product stream of concrete aggregates for levels of cross-contamination that are left from the building demolition process and are not properly mitigated by the specialised aggregate cleaning technologies. However, to date, the lack of efficient inline quality inspection capability has been a major obstacle.

In this study, a sensor platform based on LIBS was developed and demonstrated for inline quality inspection on RCA at industrial scale. Material batches with known contamination levels were manually prepared to test if the partial least squares discriminant analysis (PLS-DA) model can achieve classification errors of major contaminants within their contamination limits according to the standard. Moreover, the relation between the LIBS and the quality data of the new concrete cast using these RCA batches was investigated.

2 Inline LIBS prototype-integration into the closed-loop recycling of RCA

Similar to the LIBS setup in [1], Fig. 6.1 shows the schematic of LIBS sensor platform designed for inline inspection of the 4-12 mm RCA.

[2] In the Netherlands, recycled concrete aggregates are sold for 12 euro /tonne on average to replace primary river gravel in new concrete. The processing costs are about 8-10 euro /ton and material transport adds 0.10-0.15 euro /ton/km.

The surface roughness of RCA transported on the conveyor is determined by a laser triangulation sensor as $\pm$ 4 mm. An optimised mismatch between the focuses of the laser and the parabolic mirror enables enough depth of view to prevent the need for an auto-focusing lens system. The Nd:YAG 1064 nm laser fires at the maximum repetition rate of 100 Hz at a fixed point perpendicular to the belt to ablate a small amount of material from the aggregate that passes the focus of the laser lens. This produces a tiny cloud of plasma ($\sim$ 1mm diameter) just above the aggregate surface. This very short-lived plasma (microseconds) cools down and transmits light with a spectrum that is characteristic for the material. After implementing a supervised classification algorithm using a reference LIBS spectral database, the acquired LIBS spectrum uniquely identifies the material at hand.

Still, several challenges had to be addressed to bridge the gap between laboratory research into LIBS that lead to an industrial adaptation towards a robust and compliant LIBS platform for inline inspection of RCA. The LIBS prototype was shielded and encased to protect it from weather influences and ADR dust as shown in the bottom-left inset in the inset of Fig. 6.1. The platform was set up in mechanical isolation from the ADR machine that produced quite heavy vibrations by being mounted on top of a stack of large concrete blocks resting directly on the ground. The incident laser beam and plasma light collection unit were guided by a sealed metal tube onto the RCA stream on the conveyor belt. This laser tube also provided a safe working environment for the personnel in accordance with class 4 laser safety regulation. A fast camera was integrated into the LIBS platform to be able to monitor the amount of material on the conveyor belt (belt speed $\pm$ 0.5 m/s) and to check the laser-optics settings. The inline LIBS prototype platform, consisting of hard- and software, has been demonstrated in Hoorn, the Netherlands on 10th June 2016 to collect and analyse LIBS data in a real-scale industrial concrete recycling plant, and was operated above the ADR coarse output (4-12 mm) conveyor belt that carried 30 tons of RCA per hour [3].

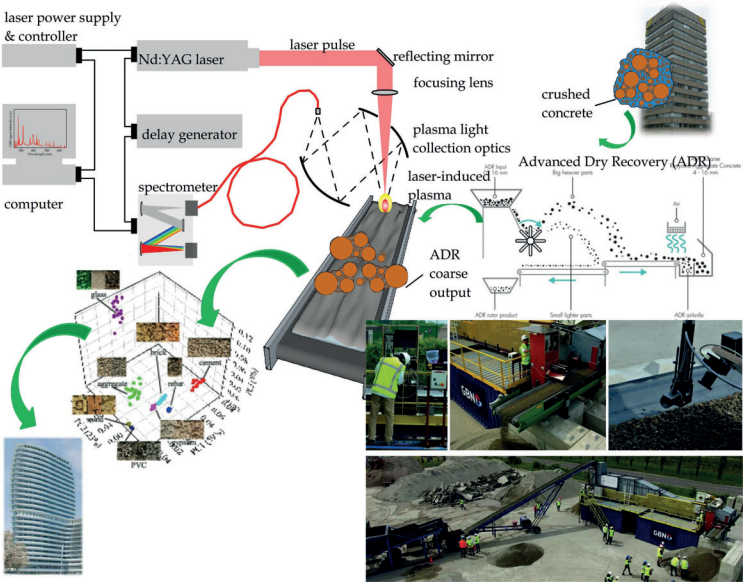

Figure 6.1: Principle and deployment of the inline LIBS platform into the closed-loop recycling of RCA. Inset photos: installation and implementation of inline LIBS sensor platform in Hoorn, the Netherlands on 10th June 2016.

3 Results and discussions

In parallel to the in-situ demonstrations, special batches of recycled aggregates (cf. Tab. 6.1 and Fig. 6.3a) were prepared and inspected using this LIBS platform. Several RCA batches were prepared as follows: 300 kg demolition concrete (0-44 mm) was sieved manually to 4-16 mm to obtain 160 kg materials. This was equal-partitioned into 4 fractions of 40 kg according to the European standard EN 932-2 [2]. Of each of these fractions, 10 kg was subjected to handpicking to determine the material composition according to the European EN standard 933-11 [3]. The major components in the sink fraction (0.63 ± 0.23 $wt\%$) were brick, glass, PVC, rebar and gypsum. The major components in the float fraction (1.29 ± 0.24 cm^3/kg) were wood and foam. The re-

[3] Video available at: `https://www.youtube.com/watch?v=lHp3G-lOoOs`

Table 6.1: Five sets of self-made RCA (4-16 mm, 30 kg) with varying contamination levels.

#Sample	Sink $[wt\%]$	Float $[\mathrm{cm}^3\mathrm{kg}^{-1}]$	Comments
1 Reference	0.63 ± 0.23	1.29 ± 0.24	Recycled aggregate
2 Low sink, high float	< 1	2	Add extra 30 cm^3 float
3 High sink, high float	5	2	Add extra 30 cm^3 float and 1.5 kg sink
4 High sink, low float	5	< 0.2	Clean the float, add 1.5 kg extra sink
5 Low sink, low float	1	< 0.2	Clean the sink and float, add 0.3 kg gypsum

Table 6.2: PLS-DA classification errors using 15 components.

	PVC	brick	RCA	glass	gypsum	foam	wood	rebar
PVC	678	0	0	0	0	0	0	0
brick	0	676	0	0	0	0	0	2
RCA	0	0	678	0	0	0	0	0
glass	0	2	0	676	0	0	0	0
gypsum	0	0	1	0	677	0	0	0
foam	0	1	0	0	0	676	1	0
wood	1	0	0	0	0	3	674	0
rebar	0	0	0	0	0	2	0	676

maining 30 kg of each of the four fractions were modified manually as shown in Tab. 6.1 to improve the detectability of pollutant levels with LIBS and also to enhance the likely correlation with the quality of the produced new concrete samples.

3.1 PLS-DA classification model

We used a PLS-DA model [4][4] to determine the sensitive LIBS parameters by minimising the classification errors. To this end, we collected training datasets (i.e. LIBS data from reference aggregate batches and materials with well-known material composition) by selectively intro-

[4] using plsregress function, MathWorks® Matlab 2015b

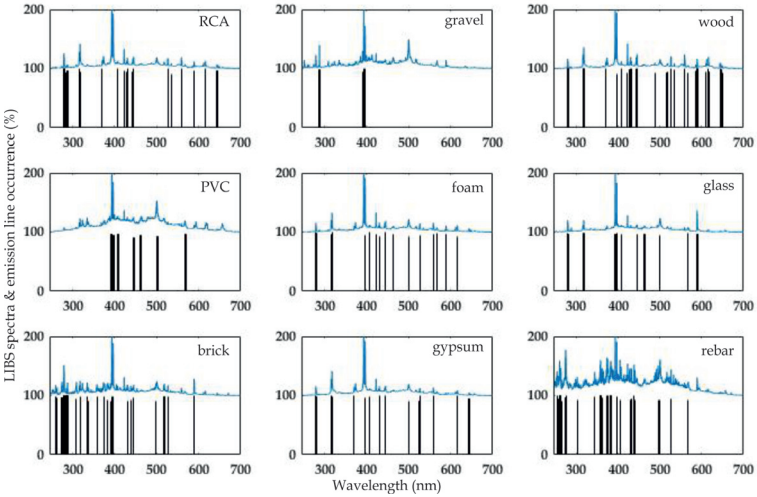

Figure 6.2: LIBS spectra (normalised to maximum as 100% and the occurrence of emission lines [%] observed for RCA, natural gravel (as a reference), and various pollutants handpicked from the concrete aggregates.

ducing more data variations, such as using larger optics-to-sample-surface distances or adding more material types. Each single-shot LIBS spectrum was normalised to its integral over the full wavelength range [5]. LIBS measurements were repeated three times per material batch, and each time 6000 single shot LIBS spectra were acquired at a rate of 100 per second while the laboratory conveyor belt shown was feeding at 30 kg/minute. Their raw LIBS spectra were shown in Fig. 6.2, in which emission lines with larger spectral occurrence $>$ 95 % (ratio of the number of spectra with identifiable emission line to the total spectra) were also shown underneath each LIBS spectrum. The emission line determination was described in [5]. It is noted that RCA is a new type of material of which the LIBS spectrum is more Ca-line-rich in comparison with that of gravel. During the collection of training data, we purposely introduced sample surface fluctuations larger than ± 20 *mm* to emulate the fluctuations observed under real-scale operations. The multi-classification PLS-DA model was trained using 60 components which results in a mean-square error of 0.104 with 5-fold

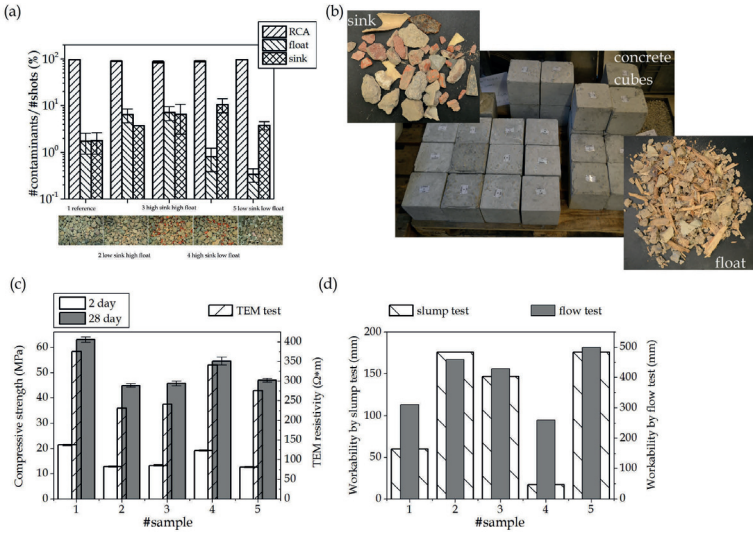

Figure 6.3: (a): Number of contaminants identified by LIBS, normalised to the total number of identified spectra. Results are for the five batches specified in Tab. 6.1, as shown in the photos underneath. The sink fraction contained PVC, brick, glass, gypsum, and rebar, while the floats contained wood and foam. The error bar represents 1STD, related to three duplicate measurements. (b): New concrete cubes cast using forenamed material batches and inherent sink and float contaminants. Quality tests on concrete cubes using five material batches (c): mechanical strength and (d): workability tests.

cross-validation. The classification errors are presented in Tab. 6.2. It is noted that the false-positive and false-negative errors for wood particles are 0.15 % (foam) and 0.59 %, respectively.

3.2 Relating LIBS parameters to the achieved quality of the new concrete

We first determine the contamination levels including composition and contents of the RCA's (4-16 mm) using LIBS. The results are shown in Fig. 6.3a as percentages of classified spectra, which agree rather well with the known material compositions. It is noted that the 1 % count

ratio of floats corresponds to 2 cm^3/kg float contaminants and 1 % count ratio of sink materials corresponds to 1 wt% sink contaminants. The last two batches were cleaned using a sink-float separation before adding extra contaminants to reach the desired contaminant composition. Therefore, the float contents in those batches are lower than the float contents of the original coarse aggregates batch from which they were derived.

We then investigate the influence of contamination levels on the quality of the newly produced concrete cubes shown in Fig. 6.3b. The classified number of shots for each type of material proved proportional to the particle size, regardless of its specific shape. Furthermore, the number of particles can simply be transferred into contents (*wt*%) or volume percentages (cm^3/kg) since the average mass densities of all the materials are known.

To test the quality of the concrete cubes the following quality parameters were selected: 2 day and 28 day mechanical strengths were tested in the ENCI quality assessment lab [5], the electrical resistivity was measured using a two-electrode method (TEM), and the workability was determined using slump and flow tests. The recipe used to produce the C30/37 XC3 F4 class strength concrete was as follows: a mixture of cement using CEM I 52.5 N (80 kg/m^3) and CEM III/B 42.5 N LH HS/SR (240 kg/m^3); 5 batches of coarse aggregate (915 kg/m^3); river sand (805 kg/m^3); water-to-cement ratio of 0.54, and super-plasticizer (1.92 kg/m^3). Per batch 30 kg was used for 6 test cubes (150 mm) to determine the workability and mechanical strength (Fig. 6.3c). The error bar represents one standard deviation as obtained from three concrete cubes per type of test. The white bar indicates the 2-day compressive strength; the dark grey bar the 28-day compressive strength and the dashed bar the resistivity using TEM. In the workability tests (Fig. 6.3d), the dashed bar indicates the slump workability, and the light grey bar the flow workability. It is clearly shown that the trends of the 2- and 28-day mechanical strength and TEM values are similar. The resistivity may be assumed inverse proportional to chlorides ingress rate at room temperature [6]. The reference sample shows the highest strength and largest resistivity. The high-sink, low-float batch shows the second best performance, where the brick is the major sink contaminant. This in-

[5] Company webpage: `http://www.enci.nl/nl`

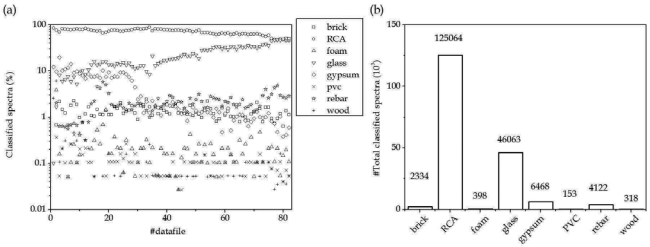

Figure 6.4: (a): Percentages of classified contaminants of each sampling burst in RCA over time. (b): Total number of classified contaminants in RCA.

dicates that brick degrades the strength and resistivity only to a small degree. The low-sink, low-float batch consisting of 1 wt% gypsum indicates that gypsum affects the concrete strength and resistivity more than brick, despite the fact that the gypsum contents were lower. Compared with brick and aggregate, gypsum is more brittle and its breaks down easily during the mixing procedure for making cement paste. According to its high workability, the gypsum batch may absorb less water. The second and third batch show similar strength and resistivity, indicating that the float contaminants are the major components that degrade concrete performance. They may also reduce water absorption when looking at the high workability.

3.3 Inline LIBS classification results on RCA

During the Hoorn demonstration, 60 tonnes of coarse aggregate products was processed by the ADR and inspected by the LIBS platform. Fig. 6.4a shows the classified numbers of LIBS spectra [%] in real-time over 82 sampling bursts. In total, 195235 LIBS single-shot spectra were collected of which 184920 shots could be properly classified, amounting to a 95 % success rate in LIBS sampling. As indicated in Fig. 6.4b), 125064 were classified as concrete aggregates, 2334 as brick, 6468 as gypsum, 4122 as steel rebar, 398 as foam, 318 as wood and 153 as PVC plastic. Using the previously determined correspondence between 1 % LIBS classification percentage and 1 cm^3/kg concentration of float contaminant, and taking wood as the most critical float contaminant in the

RCA market, the identified particles content accounted for 0.172 % of all particles which corresponds to a wood volume contamination level of < 0.2 cm^3/kg of aggregate product. This level complies with category $FL_{0.2}$ according to European-EN standards [3,7] for floating pollutants in concrete. It is remarked that this level complies accurately with the handpicking and float analysis results for a 10 kg sampler from the demonstration site.

4 Summary

In this present work, a LIBS prototype was set up for RCA recycling that achieved a sampling rate of 95 % by virtue of its long depth of field, corresponding to the surface roughness of RCA ($\pm$ 4 *mm*). Using normalised LIBS spectra as inputs, a PLS-DA multi-classification model was trained and validated on manually prepared RCA batches with different contamination levels (1-5 wt% for sink and 0.2-2 cm^3/kg for float contaminants). Same batches were then employed to cast into the new concrete, and their quality data were well-correlated with their LIBS classification results. Finally, this LIBS technology was employed for inline quality inspection of RCA (4–12 mm) at industrial scale (throughput of 30 tonnes per hour at transport speed of 0.5 m/s).

Acknowledgement

This work was financially supported by the European Commission in the H2020 collaborative project HISER, Grant Agreement No. 642085.

References

1. H. Xia and M. Bakker, "Reliable classification of moving waste materials with *libs* in concrete recycling," *Talanta*, vol. 120, pp. 239–247, 2014. [Online]. Available: http://www.sciencedirect.com/science/article/pii/S0039914013009703
2. *European Committee for Standardization, EN 932-2: Tests for general properties of aggregates - Part 2: Methods for reducing laboratory samples*, Std., 1999.

3. *European Committee for Standardization, EN 933-11: Tests for Geometrical Properties of Aggregates - Part 11: Classification Test for the Constituents of Coarse Recycled Aggregate*, Std., 2009.

4. S. De Jong, "Simpls: an alternative approach to partial least squares regression," *Chemometrics and intelligent laboratory systems*, vol. 18, no. 3, pp. 251–263, 1993. [Online]. Available: http://www.sciencedirect.com/science/article/pii/016974399385002X

5. H. Xia and M. Bakker, "Single-shot libs spectral quality for waste particles in open air," *tm-Technisches Messen*, vol. 82, no. 12, pp. 606–615, 2015. [Online]. Available: http://www.degruyter.com/view/j/teme.2015.82.issue-12/teme-2015-0042/teme-2015-0042.xml

6. C. Alonso, C. Andrade, and J. Gonzalez, "Relation between resistivity and corrosion rate of reinforcements in carbonated mortar made with several cement types," *Cement and concrete research*, vol. 18, no. 5, pp. 687–698, 1988. [Online]. Available: http://www.sciencedirect.com/science/article/pii/0008884688900919

7. *European Committee for Standardization, EN 12620+A1: Aggregates for Concrete*, Std., 2008.

Concentration determination for sorting applications using dual energy X-ray transmission imaging

Markus Firsching, Julija Lucic, Alexander Ennen and Norman Uhlmann

Fraunhofer IIS,
Development Center X-ray Technology,
Fürth, Germany

Abstract Dual Energy X-ray imaging is a method to provide quantitative information about the examined material. With Fraunhofer EZRT's Dual Energy technique it is possible to determine the concentration of a specific material in an object. This is realized through the Fraunhofer Dual Energy algorithm, which is using two X-ray spectra and/or spectral detector efficiencies for Dual Energy X-ray imaging. In this way, an areal mass density is obtained and the fraction of the mass of two given materials that differ in atomic number can be determined. This information can be used for material characterization. So X-ray Dual Energy can also be useful in industrial applications, for example to reduce the contamination of wood chips by plastic pieces. In general, differentiation is difficult in terms of gray values or shape. Here the Dual Energy method shows advantages. An overview on the method will be given as well as an introduction to current and future fields of application. The results from the test case of differentiating wood from plastics are presented and discussed.

Keywords: X-ray, dual energy, concentration of materials, separation of materials, material characterization, transmission imaging, radiographic imaging.

1 Introduction

Dual Energy X-ray imaging has proven to be valuable technique to acquire quantitative material properties from computed tomography (CT) or radiographic images. In contrast to standard measurements it is able to provide additional information about the atomic number (Z) or the density of the irradiated material. Since the 70's [1] these methods have been developed and evolved. Its main applications lies in medical and security applications like airport cargo scanner but it has not yet been commonly used in non-destructive testing (NDT). Its ability to determine the concentration of distinct materials within certain types of material compositions has widened its usage to different branches of application like sorting and recycling.

Dual Energy images are created by acquiring two X-ray images of the same sample at different spectral parameters. While standard X-ray images only allow to separate different materials on their attenuation of the X-rays and thereby struggle with varying radiation thicknesses, Dual Energy methods enable one to separate certain materials independently of the irradiated thickness of the specimens. Furthermore Dual Energy can be used to enhance the contrast of different materials which provide only low contrast in conventional X-ray imaging.

The ability to derive quantitative information from the images can also be used to calculate the concentration of materials in relationship to the entire specimen. This is of particular interest for several applications [2]. It can also be used to assert the presence of materials within hosting materials like diamonds in kimberlite [3].

2 Motivation

Single-variety separation of plastics is a crucial task for the sorting industry. This is especially true for black plastics which cannot be separated by optical techniques. Besides that, plastic contaminations in streams of material are challenging to detect and separate for other applications as well. In streams of biowaste for example plastic contaminations represent a crucial problem for the quality of biogas or humus production. Likewise the lumber industry is challenged by plastic leftovers or compound materials within the processed timber streams.

While the separation of wood from plastics provided promising results, some kinds of plastics could not be separated from wood. In order to categorize different types of plastics which can be separated from those which can't, very pure specimens of different plastics were measured and analyzed.

3 Dual Energy Method

Dual Energy in sorting or recycling tasks is primarily used to derive physical quantities from X-ray images. This is based on the fact that the total attenuation coefficient depends on the energy of the X-ray as well as on the penetrated material. In order to acquire X-ray images sufficient for Dual Energy algorithms at least two images of the same object with different spectral parameters have to be acquired. Different spectral parameters can be achieved by either changing the acceleration voltage of the tube (kV-Switching), using different filter materials for each image or by using a Dual Energy detector which is capable of acquiring two images at the same time. Changing the filter between two acquisitions is hard to achieve in industrial sorting environments and is therefore impracticable. Rapid kV-Switching is possible in sorting applications but requires exact timing of the system and is limited in regards to belt speed and lifetime of the system. It is however used for Dual Energy attempts for CT. The commonly used method for sorting on belt or chute systems is therewith the usage of Dual Energy detectors. When processing Dual Energy algorithms, information based on the penetrated material can be obtained. In fact Fraunhofer EZRT Dual Energy algorithm is able to derive the areal density ρ for two materials from those measurements. Based on this calculated areal density it is possible to calculate the concentration of one of this materials within a compound of different materials.

This is based on Lambert-Beer's law describing the attenuated intensity after an object as

$$I = I_0 * \exp(-\mu' * \alpha) \tag{7.1}$$

where μ' is the attenuation coefficient, α the areal density and I_0 the non-attenuated intensity. While penetrating more than one material at a time, the attenuation coefficients sum up. Acquiring two (or more)

images at different spectral parameters leads to a set of similar equations which describe the extinction of the same material at different energies. This leads to

$$I_k = I_{0k} * \exp(-\mu'_{jk} * \alpha_j) \tag{7.2}$$

where k indexes different energies and j being the index of the material. This approach summarizes all X-ray attenuation effects which includes Compton scattering and photo-electric absorption.

When using a non-monochromatic X-ray source the intensity captured by the detector can be described utilizing the detector efficiency *D(E)* and the emitted spectra *S(E)*

$$I_0 = \int dE * S(E) * D(E) \tag{7.3}$$

In order to utilize this attempt the used spectra and the detector efficiency has to be known. This dates can be achieved by simulation or measurement techniques. While measuring is tougher than simulation it may lead to better results. Using this in the equation above leads to:

$$I = \int dE * \exp(-\mu'(E) * \alpha) * S(E) * D(E) \tag{7.4}$$

With obtained spectra *S(E)* and detector efficiencies *D(E)* the areal densities α_j can be calculated. This requires a selection of materials upfront. Using this for two materials leads to two equations with can be solved under certain conditions and result in two areal densities for those chosen materials. This also enables the calculation of material concentrations.

4 Measurement setup and specimens

In order to perform measurements based on industrial environment the specimens were measured in movement using a drawer system mounted on a linear xy-axis system. The system as well as the used Dual Energy line scan detector (C10800-09FCM-C) were provided by Hamamatsu. All tests were performed using a high power X-ray source with an acceleration voltage up to 225 kV. To compare also the method

of kV-Switching to the results gathered from the Dual Energy detector, repetition measurements with varying kV were used. All specimens where analyzed using 50kV, 70kV and 100 kV. Dual energy measurements where performed analyzing all three different spectra. For rapid kV-switching the acquired projections where registered and only the low-energy channel was used to compare different accelerating voltages. The first application to be analyzed was the detection of contamination of wood by plastic pieces. In this case the type of the plastics is unknown. It is not necessary to identify different types of plastics, only the separation from wood is important. In order to characterize different types of plastics and make a assertion about which can be separated from wood, pure plastic specimens of the following types were analyzed as well. Table 7.1 describes the different types of plastics used for the analysis.

Table 7.1: Different types of plastics used for the analysis.

Specimen	Density ρ [g/cm^3]	Grain size [μm]
UHMW-PE	0.94	150
UPVC	1.4	250
PS	1.05	250
PMMA	1.19	600
PTFE	2.2	675

5 Results

To separate plastic leftovers from wood the provided pieces were irradiated and analyzed. Figure 7.1 shows the plastic pieces on the left and the wood chips on the right. Both materials provide a similar contrast in a standard X-ray radioscopy image. A differentiation between both materials can hardly be achieved.

The resulting X-ray Dual Energy image of higher Z material is shown in Figure 7.2. While the lower Z-materials blur out of the image, higher Z-materials appear brighter. All plastics except the one in the upper left corner appear bright in contrast to the wood, which appears dark in this image. Using Dual Energy analysis the differences between atomic

numbers of the specimens clearly enhanced the possibility to separate both types of material to a certain amount.

Since not all plastic types could be separated from the wood, measurements with different pure and known plastics were performed to determine how good the separation of plastics and wood with the Dual Energy method works. Table 7.1 displays the used materials and their densities. The plastics were fine grained and uniformly filled in a culture dish so that the fill level of all plastic samples was similar.

Figure 7.3 displays the Dual Energy results of the pure plastic specimens in pseudocolor. The specimens contained in the culture dishes are the following from left to right:
Top line: rubber, PMMA and wood sample;
Bottom line: PTFE, UPVC, UHMW-PE and PS.

The pseudocolor image indicates differences between some of the specimens but also shows that certain types of plastics seem not to be distinguishable using Dual Energy. While rubber, PTFE and UPVC seem to be clearly separable from wood and the other three specimens (PMMA, UHMW-PE and PS) the specimens on the right side of figure 7.3 show only minor differences among themselves. They also only display minor differences in respect to the wood sample.

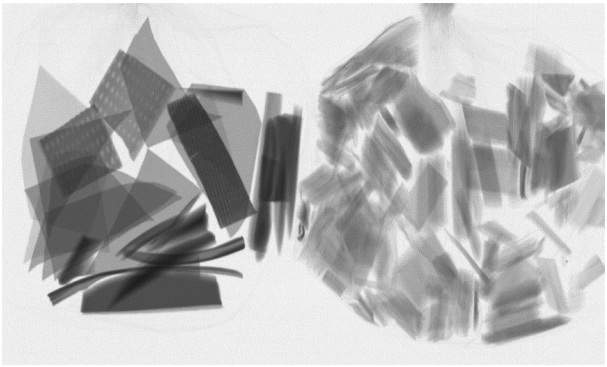

Figure 7.1: X-ray image of plastic pieces (left) and wood chips (right).

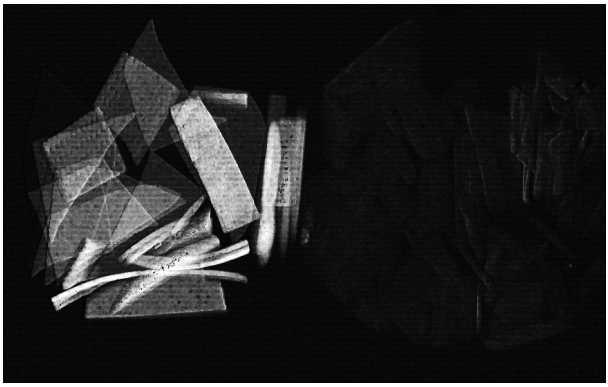

Figure 7.2: Dual Energy X-ray image showing higher Z material (higher atomic number). Most plastics appear bright.

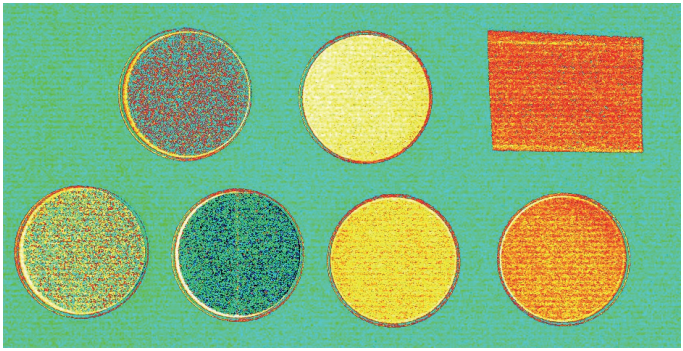

Figure 7.3: Pseudocolor image of different plastics displaying the areal densitiy using both energy channels of the detector.

It is to consider that the height of the specimen and thereby the irradiation path is known in this laboratory measurements. While the output of the Dual Energy algorithm is the product of material height and density, this additional information is key to separate those materials. In industrial environment scraps of varying size must be processed. Separability under this circumstances is only achievable if such additional information is available. This could be obtained by optical measurement systems for example.

In comparison to the results from the Dual Energy detector, figure 7.4 illustrates the areal density for the same specimen using kV-switching. As with the results from figure 7.3 UHMW-PE and PS are hard to separate from the wood sample. In addition PTFE appears homogeneous in its areal density and is also not easily separable from wood. For our setup, test samples and algorithms kV-switching does not offer any advantages over the direct usage of both Dual Energy detector channels.

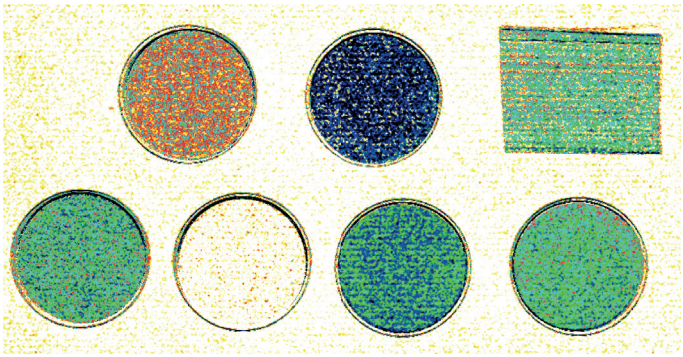

Figure 7.4: Pseudocolor image of different plastics displaying the areal density using different energies on the same detector channel.

6 Summary

While first tests indicate that the separation of plastics from wood seem to be achievable, testing distinct and pure plastic specimen outlined that this may not be possible for all kinds of plastic samples. In order to enhance the capability of separation additional information like the height of the sample is needed. This could be achieved utilizing optical measurement systems and seems to be practicable in industrial application as well.

The results provided by the measurements using (rapid) kV-switching seem not to compensate for the fact that it is hard to accomplish in sorting environments and moving systems. It may however proof valuable for CT applications.

7 Outlook

As indicated by the results, it is not ultimately clarified that all sorts of plastics and wood can be separated. Though the results are promising, there have to be further investigations with real industrial specimens. To find out if the results are reliable enough for industrial applications, the influence of the height of the object has to be clarified.

Another point which should be examined is the influence of the speed of the system to the accuracy of the imaging. The standard industrial belt systems use high speeds (approximately 3-3.5 m/s). Increased belt speed may lead to a lower SNR in the acquired images and therewith reduce the precision of the attached Dual Energy algorithms.

Also the measurements comparing kV-Switching and Dual Energy imaging need to be investigated further to get a reliable information about the advantages of each method for industrial applications. The results with the used Dual Energy line scan camera showed no advantages using kV-switching, but these could possibly be achieved using other types of detectors or sources. The respective advantages and possibilities of these two methods are thus under investigation.

Acknowledgement

The authors would like to thank Hamamatsu Photonics [4] for providing the drawer system, the detector which was used for the testing and the ongoing cooperation.

References

1. R. Alvarez and A. Macovski, "Energy selective reconstruction in x-ray computerized tomography," in *Phys. Med. Biol. Vol. 21, No. 5 (1976), 733-744*, 1976.
2. M. Firsching, J. Mühlbauer, A. Ennen, and N. Uhlmann, "Dual energy x-ray imaging for computed tomography and sorting applications," in *1st International Conference on Tomography of Materials and Structures*, Ghent, Belgium, 2013.

3. M. Firsching, F. Nachtrab, J. Mühlbauer, and N. Uhlmann, "Detection of enclosed diamonds using dual energy x-ray imaging," in *18th World Conference on Nondestructive Testing*, Durban, South Africa, April 2012.
4. "Hamamatsu photonics," http://www.hamamatsu.com/eu/en/index.html, 07.01.2017. [Online]. Available: http://www.hamamatsu.com/eu/en/index.html

How to analyze food and future requirements for NIR spectroscopy

Peter Reinig[1], Heinrich Grüger[1], Susanne Hintschich[1], Jens Knobbe[1], Tino Pügner[1]

Fraunhofer-Institut für Photonische Mikrosysteme IPMS,
Maria-Reiche-Straße 2, 01109 Dresden

Abstract Food has been subject to various characterization methods for centuries. Optical characterization methods like spectroscopy were implemented long ago. Different requirements arise from integrity (contaminations, foreign objects, spoilage) and quality (composition) issues. In our modern world, automated optical tools are being used for several tasks, in particular for testing raw materials and for in-line monitoring of food processing. In the future new options for optical food analysis and inspection will arise. On site testing from "field to fork" drives the development of mobile analysis units for harvesting, transportation, storage and distribution, which will enable a more detailed control during processing. In addition, the consumer is interested in an on-site analysis using household or mobile devices. Here, market opportunities for hardware integrators, software engineering and data service providers are identified.

Keywords: Food analysis, NIR spectroscopy, product development.

1 Introduction

The most common method of analyzing food is organoleptic testing. A person is testing food without any technical means by assessing food with the human organs of perception. Thus, food is characterized by its taste, odor, appearance, color and texture. However, this method is subjective and highly related to the tester's practical experience and

capabilities. In the worst-case this method might be hazardous to the tester's health or even lead to death. Therefore, objective and quantitative methods for analyzing food are in great demand. Various approaches have led to the development of electronic noses [1] and electronic tongues [2], but both still have a far way to go to mimic the human nose and tongue.

Food condition is affected by the complex chemical composition of the food and can be addressed by optical characterization methods like spectroscopy. Especially optical vibrational spectroscopy has the potential for a rapid quantitative detection of food quality and food fraud both in the laboratory and in mobile applications along the food supply chain [3]. Two aspects are generally considered: First, microbiological and toxicological properties must be granted by the producer and distributor. Especially food spoilage due to microbes [4] and other biological [5] and chemical hazards [6] throughout the food chain are the most significant threats to food security within Europe. Here, sophisticated methods are required to meet the very low detection limits. Second, quality issues [7] such as ripeness, freshness and nutritional facts (i.e. sugar, carbohydrate, protein, fat and water) will differ and may change between processing and consumption. A favorable option to evaluate food composition is near infrared spectroscopy (NIR). Technically, the spectral range from 1000 to 2300 nm is most interesting. Relevant data is usually available in the 1100 to 1800 nm range, which can be addressed using standard sensors without compulsory detector cooling.

With the knowledge about suitable optical methods for food quality determination and their potential to go into the field it becomes important to draw a road map for the market entry. Based on the roadmap goals and tasks can be derived for the next steps in development. This concerns both hardware, software and data base. Thereby and by offering suitable solutions the application will be opened not only to dedicated food specialists but for also for common use.

2 How to analyze food

2.1 Basics

Based on a suitable sample preparation method, there is a large variety of analytical techniques available today. These range from biological (e.g. PCR, immunology) to separation (e.g. liquid or gas chromatography), spectroscopic (e.g. mass spectrometry, fluorescence, near-/mid-infrared, NMR), rheological (e.g. viscometry), thermal (e.g. DSC), radiochemical (e.g. isotopic) and electrochemical techniques (e.g. voltammetry) [A. Cifuentes 2012]. Spectroscopic techniques are based on energy selective interaction between electromagnetic radiation and the sample (or in the case of mass spectrometry on energetic filtering of sample constituents). Electromagnetic radiation in the infrared region (λ = 0.78 μm – 100 μm) interacts with molecules and leads to an energetic excitation of the molecules depending on the specific molecular structure. In the near-infrared (NIR, λ = 0.78 – 3.0 μm) and mid-infrared (MIR, λ = 3.0 – 30 μm) region this interaction leads to vibrational and rotational excitations of the molecules. "Nowadays, spectroscopic techniques based on infrared region are one of the most numerous in the food analysis. Thus, infrared spectroscopy is frequently used for quality control of food including analysis of honey ... or muscle food ...". [8]. NIR spectroscopy can contribute valuable information to food quality analysis. However, contaminations at low concentrations (ppm and below) must be detected via more sophisticated methods, which might be too expensive for widespread consumer use.

Different system approaches have been presented for NIR spectral analysis: Classical spectrometers offer superb performance but are bulky, expensive and sensitive towards environmental conditions. Diode array spectrometers with reduced size reveal favorable performance but still the cost issue limits their applications within NIR-based food sensing systems. Low cost devices have been realized using MEMS technologies. Filter based systems (e.g. Spectral Engines, Hamamatsu), digital light processors (e.g. TellSpec), scanning grating (Hiperscan) are some examples for miniaturized systems. However, spectral analysis means more than just applying a spectrometer. The evaluation of NIR spectra requires chemometric modelling based on reference data. In addition, database access is indispensable when ap-

Table 8.1: Hardware parameters of different NIR spectrometer devices.

Device	Size	Expected target price
Lab spectrometer	(30 x 25 x 15) cm^3 = 11 250 cm^3	
Hiperscan SGS 1900	(10.5 x 8.0 x 8.6) cm^3 = 722 cm^3	
Ocean Optics flame NIR	(8.9 x 6.3 x 3.2) cm^3 = 179 cm^3	
TellSpec (DLP based)	(9.0 x 6.0 x 2.5) cm^3 = 135 cm^3	
Next-gen MEMS spectrometer	(5.0 x 5.0 x 3.0) cm^3 = 75 cm^3	500 € @ 10 000 p.a.
IPMS SCS	(1.5 x 1.4 x 1.0) cm^3 = 2.1 cm^3	100 € @ 1 mio p.a.
Mobile phone (tbd)	(1.2 x 1.1 x 0.6) cm^3 = 0.8 cm^3	5 € @ very high volume

plying this method in the field. Therefore, progress in this area must coincide with hardware development.

For a future platform, the following components and requirements in addition to the spectrometer unit itself have to be taken into account: suitable light source(s), appropriate optical coupling with minimal losses, an integrated computational device for data acquisition and post-processing, data base access, internal memory or online data communication. Options could be systems mounted to machines as well as portable devices or even integration into smart phone or tablet. In the latter case size issues become relevant (see Tab. 8.1). The development effort for the next generation MEMS spectrometer is expected to be in the range of 0.5 Million Euros, the integration of SCS including ASIC design is expected at 3 million Euros, the development cost for spectrometer integration into a mobile phone needs to be specified yet.

2.2 Miniaturized spectrometer suitable for food analysis

Much work has been done to miniaturize NIR spectrometers in the past years. In particular, obtaining the relevant spectral range (λ = 950 - 1900 nm) with a suitable spectral resolution (better than 10 nm) while keeping the signal-to-noise ratio (SNR) sufficient (3.5 a.u. corresponding to 12 bit data depth) is a challenging task (here a.u. denotes absorbance unit, which is used in practice – however the ratio between incoming and transmitted radiation is dimensionless).

An example of how small an NIR spectrometer can be realized was demonstrated by Fraunhofer IPMS (see Fig. 8.1) with the stacked-

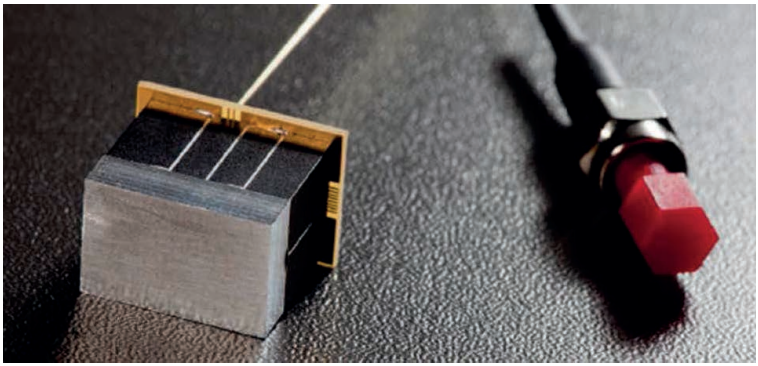

Figure 8.1: Stacked-component-spectrometer (SCS) by IPMS.

component spectrometer (SCS) in the size of a sugar cube using a scanning-grating MEMS chip [9].

The SCS is realized by stacking two key components: the MEMS/detector part and the spacer/mirror part. The basic idea behind this concept is to connect necessary spectrometer substrates (including micromechanical and optical functional elements) in a stacked manner. This enables a convoluted light path between both substrates [10].

Compared to the much larger commercially used system Hiperscan SGS1900, the IPMS SCS performs alike (Fig. 8.2 left) and exhibits a spectral resolution of less than 10 nm (Fig. 8.2 right) [9].

2.3 Food analysis using scanning grating technology

Application related measurements have been performed on selected use cases. One of these use cases is milk, representing a prominent example of food adulteration, especially in the Asian region. The scanning grating technology of IPMS has been tested for this application and measurement results are shown in Fig. 8.3, clearly giving access to fat content monitoring.

Further milk samples were deliberately spoiled with a variety of common adulterants in the Asian region (e.g. fructose, glucose, vegetable oil and detergent). First chemometrical models were developed in cooperation with Fraunhofer IOSB. The results of a principal com-

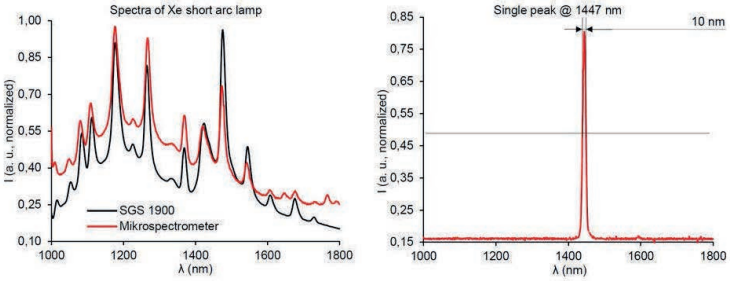

Figure 8.2: Performance comparison of IPMS SCS (microspectrometer) with Hiperscan SGS1900 (left) and spectral resolution (< 10nm) of the IPMS SCS (right).

ponents analysis (PCA) for the case of milk adulteration are shown in Fig. 8.4.

Common adulterants of milk measured with scanning-grating based NIR spectroscopy can be discriminated after PCA analysis.

3 Future requirements for NIR food analysis

3.1 Existing and future requirements

Several systems for food analysis have already been presented for selected applications (e.g. by Ocean Optics, TellSpec, Consumer Physics and others). However, to meet the customer demand in different application fields further research and development is still required. For example, the available spectral range must coincide with the relevant optical bands, especially for H2O (λ=1450 nm/1960 nm), C-C, C-H, C-O (1680 – 1820 nm). Whereas size, weight and usability are fair for systems on the market, price is still a big issue. Before considering development goals, the specific requirements of some use cases must be taken into account. Four different market segments with differing market entry conditions are discussed:

In line metrology – mounted devices

State of the art spectrometers are in use in this field, e.g. in harvesting control and meat processing. Further applications may be addressed

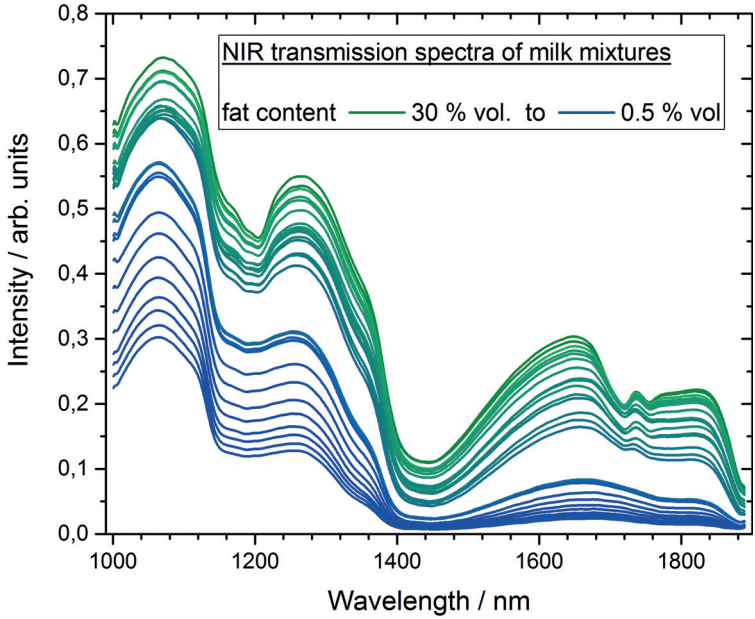

Figure 8.3: NIR spectra (acquired with scanning grating technology in diffuse reflectance mode) of milk mixtures with fat content in the range from 0.5–30 % vol.

with decreasing price and reasonable total cost of ownership. Besides, sterilization and cleaning in process must be taken into account.

Handheld analyzers – expert systems

A suitable system integration including light source, data interface and power management is required. Rough environmental conditions must be considered. Developments in this market area are already in progress.

Integrated devices – consumer use

Spectral analyzers may be integrated e.g. into scales at the point of sales or into kitchen equipment like mixers or refrigerators. A major issue beside the data base will be the proper measurement of the relevant data. Here user guidance for inhomogeneous objects combined with intelligent software may help for proper measurement quality.

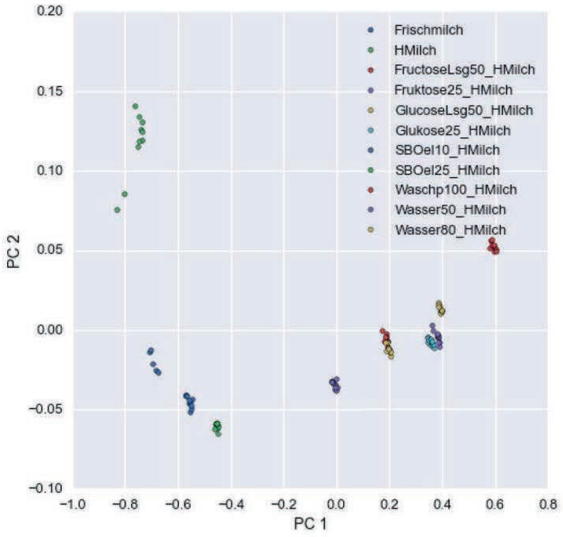

Figure 8.4: PCA of adulterated milk samples, FhG-report: MEF-SensoSpek 2015, in cooperation with H. Schulte (Fraunhofer IOSB).

Mobile spectrometers – everybody

An NIR spectral analyzer in a mobile phone or similar device may serve more applications than just food. Also here a dedicated software app must ensure proper use.

Concerning the food market optical NIR-spectroscopy has a huge potential as smart monitoring technology in the whole food value chain (see Fig. 8.4).

Certain requirements arise for appropriate NIR spectroscopy systems for a potential field of application within the food value chain, which are summarized in Tab. 8.2.

3.2 Opportunities for spectrometer development

Starting from existing systems and devices and based on multiple discussions with potential customers from different market segments, it can be derived that a growing market for NIR food analyzers exists.

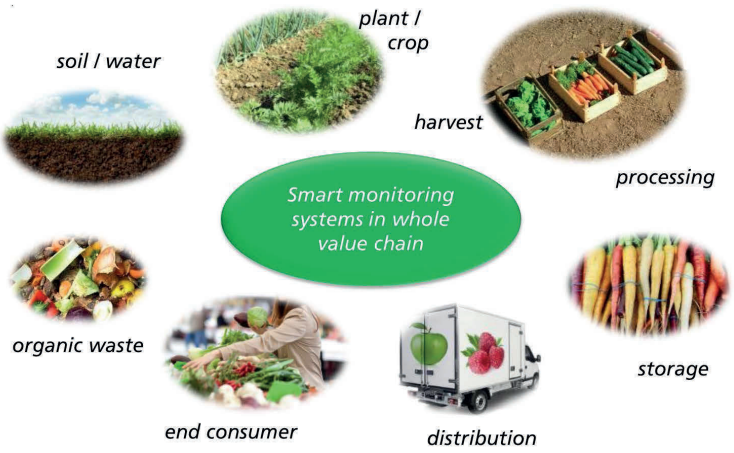

Figure 8.5: Food value chain and potential fields of application for optical NIR-spectroscopy as smart monitoring technology.

In-line monitoring is driven by increasing requirements due to legislative changes [11]. There is a growing demand to access food quality, e.g. freshness and ripeness of fruit, at the Point-of-Sales. Finally, several mobile phone manufactures and their optical system integrators have signaled interest in NIR spectroscopy but the cost requirements are tough to meet. Within the next years business opportunities arise for those who provide systems within an acceptable cost and price range.

3.3 Development goals in the field of MEMS based solutions

Based on feedback from the agricultural and mobile phone market first steps have been implemented for two new MEMS based approaches. The required specifications of below approaches are the result of discussions with agricultural machinery manufacturers and suppliers in the US and Europe.

a) The next generation MEMS spectrometer is aiming at the handheld market. The outer dimensions should not exceed 50 x 50 x 30 mm^3.

Table 8.2: Requirements for NIR spectroscopy within the food value chain.

Requirements for NIR system	Style	Size [cm³]	Sensitivity [a.u.]	Environmental conditions	Estimated Cost [€]
Field (soil, water, fertilizer, manure)	tractor mounted	9000	4.5-5.0	harsh (rough handling, vibration, temperature, dirt)	5000
Plant/crop	multiple (e.g. UAV)	75	3.5	light weight	100
Harvest	tractor mounted	800	4.0	harsh	500
Animal	handheld or wearable	75	3.5	corrosive, dirt	100
Processing	in-line	800	4.0	sterilization compatible	500
Storage	handheld or in-line	75	3.5	low temperature	500
Distribution	handheld and integrated (e.g. scales)	75	3.5	moderate	50
Consumer	mobile phone, refrigerator, kitchenware (e.g. mixer)	< 2	3.0	low cost	5

The target performance will be similar to the commercial available SGS 1900 system (, i.e. λ = 950 .. 1900 nm, 10 nm spectral resolution and 3.5 a.u. information depth) but with reduced outer dimensions.

b) An extremely miniaturized MEMS spectrometer for the potential use in mobile phones could have a very flat layout with 15 x 10 x 6 mm^3, possibly even slightly thinner. If necessary and affordable, the spectral range can be 1000–1900 nm with 10 nm resolution and at least 3 a.u. performance. However, reduced parameters will possibly be sufficient and less demanding.

3.4 Other options

Besides MEMS based spectrometers, there are other options for NIR spectral analysis. Diode array spectrometers with a fixed grating were the first step to miniaturization. Here, expensive detector materials, e.g. extended InGaAs, have limited the cost reduction. Assuming 10 nm spectral resolution and a minimum of 3 detector elements for this wavelength interval, the 900 – 1000 nm range corresponds to 256 or 512 ele-

Table 8.3: Requirements and development goals for different market tiers.

Market tier	Requirement / Development
High-end for harsh environment	Full 16 bit performance needed corresponding to 4.5 … 5 a.u., tough shock survival, size less critical Currently: diode array spectrometers (e.g. Zeiss Corona or Foss) Estimated cost reduction from 15-30 k€ to 1 k€ in 5-8 years
In-line process control device	14 bit performance corresponding to 4 a.u., Currently: either diode array spectrometer (see above & e.g. Avantes, OceanOptics) or MEMS based system (Hiperscan) Size reduction is preferred, but cost has to reach level below 500 € within the next 3-5 years
Handheld / integrated PoS System	12 bit performance, i.e. 3.5 a.u. Currently: for example "Phazir" handheld from Thermofisher Size target is below 75 cm^3, price target below 100 € in 3-5 years with estimated further decrease to 50 € region
Consumer	New development Price below 5 €, size smaller 2 cm^3, thickness requirement for mobile phone is below 6 mm Performance and time to market are to be defined Huge investments necessary in technology development, integration, …

ments in total. Today a typical width of 50 μm is used for each element to grant good SNR properties. This leads to a width of 12 – 25 mm of the sensitive area, which must be granted by the systems optical design. Lower requirements and performance may only demand 5 nm interval per pixel, 25 μm element width and 128 elements for 600 nm free spectral range. Thus the sensitive area could be shrunk to 3.2 mm. Still the question of prices for high volume production remains a challenge.

Cost may be reduced by applying single detector and a digital light processor (DLP). Although a DLP might be too large for mobile phone applications, the approach is suitable for handheld and in-line devices.

Interferometer based systems such as Fabry-Perot filters have been presented (e.g. Spectral Engines, Hamamatsu). These have a small form factor and reasonable price but still insufficient free spectral range and possibly limitations to vibration and shock in mobile and handheld systems. Filter based solutions with individual filters on each element of a detector array share the same cost issue like fixed grating spectrometers.

3.5 Recent developments

The scanning grating technology implemented at Fraunhofer IPMS is facing new developments heading for compact and ultra-small optical setups. The key to a cost efficient assembly is the alignment and reduction of the optical components cost. The actual hybrid mounted "stacked component" spectrometer SCS prototype requires complex off axis mirrors for the folded optical path. As of today, these mirrors have been fabricated by ultra-precision technologies from aluminum. Plastic or glass molding technologies do not meet the optical requirements today. Here, a joint development of optical layout and mirror technology might lead to a cost efficient way to build this device in high volume.

4 Summary and Outlook

Food safety and food quality are important topics for the individual consumer and to our society in general. Thus analytical methods for food analysis are of growing importance driven both by environmental and legislative requirements. In this context fast and non-invasive techniques are in favour. These requirements are fulfilled by optical methods. Vibrational spectroscopy is a strong tool for analysis of organic materials and especially near-infrared (NIR) spectroscopy is a suitable and promising candidate. It has been shown that miniaturized NIR spectrometers can be realized using MEMS technology. Several systems designs are presented and optimization required to match with size and cost requirements has been discussed. To reach deployment in challenging environmental conditions and in larger volume there is still development investment necessary. Ultimately, for a broad implementation of food analyzing systems mobile phones offer a very promising platform. However, the application software must display the relevant data in a way that is applicable for the non-scientific user. A joined effort of hardware, software and database providers may open the door for widespread usage of MEMS-based NIR food analyzers and will lead to new market opportunities.

References

1. F. Röck et al., "Electronic nose: Current status and future trends," in *p. 705-725*, Chem. Rev. 108 2008.
2. L. Escuder-Gilabert et al., "Review: Highlights in recent applications of electronic tongues in food analysis," in *pp. 15-25*, Analytica Chimica Acta 665 2010.
3. D.I. Ellis et al., "Point-and-shoot: rapid quantitative detection methods for on-site food fraud analysis – moving out of the laboratory and into the food supply chain," in *pp. 9401-9414*, Anal. Methods 7 2015.
4. Gram et al., "Food spoilage - interactions between food spoilage bacteria," in *pp. 79-97*, International Journal of Food Microbiology 78 2002.
5. European Commission, "Food safety overview: Biological safety." [Online]. Available: http://ec.europa.eu/food/safety/biosafety_en
6. ——, "Food safety overview: Chemical safety." [Online]. Available: http://ec.europa.eu/food/safety/chemical_safety/index_en.htm
7. B.M. Nicolaï et al., "Nondestructive measurement of fruit and vegetable quality by means of nir spectroscopy," in *pp. 99-118*, Postharvest Biology and Technology 46 2007.
8. A. Cifuentes, "Food analysis: Present, future, and foodomics," in *Article ID 801607*, doi:10.5402/2012/801607, ISRN Analytical Chemistry 2012.
9. Pügner et al., "Near-infrared grating spectrometer for mobile phone applications," in *pp. 734–745*, Applied Spectroscopy Vol. 70(5) 2016.
10. "Patent US8045159 B2, Optical apparatus of a stacked design, and method of producing same."
11. "Regulation (EU) No 1169/2011 of the European Parliament and of the council on the provision of food information to consumers," October 2011. [Online]. Available: http://eur-lex.europa.eu/legal-content/EN/TXT/HTML/?uri=CELEX:32011R1169&from=DE

Optical measurement of material abundances in mixtures incorporating preprocessing to mitigate spectral variability

Wolfgang Krippner, Sebastian Bauer and Fernando Puente León

Institute of Industrial Information Technology (IIIT),
Karlsruhe Institute of Technology (KIT),
Hertzstr. 16, 76187 Karlsruhe, Germany

Abstract A new optical approach for determining the abundances of substances in mixtures is presented. By using specifically designed spectral filters, it is sufficient to acquire monochrome images whose intensity quantitatively depicts the abundance of the respective material.

Keywords: Hyperspectral image, optical computing, optical measurement, spectral filtering.

1 Introduction

Hyperspectral images allow for the extraction of rich information about the considered scene. The downside of hyperspectral imaging, however, is the high cost for acquisition devices and the subsequent elaborate image processing hardware and software. In this paper, we investigate an alternative approach to spectral unmixing based on recorded images. Spectral unmixing denotes the process of extracting the material abundances in mixtures. Bypassing the need for acquisition, processing and information extraction, we use programmable spectral filters that allow for the acquisition of a single intensity image. When the spectral filter is chosen adequately, this image encodes the spatial abundance of the considered target spectrum. We present filter design methods that take the spectral variability of the target spectra into account.

2 Spectral filter design methods

The optical measurement of material abundances in mixtures uses specificially designed spectral filters. Their calculation is described in this section. Their implementation will be discussed in Section 4. Each of the following methods for the analytical design of spectral filters is based on the linear mixing model (LMM)

$$\mathbf{y}_{ij} = \sum_{k=1}^{p} a_{ijk}\,\mathbf{m}_k + \boldsymbol{\varepsilon}_{ij} = \hat{\mathbf{y}}_{ij} + \boldsymbol{\varepsilon}_{ij}\,, \tag{9.1}$$

where $\mathbf{y}_{ij}$ denotes the spectrum at pixel i, j of the hyperspectral image $\mathbf{Y} \in \mathbb{R}^{n_x \times n_y \times \Lambda}$ and $\mathbf{Y} \geq \mathbf{0}$, measured at Λ wavelengths. The spectra of the p pure materials assumed to be present in the observed scene are described by $\mathbf{m}_k$, whereas the a_{ijk} denote the corresponding abundances. To account for a physically meaningful representation, the abundances are commonly restricted by the constraints $\sum_{k=1}^{p} a_{ijk} = 1$ and $a_{ijk} \geq 0\ \forall i, j, k$. Both measurement noise and deviations from solely linear mixing are taken into account by $\boldsymbol{\varepsilon}_{ij}$.

The following methods for the design of spectral filters assume that the $\mathbf{m}_k$ are known, whereas $\mathbf{Y}$ is not recorded and, consequently, not available for any subsequent derivations. Particularly, for each material k, a collection of n spectra $\mathbf{m}_{kl}$ $(l = 1, \ldots, n)$ exists in addition to the corresponding mean spectrum $\mathbf{m}_k^{\star}$. The differences between the $\mathbf{m}_{kl}$ within the collection are mainly the result of chemical, microscopic and macroscale geometric effects. The so-called endmember variability [1] denotes this variability of pixel spectra of the same pure material and will be considered by an instability index [2, 3], which is used as a preprocessing step for the endmember collections in some of the next derivations of the spectral filters.

Following the LMM (9.1), the mathematical derivation of material abundances results in

$$a_{ijk} = \mathbf{f}_k^{\mathrm{T}}\mathbf{y}_{ij} = \sum_{k=1}^{p} a_{ijk}\,\mathbf{f}_k^{\mathrm{T}}\mathbf{m}_k\,, \tag{9.2}$$

where $\mathbf{f}_k$ denotes the spectral filter used to obtain the abundances of the pure material k assuming $\boldsymbol{\varepsilon}_{ij} = 0$. The determination of the abundances in (9.2) will be performed optically. It should be noted that

(9.2) obviously stipulates both $\mathbf{f}_k^{\mathrm{T}}\mathbf{m}_k = 1$ and $\mathbf{f}_k^{\mathrm{T}}\mathbf{m}_j = 0$ for $k \neq j$ and $j = 1, 2, \ldots, p$. However, not only $\boldsymbol{\varepsilon}_{ij} \neq 0$, but also the endmember variability substantially hamper that these conditions be exactly fulfilled.

As a general method for deriving $\mathbf{f}_k$, we consider the least-squares estimator. Using (9.1) and performing some further calculations, omitted for the sake of space, leads to

$$\mathbf{a}_{ij} = \begin{bmatrix} a_{ij1} \\ \vdots \\ a_{ijp} \end{bmatrix} = \begin{bmatrix} \mathbf{f}_1^{\mathrm{T}} \\ \vdots \\ \mathbf{f}_p^{\mathrm{T}} \end{bmatrix} \mathbf{y}_{ij} = \left(\mathbf{M}^{\mathrm{T}}\mathbf{M}\right)^{-1}\mathbf{M}^{\mathrm{T}}\mathbf{y}_{ij}\,, \tag{9.3}$$

where $\mathbf{M} = \left[\mathbf{m}_1, \ldots, \mathbf{m}_p\right]$ holds and $\left(\mathbf{M}^{\mathrm{T}}\mathbf{M}\right)^{-1}\mathbf{M}^{\mathrm{T}}$ is called the *Moore–Penrose pseudoinverse* of $\mathbf{M}$.

The design of spectral filters according to (9.3), where $\mathbf{M}$ is replaced by $\mathbf{M}^\star = \left[\mathbf{m}_1^\star, \ldots, \mathbf{m}_p^\star\right]$, describes the first method considered for the optical determination of material abundances. The spectral filters derived by this method are denoted as *pseudoinverse spectral filters* $\mathbf{f}_k^{\mathrm{PS}}$.
In contrast, the following methods first apply the spectral manipulation $\mathbf{C}\,\mathbf{y}_{ij} = \mathbf{C}\,\mathbf{M}\mathbf{a}_{ij}$, where $\mathbf{C} \in \mathbb{R}^{\Lambda\times\Lambda}$ denotes a non-orthogonal matrix. Then, the spectral filters are derived by

$$\tilde{\mathbf{a}}_{ij} = \begin{bmatrix} \tilde{a}_{ij1} \\ \vdots \\ \tilde{a}_{ijp} \end{bmatrix} = \begin{bmatrix} \tilde{\mathbf{f}}_1^{\mathrm{T}} \\ \vdots \\ \tilde{\mathbf{f}}_p^{\mathrm{T}} \end{bmatrix} \mathbf{y}_{ij} = \left((\mathbf{C}\mathbf{M})^{\mathrm{T}}\,\mathbf{C}\mathbf{M}\right)^{-1}(\mathbf{C}\mathbf{M})^{\mathrm{T}}\,\mathbf{C}\mathbf{y}_{ij} \tag{9.4}$$

denoting a similar approach as (9.3).

Searching for a meaningfully defined $\mathbf{C}$, [3] proposes to account for the shape of $\mathbf{m}_k$ in order to improve the estimates of the material abundances. Spectral differences $\Delta m_{ki} = m_{ki+1} - m_{ki}$ $(i = 1, \ldots, \Lambda - 1)$ leading to spectra $\Delta\mathbf{m}_k$ are calculated therefor. This can be performed by a suitably chosen $\mathbf{C}$. Applying the differences on material spectra tends to significantly increase the endmember variability. To mitigate this drawback, we smooth each spectrum beforehand by applying the discrete cosine transform [4] first and then removing coefficients representing high frequencies. Note that the discrete cosine transform is a linear transformation and, consequently, can be integrated into an

appropriate $\mathbf{C}$. The spectral filters, named *differential filters* $\boldsymbol{\Delta}\tilde{\mathbf{f}}_k$ in the following, finally result by using $\mathbf{C} = \mathbf{C}_{\text{diff}}{\mathbf{C}_{\text{dct}}}^{\text{T}}\mathbf{C}_{\text{sm}}\mathbf{C}_{\text{dct}}$, where $\mathbf{C}_{\text{dct}} \in \mathbb{R}^{\Lambda\times\Lambda}$ denotes the discrete cosine transform matrix. $\mathbf{C}_{\text{sm}} \in \mathbb{R}^{\Lambda\times\Lambda}$ denotes the identity matrix, where $c_{\text{sm},nn} = 0$ for $n = m, \ldots, \Lambda$ for the m highest frequencies that belong to sharp edges of $\mathbf{m}_k$ and therefore should be suppressed. The matrix $\mathbf{C}_{\text{diff}} \in \mathbb{R}^{\Lambda\times\Lambda}$ is used to derive $\Delta\mathbf{m}_k$, where $\Delta\mathbf{m}_k^\star$ denotes the differences of the mean spectra that are considered for $\boldsymbol{\Delta}\tilde{\mathbf{f}}_k$. $\mathbf{C}_{\text{diff}}$ consists of ones on the main diagonal and -1 on the first diagonal above the main diagonal.

The next methods for the derivation of the spectral filters extend $\mathbf{f}_k^{\text{PS}}$ and $\boldsymbol{\Delta}\tilde{\mathbf{f}}_k$ to incorporate the endmember variability contained within the collections of the pure materials. In detail, the endmember variability is valued by the instability index, abbreviated with ISI, and defined as

$$\text{ISI}_\lambda = \frac{\Delta_{\text{within }\lambda}}{\Delta_{\text{between }\lambda}} = \frac{P}{P-1}\sum_{k=1}^{P-1}\sum_{r=k+1}^{P}\frac{1.96\,(\sigma_{k\lambda}-\sigma_{r\lambda})}{\left|R_{\text{mean},k\lambda}-R_{\text{mean},r\lambda}\right|} \tag{9.5}$$

for each wavelength $\lambda = 1, \ldots, \Lambda$. In this equation, $R_{\text{mean},k\lambda}$ denotes the mean reflectance value of class k at wavelength λ and $\sigma_{k\lambda}$ the standard deviation of class k at the same wavelength.

The variability at wavelength λ within each collection of spectra referring to a certain material class is taken into account by $\Delta_{\text{within }\lambda}$, whereby the sum of the one-sided 95 % confidence interval is used under the assumption that each collection contains normally distributed spectra. Conversely, $\Delta_{\text{between }\lambda}$ accounts for the distances between the mean spectra of the pure materials k and r at wavelength λ, i.e., $m_{k\lambda}^\star$ and $m_{r\lambda}^\star$. Using (9.5) allows to assess the endmember variability at each wavelength. A large value of ISI_λ indicates a greater value of $\Delta_{\text{within }\lambda}$ than the value of $\Delta_{\text{between }\lambda}$. Wavelength λ should consequently be discarded for the design of the spectral filters.

To incorporate the ISI index into the filter design (9.4), we propose two different versions of the transformation matrix $\mathbf{C}$. The first one uses (9.5) for defining additional weightings for each wavelength by

$$\mathbf{C}_{\text{ISI}} = \begin{bmatrix} \text{ISI}_1^{-1} & 0 & \ldots & & 0 \\ 0 & \text{ISI}_2^{-1} & 0 & \ldots & 0 \\ \vdots & \ddots & \ddots & \ddots & \vdots \\ 0 & \ldots & & 0 & \text{ISI}_\Lambda^{-1} \end{bmatrix} \in \mathbb{R}^{\Lambda\times\Lambda}, \tag{9.6}$$

whereas the second one not only considers these weightings, but also completely removes wavelengths corresponding to high values of (9.5) by using $\mathbf{C}_{\mathrm{ISI,Thresh}} = \mathbf{C}_{\mathrm{Thresh}}\mathbf{C}_{\mathrm{ISI}}$. Here, $\mathbf{C}_{\mathrm{Thresh}} \in \mathbb{R}^{\Lambda\times\Lambda}$ denotes a unit matrix with $c_{\mathrm{Thresh},ii} = 0$ if $\mathrm{ISI}_\lambda > \tau$ holds. For the threshold τ we consider a multiple of the mean of the ISI, $\tau = c\,\mu_{\mathrm{ISI}}$ and $c > 0$.

Combining $\mathbf{C}_{\mathrm{ISI}}$ and $\mathbf{C}_{\mathrm{ISI,Thresh}}$ with $\mathbf{f}_k$ and $\Delta\tilde{\mathbf{f}}_k^{\mathrm{PS}}$ is achieved by setting $\mathbf{C} = \mathbf{C}_{\mathrm{ISI}}$, $\mathbf{C} = \mathbf{C}_{\mathrm{ISI,Thresh}}$ and $\mathbf{C} = \mathbf{C}_{\mathrm{ISI}}\mathbf{C}_{\mathrm{diff}}\mathbf{C}_{\mathrm{dct}}{}^{\mathrm{T}}\mathbf{C}_{\mathrm{sm}}\mathbf{C}_{\mathrm{dct}}$, $\mathbf{C} = \mathbf{C}_{\mathrm{ISI,Thresh}}\mathbf{C}_{\mathrm{diff}}\mathbf{C}_{\mathrm{dct}}{}^{\mathrm{T}}\mathbf{C}_{\mathrm{sm}}\mathbf{C}_{\mathrm{dct}}$, respectively, and yields the spectral filters denoted by $\tilde{\mathbf{f}}_k^{\mathrm{PS,ISI}}$, $\tilde{\mathbf{f}}_k^{\mathrm{ISI,Th}}$, $\Delta\tilde{\mathbf{f}}_k^{\mathrm{ISI}}$ and $\Delta\tilde{\mathbf{f}}_k^{\mathrm{ISI,Th}}$.

In total, 6 types of spectral filters have been presented. The following section shows our approach for their optical implementation, whereas in Section 4, each of them is applied experimentally to evaluate its performance in estimating material abundances.

3 Optical implementation of spectral filters

In order to realize the spectral filters derived in the previous section, we customize the measuring system which is normally used to record common hyperspectral images. The following measuring approach results in an innovative procedure for deriving material abundances in mixtures.

Hyperspectral images are obtained by first discretizing the considered wavelength range into a finite number of wavelength channels. The scalar images, which finally form a hyperspectral image by arranging them to a stack, are then measured with a constant exposure time in each wavelength channel. Thus, each wavelength is weighted equally. Conversely, to optically realize the designed spectral filters, we adjust the exposure time of each wavelength channel with respect to the spectral filter coefficients. Large values in the magnitudes of the coefficients result in higher exposure times and vice versa. Eventually, the grayscale intensity images only have to be summed up in order to obtain spatial estimates for the material abundances. Note that keeping the camera shutter open during the complete measuring time even supersedes the need for recording numerous grayscale images and summing them up, and directly yields the intensity image showing the material abundances. Because of hardware restrictions,

this advanced exposure technique has not been investigated experimentally yet, though.

Since negative values of spectral filter coefficients may occur, whereas physically meaningful exposure times are restricted to positive values, the spectral filters have to be split into a positive and a negative part, $\mathbf{f}_k = \mathbf{f}_k^+ + \mathbf{f}_k^-$, where $f_{k\lambda}^+ \geq 0$ and $f_{k\lambda}^- < 0$ hold for $\lambda = 1, 2, \ldots, \Lambda$. Hence, instead of $\mathbf{f}_k$, two grayscale images are recorded that represent the optical realization of $\mathbf{f}_k^+$ and $\mathbf{f}_k^-$. As mandatory postprocessing step, they have to be subtracted.

4 Experimental evaluation

For the evaluation of the optical determination of material abundances in mixtures we used an experimental setup consisting of a 300 W Xenon lamp as the light source, an EMCCD camera (Andor iXon$_3$897) and a spectral filter, namely an acousto-optical tunable filter (AOTF, Gooch&Housego HSi-300), which allows to tune the mean wavelength and bandwidth of each wavelength channel. The following evaluations consider the wavelength range between 450 and 810 nm, in which the sampling is accomplished in steps of 4 nm resulting in 91 wavelength channels.

As samples we examine mixtures of color powders and mixtures created by a laser printer with reference to an artificially derived image. The additional investigation of the second mixture scheme results from former examinations, which exhibit significant violations of the LMM by mixtures of color powders. In contrast, the printed mixtures approximate the LMM sufficiently well due to the fact that they were designed aiming for meeting assumptions belonging to the LMM, such as that spectral mixing occurs only on the macroscopic scale [5]. The determination of the material abundances with the printed mixtures remains challenging because the number of raw materials is increased by a fifth color.

Since in each mixture regions including a single material are present, spectra of the corresponding pixels are used to build the collections of spectra of pure materials. The mean spectra and variances are shown in Figures 9.1 and 9.2. Note that the spectrum of color 5 exhibits a remarkable similarity to the spectrum of color 2, whereas the pure spec-

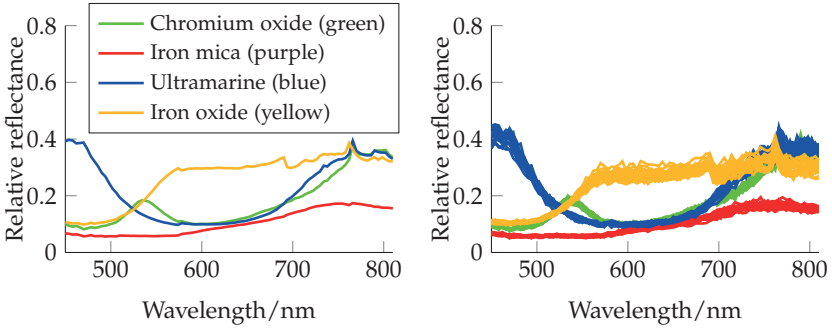

Figure 9.1: Powder mixtures: mean spectra (left), 20 pixel samples of pure spectra as an excerpt of the used collections (right).

tra within the mixture of the color powders are visually more distinguishable. The variances demonstrate notable endmember variability throughout the considered wavelength range. Using the information about ultramarine, Figure 9.3 illustrates the normalized (i.e., the maximum value is normalized to 1) spectral filters following from Section 2. Though the spectral filters aim for estimating the abundances of the same material, their shapes vary substantially.

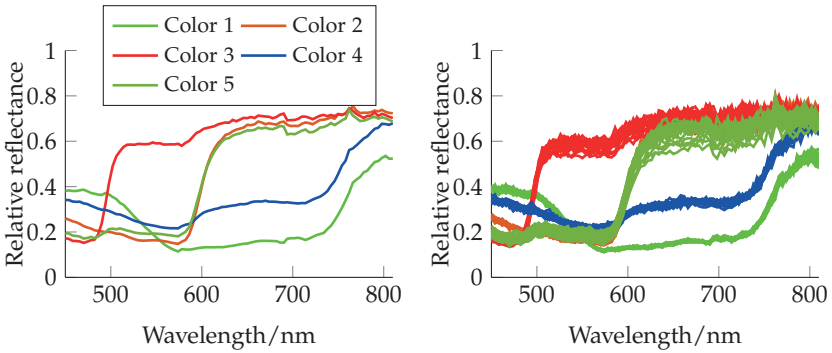

Figure 9.2: Printed mixtures: mean spectra (left), 20 pixel samples of pure spectra as an excerpt of the used collections (right).

The assessment of the spectral filters' performance in accurately estimating material abundances is conducted using the root mean square error $e_\theta = \frac{1}{n_x n_y}\sqrt{\sum_{i=1}^{n_x}\sum_{j=1}^{n_y}\theta_{ij}^2}$ where θ_{ij} denotes the angle between the estimated abundances $\hat{\mathbf{a}}_{ij}$ and the true abundances $\mathbf{a}_{ij}$ (ground truth) at pixel i, j, calculated by $\theta_{ij} = \hat{\mathbf{a}}_{ij}^{\mathrm{T}}\mathbf{a}_{ij}/\|\hat{\mathbf{a}}_{ij}\|\|\mathbf{a}_{ij}\|$. The root mean square error is invariant to the normalization of $\hat{\mathbf{a}}_{ij}$ [6] and therefore provides qualitative results. It will be used to evaluate both the optically determined abundances and the abundances derived by mathematically applying the spectral filters on recorded full hyperspectral images of the mixtures.

Tables 9.1 and 9.2 show the results of e_θ for both mixing schemes. In addition, the intensity images following from the use of the spectral filters for ultramarine and color 3, as illustrative examples, are presented in Figure 9.4. The evaluation exhibits slight differences of e_θ with respect to the application of different spectral filters for the determination of material abundances.

Figure 9.4 allows the implication that the optical use of spectral filters based on shapes of the pure spectra leads to the largest deviations comparing with the derived results. Probably, the differences depend on the shape of the spectral filters. As a consequence, efforts for more detailed investigations focusing on the capability of the optical implementation of different types of shapes of spectral filters including comparisons with derived results, should be taken in future work.

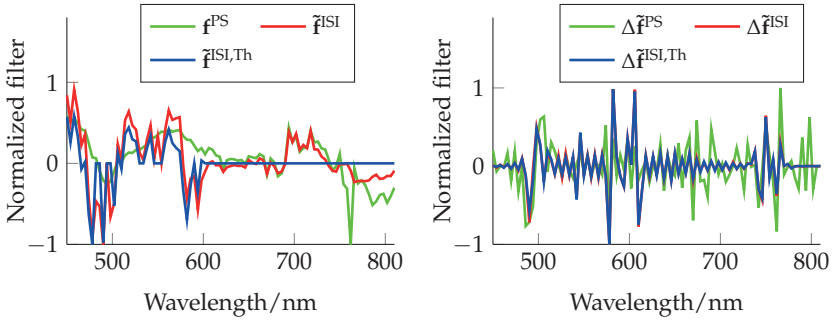

Figure 9.3: Ultramarine: spectral filters using the original spectra (left) and their differences (right).

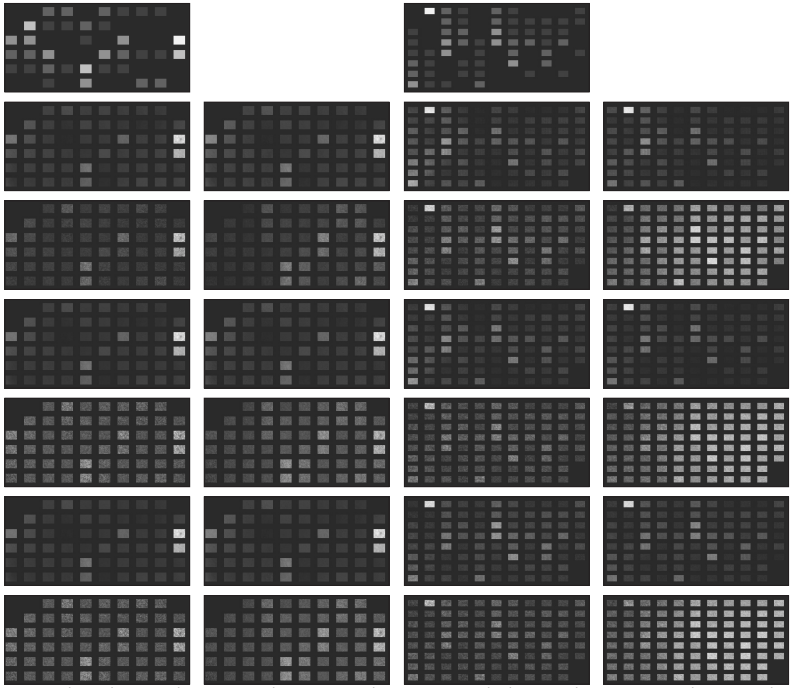

Figure 9.4: The two left columns show the ultramarine abundances, while the two right columns show the abundances of color 3. Top row: ground truth, second row: pure pseudoinverse ($\mathbf{f}_k^{\mathrm{PS}}$), third row: differences ($\Delta\tilde{\mathbf{f}}_k$), fourth row: ISI index ($\tilde{\mathbf{f}}_k^{\mathrm{PS,ISI}}$), fifth row: ISI index with differences $\Delta\tilde{\mathbf{f}}_k^{\mathrm{ISI}}$, sixth row: ISI index with threshold ($\tilde{\mathbf{f}}_k^{\mathrm{ISI,Th}}$), last row: ISI index with threshold and differences ($\Delta\tilde{\mathbf{f}}_k^{\mathrm{ISI,Th}}$).

5 Summary

The use of spectral filters for directly acquiring abundances in mixtures using grayscale images has been shown both theoretically and experimentally. Various filter design methods demonstrating some of the possibilities for incorporating additional information have been de-

Table 9.1: Powder mixtures: root mean square error.

	$\mathbf{f}^{\mathrm{PS}}$	$\Delta\tilde{\mathbf{f}}$	$\tilde{\mathbf{f}}^{\mathrm{ISI}}$	$\Delta\tilde{\mathbf{f}}^{\mathrm{ISI}}$	$\tilde{\mathbf{f}}^{\mathrm{ISI,Th}}$	$\Delta\tilde{\mathbf{f}}^{\mathrm{ISI,Th}}$
e_θ optical	0.0001	0.0020	0.0001	0.0023	0.0001	0.0023
e_θ derived	0.0011	0.0010	0.0011	0.0013	0.0011	0.0013

Table 9.2: Printed mixtures: root mean square error.

	$\mathbf{f}^{\mathrm{PS}}$	$\Delta\tilde{\mathbf{f}}$	$\tilde{\mathbf{f}}^{\mathrm{ISI}}$	$\Delta\tilde{\mathbf{f}}^{\mathrm{ISI}}$	$\tilde{\mathbf{f}}^{\mathrm{ISI,Th}}$	$\Delta\tilde{\mathbf{f}}^{\mathrm{ISI,Th}}$
e_θ optical	0.0017	0.0013	0.0016	0.0015	0.0012	0.0015
e_θ derived	0.0013	0.0010	0.0011	0.0013	0.0001	0.0013

scribed, e.g., the ISI index has been used that evaluates endmember variability. Although the results point into the right direction, filter design improvements have to be achieved in future. One possibility would be to include the conditions that the abundances of each pixel should be nonnegative and sum to one.

References

1. B. Somers, G. P. Asner, L. Tits, and P. Coppin, "Endmember variability in spectral mixture analysis: A review," *Remote Sensing of Environment*, vol. 115, no. 7, pp. 1603 – 1616, April 2011.
2. B. Somers, M. Zortea, A. Plaza, and G. P. Asner, "Automated extraction of image-based endmember bundles for improved spectral unmixing," *IEEE Journal of Selected Topics in Applied Earth Observations and Remote Sensing*, vol. 5, no. 2, pp. 396–408, April 2012.
3. B. Somers, S. Delalieux, W. W. Verstraeten, J. A. N. van Aardt, G. L. Albrigo, and P. Coppin, "An automated waveband selection technique for optimized hyperspectral mixture analysis," *International Journal of Remote Sensing*, vol. 31, no. 20, pp. 5549–5568, October 2010.
4. N. Ahmed, T. Natarajan, and K. R. Rao, "Discrete cosine transform," *IEEE Transactions on Computers*, vol. C-23, no. 1, pp. 90–93, Jan 1974.
5. N. Keshava and J. F. Mustard, "Spectral unmixing," *IEEE Signal Processing Magazine*, vol. 19, no. 1, pp. 44–57, Jan 2002.
6. J. M. P. Nascimento and J. M. B. Dias, "Vertex component analysis: a fast algorithm to unmix hyperspectral data," *IEEE Transactions on Geoscience and Remote Sensing*, vol. 43, no. 4, pp. 898–910, April 2005.

Automatic fused tungsten carbide detection in weld pool

Maik Rosenberger[1], Chen Zhang[1], Karsten Günther[2], Jean Pierre Bergmann[2], Gunther Notni[1]

[1] Technische Universität Ilmenau, Department of Quality Assurance and Industrial Image Processing, Gustav-Kirchhoff-Platz 2, 98693 Ilmenau
[2] Technische Universität Ilmenau, Department of Production Technology, Gustav-Kirchhoff-Platz 2, 98693 Ilmenau

Abstract This paper represents an image-based tool for quantitative characterization of the dissolution behaviour of fused tungsten carbides (FTC) in weld pool. For the metallographical investigations with microscopic images, a method for automatic detection of hard phases is proposed to quantify the amount and distribution of FTCs in the matrix material. With this tool, the dependence of the hard phase characteristic on the welding parameters was investigated.

Keywords: metallography, welding process, image segmentation.

1 Introduction and motivation

In order to increase the wear resistance of tools underlying severe abrasive stresses (e.g. mining and oil drilling industry), fused tungsten carbides (FTC) embedded in a ductile Ni-base alloy become more and more important as hardfacing material. FTCs comprise an eutectoid morphology of mono-tungsten carbide (WC) and di-tungsten carbide (W_2C), whereby high cooling rates during the manufacturing process are necessary in order to stabilise both phases below 1300°C [1]. The benefit is a combination of high hardness and fracture toughness, exceeding the tribological properties of other commercial available hard phases [2].

Due to the manufacturing process, the weldability of FTC poses a challenge, as these hard phases have a strong liability to thermally induced dissolution reducing the wear performance of the hardfacing alloy [1,3–5]. In this context, the main reasons for the FTC degradation were not completely understood yet, so that several hypotheses currently exist referring to the high weld pool temperatures and dilution rates of the weld. Indeed, a deep understanding of the mechanisms is necessary in order to improve both welding process properties and hardfacing alloys [6–9].

In order to quantify the dissolution behaviour of FTC in dependence on the welding parameters, a software was developed, enabling a reliable detection of the hard phases in the cross section of the weld and thus giving a statement about the relation between the welding process parameters (welding feed speed, welding voltage and welding speed) and the content of the hard phases.

2 Experimental procedure

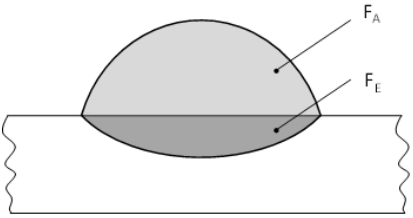

Dilution Rate A [%]

$$A = \frac{F_E}{F_E + F_A} * 100$$

Figure 10.1: Definition of the dilution rate.

For metallographical investigations, three cross sections per sample were extracted at a weld seam length of 40, 50, 60 mm and finally grinded as well as polished in a multi-staged procedure. Macroscopically, the dilution rate A is of main interest, as defined in figure 10.1. The metallographically obtained contrast facilitated the detection of the hard phases by means of the developed program and hence a calculation of the percentage amount with respect to the weld surface (F_E+F_A).

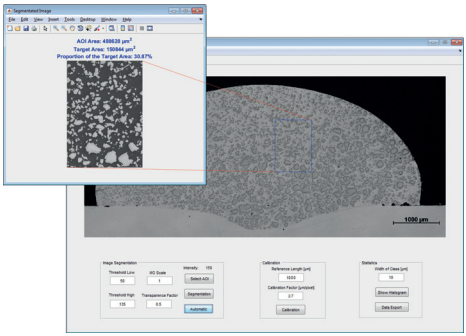

Figure 10.2: Detection of fused tungsten carbide (FTC) in the cross section of a hardfacing layer.

Through the calibration via the scale on the microscopic image, the calculated image resolution is 2.7 µm / pixel. The detection of the dark contrasted hard phases can be realized by adjusting the lower and upper threshold and thus localizing the relevant brightness intensity, see figure 10.2. Moreover, an algorithm for automatic hard phase detection is developed and will be extensively described in section 3.
Furthermore, the size distribution of the hard phases can be represented as histogram with user-defined class width, as shown in figure 10.3. The histogram offers another method for the characterisation of the microstructure of hard phases.

3 Automatic detection of hard phases

3.1 Evaluation of single methods

The hard phases are detected using image segmentation method. Generally, unsupervised methods for image segmentation could be divided into three classes: threshold-based, edge-based and region-based segmentation. In the first class, a set of threshold values is used to label different image regions and thus identifiy the target areas. A classical method for the automation of threshold selection is the Ostu's method [10], in which the optimal thresholds are determined by minimizing the within-class variance. The edge-based methods extract at first the outer contour of objects using different edge detectors [11].

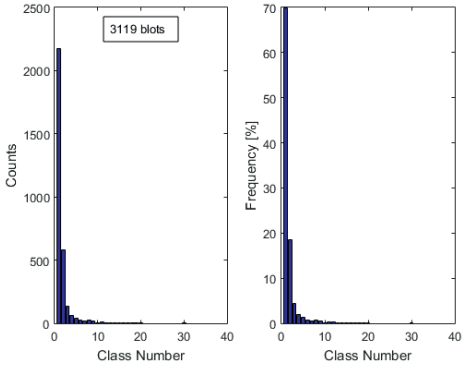

Figure 10.3: Histogram of hard phase sizes.

A considerable operator is the Canny detector for its ability in noise reduction and edge localization. Then, the small disconnectivities in the edges labeled by edge detectors must be eliminated so that closed region boundaries could be formed and identified as object regions. In the class of region-based methods, the active contour method is widely used. Starting from a set of initial object points, the neighboring pixels that satisfy a decision criterion are gradually added to the growing object region. As criterion, there is the region-based energy model [12] and the edge-based model [13]. The key step in the active contour method is a suitable selection of initial points to present the object property.

Besides these unsupervised methods, learning-based methods could be also used for image segmentation using support-vector-machine [14] or neural network [15]. But these methods need a high time expenditure for the collecting and labeling of training data. Therefore, only the unsupervised methods are taken into consideration within the framework of this work.

The challenge in the automation of hard phase detection is that the hard phases feature only a weak intensity contrast and the edge transition is irregular in part. With test images in grayscale, the Otsu's method, the Canny edge detector and the active contour method are individually evaluated first of all. With the fact that the central areas of hard phase, the edge transition areas and the background build

approximately three classes, the Ostu's method is implemented with three levels. Furthermore, the resulting hard phase map is used as initial mask in the active contour method, in which the region-based energy model is used in order to overcome the irregularity of edge transition behavior.

To oppress the small-scale noise textures in background which could lead to false connections of separate hard phases, the Canny edge detector is implemented with increasing σ values and the resulting edge maps are pixelwise summed to generate an integral map. It is assumed that pixels with high integral indices refer to true edges, because the peak locations of small-scale edges become unreliable or disapperare with large σ values [16]. Then, the small fractures in the contours are removed with morphological bridge operator, and the hard phase areas are identified with hole filling operation.

From the results in figure 10.4, it can be seen that the Otsu's method can only achieve a coarse segmentation with much noise and plenty of false connections between large particle areas, probably due to the inhomogeneity of intensity distribution. In contrast, the Canny detector based method can realize a clean seperation of different particle areas, but some large particles are missed, because there are significant weak points on their contours that are not identified by the edge detector, so that closed boundaries cannot be builded at these areas.

Using the hard phase map obtained with the Otsu's method as initial mask, the active contour method achieves an improved segmentation result, as shown in figure 10.4 c. However, there remain still some noise and false connectivities. Therefore, an improved initial mask with less noise and false connectivites is needed to achieve a better segmentation result.

In section 3.2, a hybrid method will be described, which combines the aforementioned single methods into a complex procedure and could achieve an improved performance.

3.2 Proposed hybrid method

Figure 10.5 illustrates the proposed method that is based on the active contour method for the detection of hard phases. For the performance enhancement of the active contour method, the initial mask that is obtained with the Ostu's threshold is processed with erosion and opening

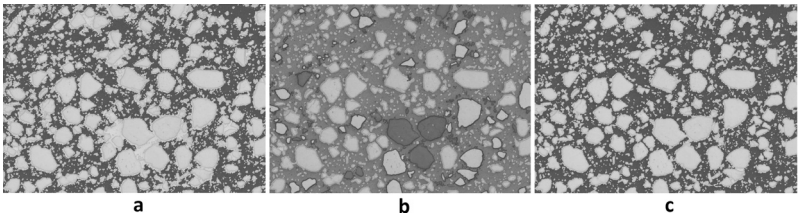

Figure 10.4: Hard phase detection based on different single methods. a: Otsu's threshold. b: Canny edge detector. c: active contour.

operation in order to disconnect independent hard phase areas clearly. But as a result, some small hard phase areas could disappear after these morphological operations. Therefore, the segmentation result with the active contour method is then merged with the hard phase map obtained with the Canny detector based method described in section 3.1, so that hard phases in all sizes can be accurately and cleanly extracted.

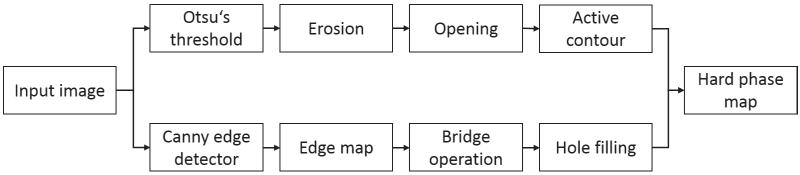

Figure 10.5: Proposed method for hard phase detection.

Figure 10.6 shows the segmented hard phase map with the proposed method. It is obvious that the boundaries of hard phase areas are extracted with high accuracy, and false connectivities can be avoided in principle.

4 Results and future work

Representative cross sections, see figure 10.7, illustrate the influence of the process parameters on the amount and distribution of FTCs in the Ni-base matrix material. It can be noticed, that an increase of the wire feed speed v_{GMAW} and welding voltage U_{GMAW} is going along

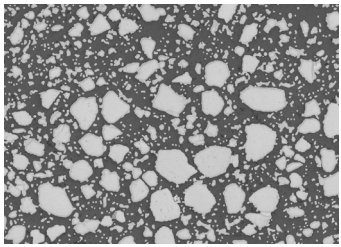

Figure 10.6: Detected hard phases with the proposed method.

with a rising dilution rate and a decrease of the hard phase content in the weld. However, metallographic investigations give only a qualitative statement concerning the relation between process parameters and microstructure.

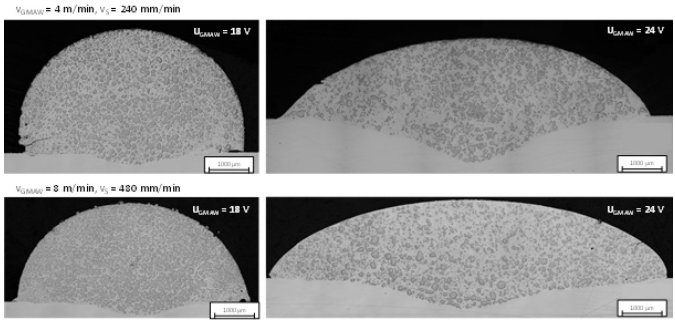

Figure 10.7: Influence of process parameters on the dilution and the hard phase characteristic.

Taking all investigated process parameters into account, the detection of the hard phase content finally evinced a dependency on the dilution rate, as depicted in figure 10.8. Maximum contents of app. 40 % at a dilution rate below 5 % could only be realized in between a narrow process window, including low wire feed speeds (v_{GMAW} = 4 m/min) and welding voltages U_{GMAW} (U_{GMAW} = 18 to 20 V). In return, a rising dilution rate of up to app. 40 % is synonymous with an almost complete extinction of FTC in the matrix.

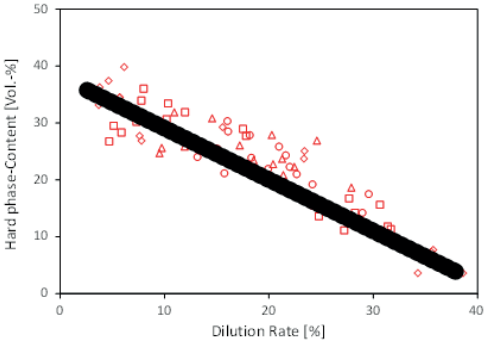

Figure 10.8: Relation between the hard phase content and the dilution rate.

Hence, by means of the developed software tool it could be proofed quantifiably, that the FTC dissolution shows a systematic dependency on the dilution to the substrate material (dilution rate), see figure 10.8. In contrast to the metallographic analysis, as shown in figure 10.7, this finding enables a specific adjustment of the welding process improving the wear performance of Ni-FTC hardfacings.

In the future, investigations based on histogram of hard phase size will be also performed to characterise the influences of welding parameters on the size distribution of hard phases.

References

1. F. Schreiber, *Wolfram-Schmelzkarbid im Verschleißschutz: Besonderheiten bei der schweißtechnischen Verarbeitung und Qualitätsicherung*. Fachartikel der Durum Verschleißschutz GmbH, 2000.
2. H. Berns, *Hartlegierungen und Hartverbundwerkstoffe*. Springer, 1998.
3. V. Z. Kublii and T. Y. Velikanova, "Ordering in the carbide W_2C and phase equilibria in the tungsten-carbon system in the region of its existence," in *Powder Metallurgy and Metal Ceramics*, vol. 43, pp. 630–644.
4. A. S. Kurlov and A. I. Gusev, "Tungsten carbides and W-C phase diagram," in *Inorganic Materials*, vol. 42, pp. 121–127.
5. R. Reiter, F. Schreiber, and K. Wernicke, "Verschleißeigenschaften von

Wolframkarbid-Hartlegierungen," in *Tagungsband zum 7. Werkstofftechnischen Kolloquium*, Chemnitz, Germany, 2004.

6. P. Vespa, P. T. Pinard, R. Gauvin, and M. Brochu, "Analysis of WC/Ni-based coatings deposited by controlled short-circuit MIG welding," in *Journal of Materials Engineering and Performance*, vol. 21, pp. 865–876.
7. E. Badisch and M. Kirchgassner, "Influence of welding parameters on microstructure and wear behaviour of a typical NiCrBSi hardfacing alloy reinforced with tungsten carbide," in *Surface and Coating Technology*, vol. 202, pp. 6016–6022.
8. L. Choi, M. Wolfe, M. Yarmurch, and A. Gerlich, "Effect of welding parameters on tungsten carbide-metal matrix composites produced by GMAW," in *Proceedings of Canadian Welding Association Conference*, Alberta, Canada, 2011.
9. L. J. Li and C. B. Gui, "Effect of dissolving of WC/W_2C on the interface microstructure of iron matrix hardfacing alloys," in *Advanced Materials Research*, vol. 306-307, 2011, p. 819–822.
10. N. Otsu, "A threshold selection method from gray-level histograms," in *Transactions on Systems, Man, and Cybernetics*, vol. 9, 1979, pp. 62–66.
11. D. Zhou and S. Tabbone, "Edge detection techniques: An overview," in *International Journal of Pattern Recognition and Image Analysis*, vol. 8, 1998, pp. 537–559.
12. V. Caselles, R. Kimmel, and G. Sapiro, "Geodesic active contours," in *International Journal of Computer Vision*, vol. 22, 1997, pp. 61–79.
13. T. F. Chan and L. A. Vese, "Active contours without edges," in *IEEE Transactions on Image Processing*, vol. 10, 2001, pp. 266–277.
14. J. Lu, D. Wang, L. Shi, and P. A. Heng, "Automatic liver segmentation in CT images based on support vector machine," in *Proceedings of theIEEE-EMBS International Conference on Biomedical and Health Informatics*, 2012, pp. 333–336.
15. M. Oquab, L. Bottou, I. Laptev, and J. Sivic, "Is object localizationfor free? -Weakly-supervised learning with convolutional neural networks," in *Proceedings of the IEEE Conference on Computer Vision and Pattern Recognition*, 2015, pp. 685–694.
16. X. Ren, "Multi-scale improves boundary detection in natural images," in *Proceedings of European Conference on Computer Vision 2008*, Marseille, France, 2008.

Improving material characterization in sensor-based sorting by utilizing motion information

Georg Maier[1], Florian Pfaff[2], Florian Becker[1], Christoph Pieper[3], Robin Gruna[1], Benjamin Noack[2], Harald Kruggel-Emden[3], Thomas Längle[1], Uwe D. Hanebeck[2], Siegmar Wirtz[3], Viktor Scherer[3] and Jürgen Beyerer[1]

[1] Fraunhofer Institute of Optronics, System Technologies and Image Exploitation IOSB
Fraunhoferstr. 1, 76131 Karlsruhe, Germany
[2] Karlsruhe Institute of Technology,
Intelligent Sensor-Actuator-Systems Laboratory
Adenauerring 2, 76131 Karlsruhe, Germany
[3] Ruhr-Universität Bochum, Department of Energy Plant Technology
Universitätsstraße 150, 44780 Bochum, Germany

Abstract Sensor-based sorting provides state-of-the-art solutions for sorting of cohesive, granular materials. Systems are tailored to a task at hand, for instance by means of sensors and implementation of data analysis. Conventional systems utilize scanning sensors which do not allow for extraction of motion-related information of objects contained in a material feed. Recently, usage of area-scan cameras to overcome this disadvantage has been proposed. Multitarget tracking can then be used in order to accurately estimate the point in time and position at which any object will reach the separation stage. In this paper, utilizing motion information of objects which can be retrieved from multitarget tracking for the purpose of classification is proposed. Results show that corresponding features can significantly increase classification performance and eventually decrease the detection error of a sorting system.

Keywords: Optical inspection, sensor-based sorting, multitarget tracking, classification.

1 Introduction

Sensor-based sorting technology enables the separation of a material feed into different classes. Typically, systems are used to remove low-quality or potentially dangerous entities from a feed. Applications are found in food processing [1], waste management [2], as well as sorting of industrial minerals [3]. The sorting process is commonly subdivided into the stages feeding, presentation, data analysis, and physical separation. Systems further differ in regard to the applied transport mechanism, sensors, and separation mechanism. A widespread setup regarding these components consists of a conveyor belt, line-scan cameras operating in the visible spectrum, and compressed air nozzles. Whenever an object is to be removed from the feed, it is deflected during a flight phase by activating corresponding nozzles. Hence, errors in sorting occur whenever an object to be accepted is falsely deflected and contrariwise. Which of these two errors is of higher importance depends on the sorting task at hand. However, both result from various errors that may occur, such as sensor errors, detection errors, or errors in physical separation.

For conventional systems utilizing scanning sensors, it is desired to achieve perfect flow control, i.e. the material moves with a defined, constant velocity. This is due to a delay between presentation and physical separation. Between these two points in time, no further information about an object can be obtained. Therefore, all objects are required to reach an expected velocity in order to be able to reliably predict the point in time as well as the position when the particles reach the array of air nozzles and hence minimize the error in physical separation. For certain products, this is a very hard task. In order to be able to also sort products for which perfect flow control is infeasible to achieve, replacing line-scan sensors by area-scan sensors has recently been proposed [4]. A sufficiently high frame-rate provided, objects can be observed at multiple points in time. By applying multi-target tracking, the velocity of the object can be determined. This way imperfection in flow control can be compensated and potential errors in physical separation can be reduced.

In this paper, it is demonstrated that information derived from tracking of the objects can also increase detection performance. More precisely, integral features such as the velocity are derived from the tracks.

These features can then be used to characterize objects contained in the feed. Therefore, classification can be performed on the basis of physical motion behavior and hence non-optical properties. To our best knowledge, this is the first time such an approach has been proposed for sensor-based sorting. Results show the approach can significantly increase classification performance for certain products.

2 Related work

Sensor-based sorting is a field of growing importance with widespread applicability. Corresponding systems can be used stand-alone, e.g. to clean a feed from impurities, or as a step of more complex sorting processes [2]. In many cases, systems are tailored to a specific task at hand and hence exploit knowledge about the material to be processed. This includes the selection of appropriate sensors [5] and possibly illumination [6]. State of the art systems employ scanning sensors such as line-scan cameras. Consequently, the material is required to be in motion, which is achieved by a corresponding transport mechanism. For instance, systems include a conveyor belt or the material is running down a slide or chutes. Derivation of the sorting decision, which typically can be regarded as an *accept or reject* task, is performed via data analysis. For cohesive, granular materials, arrays of compressed air nozzles are used for the task of physical separation. In optical sorting, sensor data can be interpreted as an image, hence image processing is performed. This includes segmentation of the image data, detecting regions containing objects, and classification of those [7]. For the latter, color related properties are often used [8].

Recently, replacing line-scan sensors by area-scan sensors has been proposed [9]. By obtaining sensor data for multiple points in time for each object contained in the feed, multitarget tracking can be utilized to gain insight into the trajectory of an object [4]. This eventually allows decreasing the error in physical separation since more accurate assumptions regarding the point in time as well as the position when an object reaches the separation stage can be employed. This paper extends these works by also utilizing motion information for the discrimination of objects.

3 Motion-based discrimination of products

The proposed approach aims at increasing detection performance by incorporating motion-related characteristics of individual objects of the feed. In the following, the methodology for deriving such features as well as the evaluation setup considered in this paper are presented.

3.1 Methods

In sensor-based sorting, the main direction in which objects are moving is defined by the system setup. For instance, using a conveyor belt, objects mainly move with the running direction of the belt. In order to obtain data that can be used for characterisation of objects based on their movement, it is required that each individual object is observed by the camera multiple times. Considering an area-scan sensor, this can be achieved by a sufficiently high frame rate.

From the image data, the position of objects, e.g. the centroid of the 2D projection, can be determined. This results in a set of points for each obtained frame. By applying multitarget tracking, information about the same object in successive frames can be combined into a track. Briefly, a standard Kalman filter is used for state estimation including the 2D position as well as velocity for both direction components as state variables. Also, an algorithm solving the Linear Assignment Problem is used for the association between retrieved measurements and existing tracks. A detailed description of the system is provided in [4,9]. Eventually, the path of each individual object can hence be described by a list of centroid measurements. However, these may vary in length due to different number of observation time points for the objects.

In the course of this work, basic motion-related key figures based on velocity and acceleration are manually selected. With respect to velocity, one temporally global as well as several temporally local features are considered. In this context, a global feature refers to information obtained for the entire observation sequence of an object. Local features are based upon 2 successive measurements for velocity related features and 3 for acceleration related features. The final feature vector is of dimensionality 14 and is a composite of the following numerical values:

- The number of measurements obtained.
- The global velocity of the object.
- The local minimal, average, and maximum velocity individually for the x and y component.
- The local minimal, average, and maximum acceleration individually for the x and y component.

It should be noted that local features, which are in the majority, can be computed in-line to the observations, while global features require identifying that an object left the observable area.

3.2 Evaluation framework

The described approach was validated experimentally. For this purpose, 4 products were identified for which similar, yet not equal motion characteristics may be expected. An illustration of the products is provided in Figure 11.1 (l.t.r): wooden hemispheres, wooden spheres, wax beads, and cotton balls. All objects have a diameter of 10 mm and only differ in terms of surface friction and weight. In addition to the different materials, the wax beads and cotton balls have a tiny hole through them.

(a) Wooden hemispheres, ∼0.26 g (b) Wooden spheres, ∼0.4 g (c) Wax beads with hole, ∼0.47 g (d) Cotton balls with hole, ∼0.24 g

Figure 11.1: Products used for experiments.

For these products, image data using a miniature optical belt sorter was recorded. A detailed presentation of the system with the purpose of a simulation thereof is provided in [10]. The objects were fed into the system by a vibrating feeder, passing down a slide on to a conveyor belt running at 1.1 m/s. Frames were recorded at ∼192 Hz using a camera of the type *Bonito CL-400*. An example frame is provided in Figure 11.2.

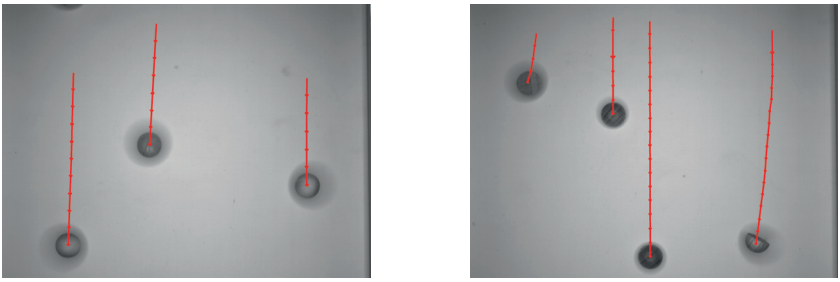

(a) Wooden spheres (b) Wooden hemispheres

Figure 11.2: Frames captured on the conveyor belt. The red, arrowed lines illustrate the resulting tracks in terms of associated measurements.

The conveyor belt has a total length of 60 cm. A crucial parameter for flow control is the length of the belt. Therefore, different lengths were imitated by mounting the camera at different positions along the belt at a fixed distance. More precisely, data was collected for 3 locations which are described in the following. The first section, hereafter referred to as *feeding*, is located right after objects enter the belt from the slide and covers the first $\sim$11 cm. Hence, this location simulates the shortest belt considered in this evaluation. The second section is located at the middle of the belt, covering the area reaching from $\sim$23 cm to $\sim$34 cm, and is referred to as *center* in the remainder. Lastly, the third section called *edge* covers the last $\sim$8 cm of the belt.

Each of the following processing steps were performed offline subsequent to image recording. First, basic image processing routines are required to extract the midpoints of potentially contained objects in each frame. For this purpose, the fact that a stable background as well as illumination exists in the scene is exploited. Utilizing a background subtraction approach, regions of the frame containing objects can be extracted and their midpoints calculated. This centroid's information is then fed into the multitarget tracking system, which outputs a list of tracks and the associated measurements for each data set. From this data, the feature vectors as described in the previous section are calculated.

Since manual feature selection was performed, Principal Component Analysis (PCA) is used to validate the selection. An example of the outcome is provided in Figure 11.3. As can be seen, visualising the first and second component shows that clusters form for all of the 4 classes.

Figure 11.3: Visualisation of the feature space using the first and second component obtained via PCA for position *edge*.

4 Experimental results

In order to demonstrate the success of the method, a random forest classifier consisting of 10 estimators was trained on the data. As a measure of quality, Matthews correlation coefficient (MCC) [11] is used. Firstly, the entire data was used both for training and testing in order to estimate an upper bound of the performance. For all observation areas and classes, excellent values ranging between 0.98 and 1.0 were obtained. This clearly indicates that classes can be discriminated on basis of the data.

Secondly, training and testing via cross validation was performed. For this purpose, 60% of the data was used for training. Obtained

results as shown in Figure 11.4 (b) allow for several conclusions. In general, wooden spheres and hemispheres can be detected the most accurately for all considered camera positions. It also becomes clear that classification performance increases with the length of the belt used for transportation. The latter is especially noteworthy since it leads to the conclusion that the differences in the adaption to belt velocity reveals properties which allow discrimination of the different products. A possible explanation, which is yet to be confirmed, is that at the beginning of the belt, the motion of objects is rather random due to the feeding process. In summary, results show that motion-based features are expressive key figures which can allow discrimination of products. Therefore, it is assumed that combining traditional features, such as color-based and geometric, with motion related ones results in a significant increase in classification performance and therefore minimization of the detection error in sensor-based sorting.

Furthermore, Figure 11.5 provides insights regarding the errors made during classification. For instance, from the confusion matrices, it can be seen that for the position *feeding* many wax beads are falsely classified as wooden hemispheres, while this error almost disappears for the position *edge*. However, the number of cotton balls mistakenly hold as wooden hemispheres can be observed to be almost equal for both positions.

5 Conclusion

In this paper, it was shown that motion-based features provide a powerful tool to discriminate certain products in sensor-based sorting. Therefore, the presented approach contributes towards minimizing the detection error. The approach was validated experimentally on the basis of real world data obtained using a miniature sorting system. Results indicate that the difference in adaption to the velocity of the conveyor belt reveals the most insightful properties that allow discrimination of the products.

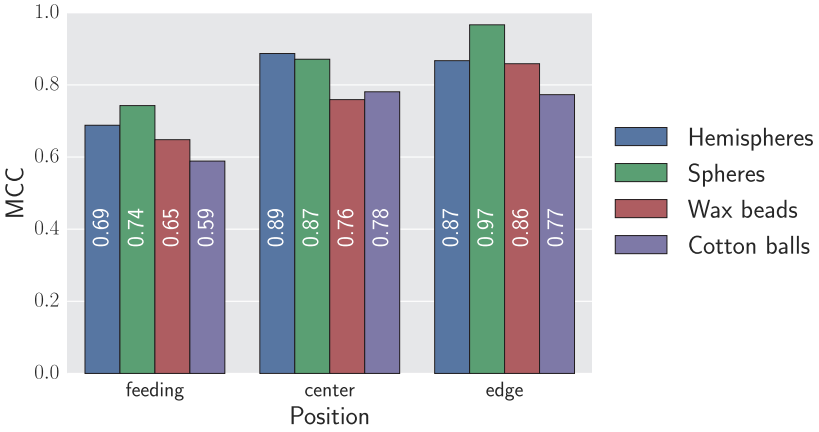

Figure 11.4: Classifier performance for cross validation (testing size 40%).

Due to the success of the method, it is intended to explore more complex motion-based features in the future. For instance, information regarding changes in direction and spin may lead to even better results. Also, for application in an industrial setting, further potential challenges, such as required computation time, need to be taken into consideration and addressed appropriately. Lastly, insights from this paper can be taken into account for system design. Instead of aiming at perfect flow control, it might be beneficial to use setups which support revelation of object characteristics by not suppressing their motion characteristics. This in turn requires precise predictions for physical separation. Hence, a potential conflict between quality of classification and separation exists.

Acknowledgment

The IGF project 18798 N of the research association Forschungs-Gesellschaft Verfahrens-Technik e.V. (GVT) was supported via the AiF in a program to promote the Industrial Community Research and Development (IGF) by the Federal Ministry for Economic Affairs and Energy on the basis of a resolution of the German Bundestag.

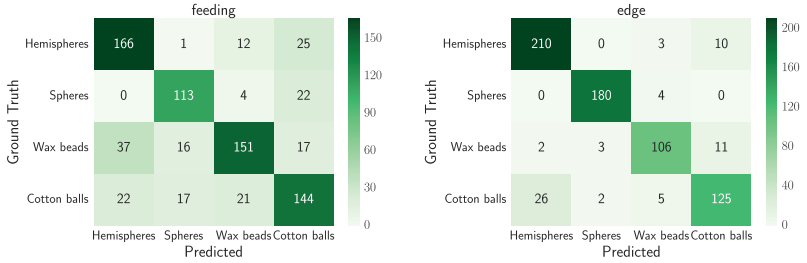

(a) Position *feeding*. (b) Position *edge*.

Figure 11.5: Confusion matrices for cross validation.

References

1. V. Narendra and K. Hareesha, "Prospects of computer vision automated grading and sorting systems in agricultural and food products for quality evaluation," *International Journal of Computer Applications*, vol. 1, no. 4, pp. 1–9, 2010.
2. W. Kepys, "Opto-pneumatic separators in waste management," *Inżynieria Mineralna*, vol. 17, 2016.
3. J. Lessard, J. de Bakker, and L. McHugh, "Development of ore sorting and its impact on mineral processing economics," *Minerals Engineering*, vol. 65, pp. 88–97, 2014.
4. F. Pfaff, C. Pieper, G. Maier, B. Noack, H. Kruggel-Emden, R. Gruna, U. D. Hanebeck, S. Wirtz, V. Scherer, T. Längle *et al.*, "Improving optical sorting of bulk materials using sophisticated motion models," *tm-Technisches Messen*, vol. 83, no. 2, pp. 77–84, 2016.
5. S. Cubero, N. Aleixos, E. Moltó, J. Gómez-Sanchis, and J. Blasco, "Advances in machine vision applications for automatic inspection and quality evaluation of fruits and vegetables," *Food and Bioprocess Technology*, vol. 4, no. 4, pp. 487–504, 2011.
6. R. Gruna and J. Beyerer, "Feature-specific illumination patterns for automated visual inspection," in *IEEE International Instrumentation and Measurement Technology Conference (I2MTC) Proceedings*, Graz, Austria, May 2012.
7. R. Mattone, G. Campagiorni, and F. Galati, "Sorting of items on a moving conveyor belt. Part 1: a technique for detecting and classifying objects,"

Robotics and Computer-Integrated Manufacturing, vol. 16, no. 2, pp. 73–80, 2000.

8. M. Richter, T. Längle, and J. Beyerer, "An approach to color-based sorting of bulk materials with automated estimation of system parameters," *tm-Technisches Messen*, vol. 82, no. 3, pp. 135–144, 2015.
9. F. Pfaff, M. Baum, B. Noack, U. D. Hanebeck, R. Gruna, T. Längle, and J. Beyerer, "TrackSort: Predictive tracking for sorting uncooperative bulk materials," in *2015 IEEE International Conference on Multisensor Fusion and Integration for Intelligent Systems (MFI)*, 2015, pp. 7–12.
10. C. Pieper, G. Maier, F. Pfaff, H. Kruggel-Emden, S. Wirtz, R. Gruna, B. Noack, V. Scherer, T. Längle, J. Beyerer *et al.*, "Numerical modeling of an automated optical belt sorter using the discrete element method," *Powder Technology*, 2016.
11. B. W. Matthews, "Comparison of the predicted and observed secondary structure of T4 phage lysozyme," *Biochimica et Biophysica Acta (BBA)-Protein Structure*, vol. 405, no. 2, pp. 442–451, 1975.

Inline density measurement for rock wool

Dirk Nüßler, Nils Pohl and Sven Leuchs

Fraunhofer FHR
Fraunhoferstraße 20, 53343 Wachtberg

Abstract Distinguishing the density of rock wool is an important part in its production process. One available common option for inline measurements of the density is based on X-rays. Due to huge security requirements in realising such measurements, this method is very complex and expensive. This paper investigates a method to find a relationship between radar based measurements and the density of rockwool. This is shown by evaluating the measurements of amplitude and phase of several rock wool samples with different densities. The results show a linear dependency of the measured phase values and the surface weights of the given samples.

Keywords Rock wool density, radar, SAMMI, surface weight.

1 Introduction

The density of rock wool is one of the distinctive features for this common product. The quality of the material depends, among other criteria, on the weight per sqm and the homogeneity. Unfortunately, the same material properties which make rock wool a perfect isolation material for buildings make it difficult to measure the density and the density distribution of the product. Typically the weight is measured with an electronic balance after the production process. Because of the good isolation properties, typical inline measurement sensors like optical camera systems, ultrasonic sensors or thermal flow thermography cannot be used. The only technical approaches which are available on the market are density measurement systems based on X-rays. Based

on the security requirements, the integration of X-ray systems into a running production process is complex. High frequency sensors offer an alternative for contactless inline density measurements and use non-ionizing radiation.

2 Hardware concept

To develop a cheap millimeter wave imaging system, it is necessary to minimize the number of active high frequency channels. The smallest number possible is a single channel sensor in combination with a 2D-mechanical scanner concept. The reduction of channels is possible through the fast measurement speed of high frequency systems. High frequency systems typically use no detector concepts, which allow update rates between several thousands and a hundred thousand measurements per second. Most scanning approaches move the high frequency sensor around the DUT in a reflection or transmission configuration. For a first test series, a rotating antenna concept was used to create a transmission image for one single frequency.

In combination with a focusing antenna, a lens system or a near field probe, these system concepts produce high resolution millimeter wave images. SAMMI [1] (see Figure 12.1) is based on a continuous wave (CW) signal system concept. The system can be roughly divided into three modules. There is a rotating transmitter module (TX), a rotating receiver module (RX) and in each case a stationary part for frequency generation and the processing of the received signals. In the transmitter path an active triple stage TX module is used to multiply and amplify the frequency up to 78 GHz. In the receiver path the received signal is converted down using a mixer. The stationarily generated frequency is used as LO and fed into the RX-Module. In the stationary RF processing, an IQ-Mixer is used for down-converting the received signal. Subsequently, the I- and Q-signals are fed to the ADC. The digital backend consists of two analogue digital converters (ADC), which are controlled and read out simultaneously by a digital logic built up on a field programmable gate array (FPGA). The arc, which is traversed by the antenna configuration eight times a second, has a diameter of 300 mm, corresponding to a circumference of 942 mm. To achieve an

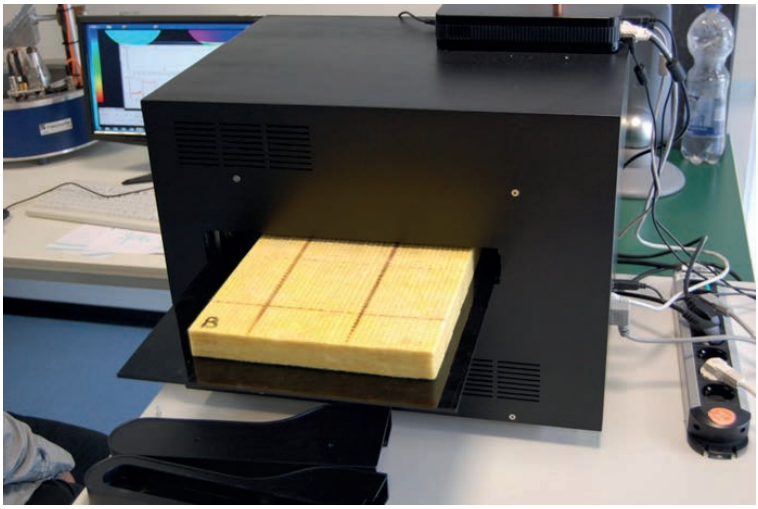

Figure 12.1: Photogaphy of a 20 cm times 20 cm large test object with the test system SAMMI (Stand Alone MM-wave Imager).

image resolution in range of one millimeter or less, the data acquisition must record at least 1000 points of measurement per round. Since amplitude an phase value must be recorded for each pixel, the number of data points sums up to 2000 measurements per round (minimum requirement). The built-in control logic assures that both channels (I/Q) are sampled synchronously, which is vital for the amplitude and phase calculation later on. For the proof of concept the further data processing (like transforming the measured arcs of pixels into a rectangular image) has been implemented on a computer. The antenna system was realized with a dielectric tip. For the tip, polyethylene (PE) with a relative permeability of 2.25 was used.

For a second test series, a motorized, linear XY-scanner stage was used in combination with a dielectric tip antenna. The system consists of two linear stages, which scan a two-dimensional grid to create the image. A program controls the frequency generation as well as the recording of the signals and the motor positions. It can even provide some simple signal processing like standardization of amplitudes

etc. The antennas mounted in the system are dielectric waveguides with their tips cut in an appropriate angle. The outer dimensions correspond to the inner dimensions of classical waveguides. Angle and length of the tips determine the gain of the waveguides, similar to horn-antennas. The advantage of this kind of antenna is the flexibility of the waveguide. As the wave is guided mostly outside the waveguides, the antennas are placed very carefully to avoid any contact with other parts of the measurement system. This system was connected to a vector network analyzer, which allows the measurement of a wider frequency spectrum.

3 Test samples

For a first test series, four samples with different densities were selected. All probes have the same thickness and structure. The only difference is the density of the four samples (see Table 12.1).

Table 12.1: Samples for the test measurement.

mineral wool	**weight [g]**	**surface [m^2]**	**Surface weight [kg/m^2]**
D1	35.1357	0.0225	1.5616
E1	29.8223	0.0225	1.3254
B1	40.7342	0.0225	1.8104
C1	43.8869	0.0225	1.9505

4 Measurements

Especially the amplitude measurements show only minimal differences between the wool samples. Like measurements with X-ray systems, the attenuation coefficient for all samples is very low and differences between the samples are very small. In contrast to the amplitude measurements, the phase results show a strong dependence on the density of the investigated material samples (compare Figure 12.2).

For a deeper analysis, we compare a measurement along a reference line (see figure 12.3). The comparison of the attenuation shows a strong

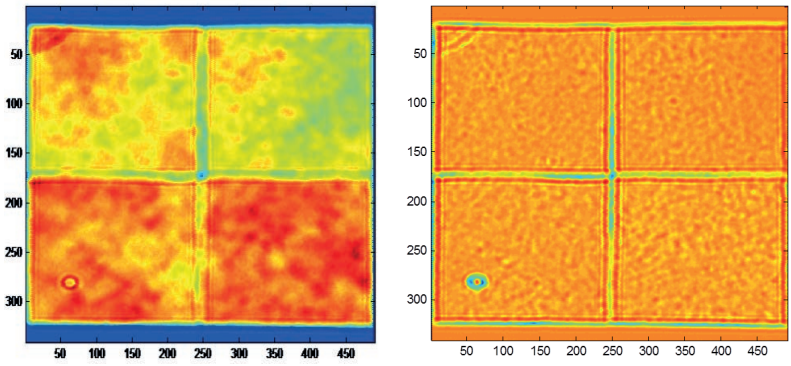

Figure 12.2: Phase measurement (left) and amplitude measurement (right)

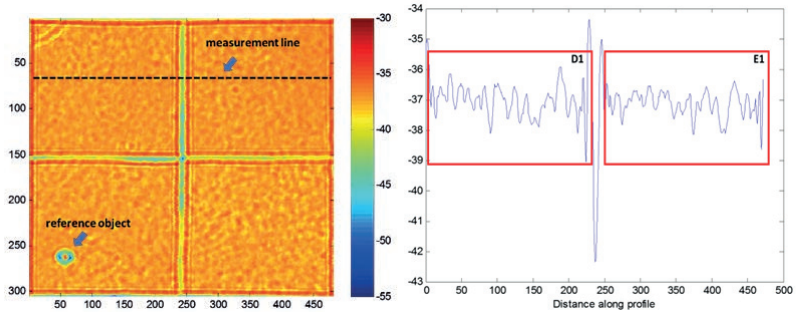

Figure 12.3: Amplitude measurement (left) and attenuation along the selected reference line (right)

fluctuation along the selected measurement line. There are only minimal differences between the two samples. Like the results from X-ray measurement systems, the small differences allow an estimation for the surface weight only through an average value over many measurement points.

With the phase measurement, high frequency sensors can measure the time delay which is caused whenever the electromagnetic wave transfer a dielectric medium. In contrast to a simple amplitude measurement, phase measurements offer a high sensitivity for even the

smallest changes in the dielectric medium. Figure 12.4 shows (comparable to the amplitude measurements in figure 12.3) the measurement along a randomly selected reference line over 2 material samples. Other than the amplitude measurement, the phase measurement shows a small but relevant phase difference between the 2 samples. As estimated, the inhomogeneity of the material causes a strong fluctuation along the reference line. For an exact estimation, a mean value over a larger number of measurement points must be created.

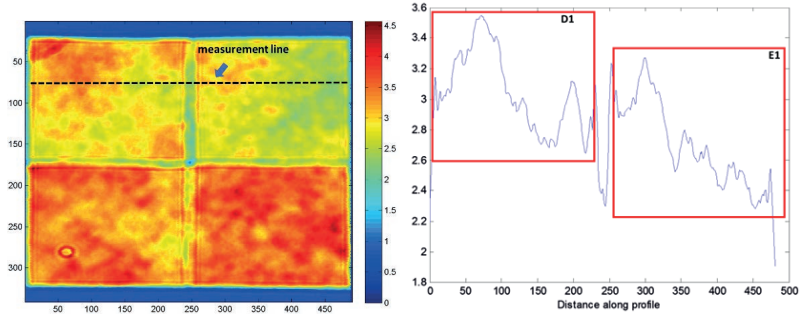

Figure 12.4: Phase measurement (left) and phase distribution along the selected reference line (right)

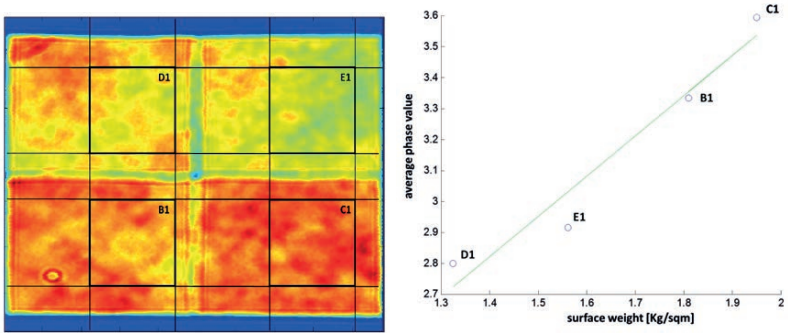

Figure 12.5: Grid creation of phase measurements (left) and appropriate mean phase values for every probe grid (right)

To evaluate how useful the mean value for the determination of the surface weight is, an average phase value over a test area is formed. The four selected test areas have equal dimensions. Figure 12.5 shows the four mean values. When comparing the values with the surface weight from table 12.1, a linear relationship between the mean values and the different material densities can be observed, visualized through the trend line in figure 12.5.

5 Summary

The paper demonstrates that the density distribution of stone wool can be measured by high frequency signals. In this the distinguished amplitudes show only small differences between the samples with different surface weights. But the analysis of the phase information offers a good alternative. Thus it was shown that the phase is related to the surface weight.

References

1. D. Nüßler, M. Schubert, S. Reible, S. Kose, T. Rosenthal, R. Salman, and N. Pohl, "T-sense - the new generation of non-contact transmission imaging with non-ionizing radiation," in *WCNDT 2016 - 19th World Conference on Non-Destructive Testing*, Munich, Germany, June 2016.

Evaluation and comparison of different approaches to multi-product brix calibration in near-infrared spectroscopy

Michael Kopf, Robin Gruna, Thomas Längle, Jürgen Beyerer

Fraunhofer IOSB, Visual Inspection,
Fraunhoferstr. 1, 76131 Karlsruhe

Abstract Near-infrared (NIR) spectroscopy became a widespread technology for qualitative and quantitative material analysis. New fields of application of this technology, e.g., quantitative food analysis for consumers, increase demand for multi-product calibration models. Conventional multivariate calibration methods, such as partial least squares regression (PLSR), are reported to show weakness in predictive performance [1]. Preliminary studies in multi-product calibration for quantitative analysis of food with near-infrared spectroscopy showed good results for memory-based learning (MBL) and a classification prediction hierarchy (CPH) [2]. In this study, three varieties of apples, pears and tomatoes with known °brix value are analyzed with NIR spectroscopy in the range from 900 nm to 2400 nm. Predictive performance of a linear PLSR model, two non-linear models (CPH and MBL) and different preprocessing techniques are tested and evaluated. For error estimation, leave-one-product-out and leave-one-out cross-validation are used.

Keywords: NIR, chemometrics, nutrition, multi-product calibration.

1 Introduction

Near-infrared spectroscopy became a widespread technology for quality inspection and optical sorting issues. Due to its ability for nondestructive quantitative and qualitative analysis, it can be found in production chains and in laboratories. Unlike mid-infrared, quantitative

information can not be read directly from the spectrum. Mathematical methods and models, called chemometric methods, must be applied to gain information. For quantitative analysis in NIR spectroscopy partial least squares regression and principal component regression are gold standard methods [3]. With increasing interest in new areas of application, such as the handheld food scanners for consumers [4, 5], the requirements for chemometric methods changed. In contrast to laboratory tasks, there is no prior knowledge about the samples being scanned. Robust multi-product calibrations are necessary. Preliminary studies in memory-based learning and a classification prediction hierarchy showed promising results [2]. In this experiment, those two nonlinear methods and a linear PLSR model were tested and evaluated. The task was to predict the °brix value, which is highly correlating to sugar content, for three apple varieties, tomatoes and pears. To this end, hyperspectral short wave infrared (SWIR) images were used. Five preprocessing techniques and combinations of them were tested: first and second derivative, standard normal variate transformation (SNV), multiplicative scatter correction (MSC) and absorbance transformation.

2 Material and methods

2.1 Data acquisition

Three varieties of apples (Jonagold, Gala and Elstar) were used to get product separation on different levels. For a separation on a higher product level, tomatoes and pears were added to the samples. Each fruit was cut into two halves, the ripest and the most unripe half. A SWIR line camera was used to obtain hyperspectral reflectance images in the range of 900 nm to 2400 nm. Six halogen lamps in bright field constellation were used as light source. Dark and white reference images were acquired at the beginning of each measurement and used for reflectance calculation. For the white reference image, a white teflon bar was used. A total amount of 124 pear, 454 apple (146 Elstar, 146 Gala, 162 Jonagold) and 90 tomato images were taken. After the hyperspectral image acquisition of each half, its middle third part was extracted and pressed to juice. The °brix value for each half was determined with a refractometer.

2.2 Data processing

After defective pixel elimination, reflectance calculation and segmentation, the median spectrum from each image was calculated. A median spectrum is more robust against outliers and other influences than the raw point spectra. The median spectra serve as basis for further preprocessing and analysis.

Preprocessing was used to remove scatter effects or to extract different features. First two derivatives, SNV and MSC are used as well as absorbance transformation in combination with the other preprocessing techniques.

PLSR A conventional PLSR from the *R*-Package *PLS* [6] was used as linear calibration. The number of components was chosen via leave-one-product-out (LOPO) and leave-one-out (LOO) cross-validation. All data were pooled to one dataset for training and validation to test multi-product prediction performance.

MBL In contrast to so called eager learning, like PLSR, there is no offline training in memory-based learning or lazy learning. To predict the response variable(s) for a sample, a distance metric is used to find nearest neighbours in the training data. A regression model is trained with those nearest neighbours on demand (see Fig. 13.1). Parameters to set are among others the distance metric to find the nearest neighbours, the number of neighbours, the regression algorithm and the use of the dissimilarity matrix. The used *R*-package *resemble* [7] offers three kinds of distance metrics and four regression methods (see [7] for more details). It is also possible to use the distance information as additional predictor variables or as weights for weighted regressions.

CPH Another approach for multi-product calibrations is classification prediction hierarchy (CPH). For each class or subclass, a specialized regression model is trained. For prediction, the optimal model is chosen by a classifier. Then the regression model predicts the response variable. Due to the bad results for applying a specialized model to another class than it was trained on [2], the models are evaluated only with LOO cross-validation.

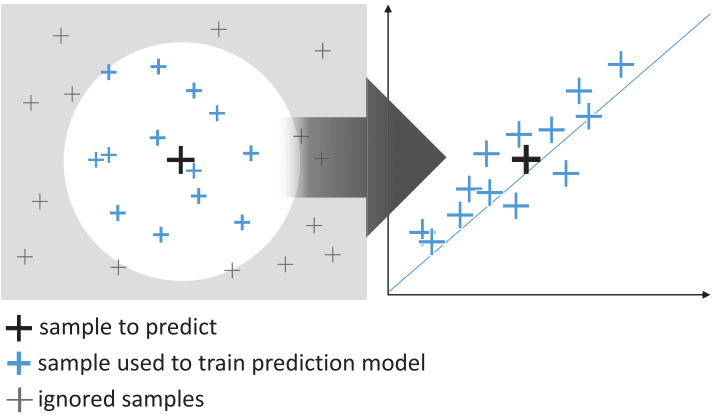

Figure 13.1: Memory-based learning: prediction model is build on demand with the nearest neighbours of the new sample.

2.3 LOPO cross-validation

To validate the calibration models, a leave-one-product-out cross-validation was used. To estimate the ability of prediction on materials that are not in the training set, the models were trained with all classes but one. The class left out was used for validation (Fig. 13.2). The root mean square error of cross-validation (RMSECV) was used as error function:

$$\text{RMSECV} = \sqrt{\frac{\sum_{i=1}^{n} (p_i - r_i)^2}{n}},$$

where p_i is the i-th predicted value, r_i is the i-th observed reference value, i is in the range of $[1, n]$ and n is the number of test samples.

3 Results

PLSR Best linear calibration model for a LOO cross-validation was trained with 16 components and absorbance transformation as preprocessing (Fig. 13.3 left). The RMSECV is 0.78 °brix. With a LOPO cross-validation best PLSR model was gained with absorbance trans-

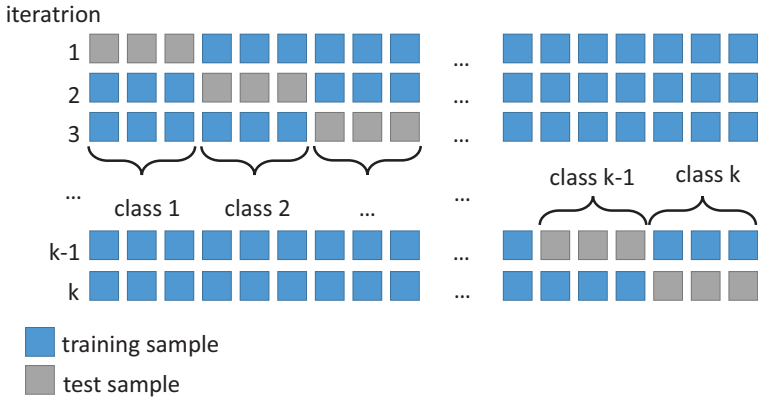

Figure 13.2: Leave-one-product-out cross-validation with *k* classes.

formation and MSC as preprocessing. The RMSECV is 1.13 °brix with 6 components.

MBL Memory-based learning calibrations were tested with LOPO cross-validation to estimate the ability for predicting unknown materials. Only little improvement to the PLSR model is possible with a MBL calibration that uses euclidean distance for dissimilarity calculation, PLSR as regression algorithm with 8 components for prediction, dissimilarity matrix as additional predictor variables and 300 nearest neighbours. Samples were preprocessed by an absorbance transformation. The root mean square error of cross-validation was 1.11 °brix (see Fig. 13.4 left).

CPH Linear discriminant analysis was used to classify and to choose prediction models. Best models were obtained with 6 components PLSR and MSC preprocessing for pears, 12 components PLSR and absorbance transformation for Elstar apples, 13 components PLSR and absorbance transformation for Gala apples, 17 components PLSR and SNV after absorbance transformation for Jonagold apples and 7 components and SNV after absorbance transformation for tomatoes. With

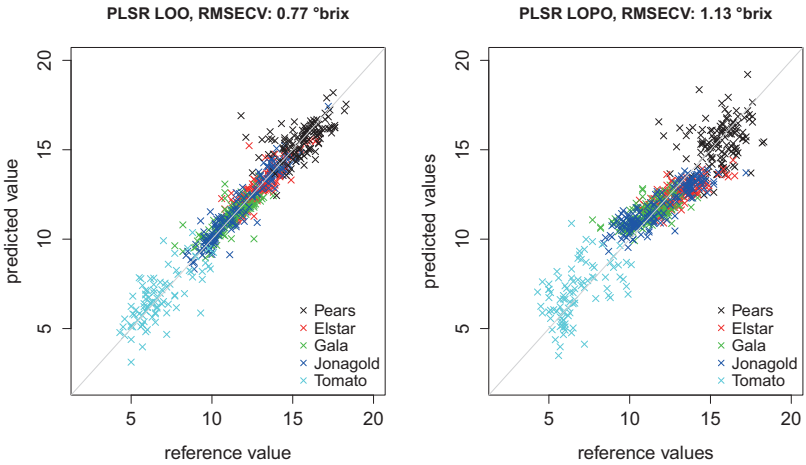

Figure 13.3: Left: best PLSR °brix calibration model, validated with LOO cross-validation, absorbance transformation as preprocessing. Right: best PLSR °brix model, validated with LOPO cross-validation, absorbance transformation and MSC as preprocessing.

those specialized models a RMSECV of 0.73 °brix was reached in LOO cross-validation (see Fig. 13.4 right).

4 Conclusion

In contrast to the study of Micklander et al. [1], where PLSR calibrations showed weakness in prediction compared to nonlinear methods as local regressions and neuronal nets, a linear multi-product calibration for °brix value on apples, pears and tomatoes shows comparable accuracy to nonlinear models. MBL and CPH can only reach little improvement in predictive performance. A hierarchical calibration, such as the classification prediction hierarchy, can increase accuracy in °brix prediction for apple varieties, pears and tomatoes from 0.78 °brix to 0.73 °brix.

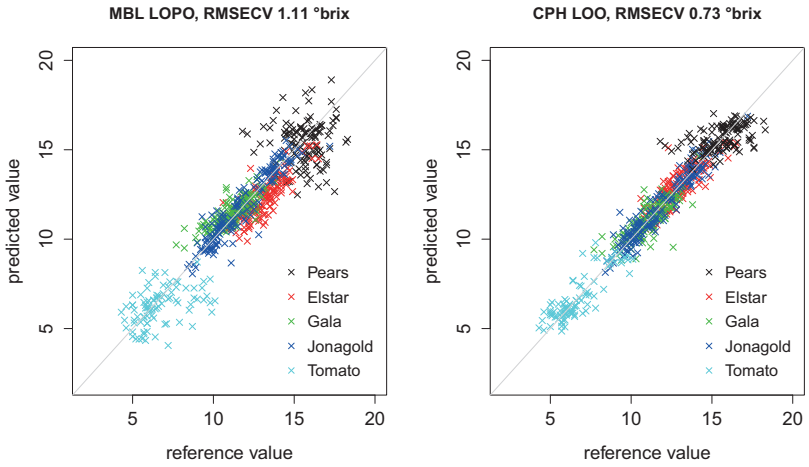

Figure 13.4: Left: best MBL °brix calibration for LOPO with 300 nearest neighbours and absorbance transformation as preprocessing. Right: best CPH °brix model, validated with LOO cross-validation.

Memory-based learning as multi-product calibration approach reaches little better result for leave-one-product-out cross-validation than the pooled PLSR model. The RMSECV for best PLSR model is 1.13 °brix while MBL reaches 1.11 °brix. Especially memory-based learning has a high calculation effort by calculating big dissimilarity matrices for nearest neighbour search, which slows down prediction. As you can see in Fig. 13.3 right, the outer classes, pears and tomatoes, have a higher error and a higher deviation than the apple varieties in a LOPO cross-validation. When predicting in a LOPO cross-validation, the model has to extrapolate the response variable, which might cause the higher error, as conventional regression models are said not to be able to extrapolate without loss in accuracy [8]. Same effects are noticeable for MBL calibrations (Fig. 13.4).

References

1. E. Micklander, K. Kjeldahl, M. Egebo, and L. Norgaard, "Multi-product calibration models of near infrared spectra of foods," *Journal of Near Infrared Spectroscopy*, vol. 14, pp. 395–402, 2006.
2. M. C. Kopf and R. Gruna, "Examination of multiproduct calibration approaches for quantitative analysis of food with near infrared spectroscopy," Bachelor's thesis, 2016.
3. H. W. Siesler, Y. Ozaki, S. Kawata, and H. M. Heise, Eds., *Near-Infrared Spectroscopy: Principles, Instruments, Applications (Chemistry)*, 1st ed. Wiley-VCH Verlag GmbH & Co. KG, 2002.
4. K. Grifantini, "Knowing what you eat: Researchers are looking for ways to help people cope with food allergies," *IEEE Pulse*, vol. 7, 2016.
5. H. Schulte, G. Brink, R. Gruna, R. Herzog, and H. Grueger, "Utilization of spectral signatures of food for daily use," in *OCM 2015 - Optical Characterization of Materials - conference proceedings*, 2015.
6. R. W. Bjorn-Helge Mevik and K. H. Liland, "pls: Partial least squares and principal component regression," CRAN repository. [Online]. Available: https://CRAN.R-project.org/package=pls
7. L. Ramirez-Lopez and A. Stevens, "resemble: Regression and similarity evaluation for memory-based learning in spectral chemometrics," CRAN repository, 2016. [Online]. Available: https://CRAN.R-project.org/package=resemble
8. E. W. Ciurczak and D. A. Burns, Eds., *Handbook of Near Infrared Analysis*, 3rd ed. Practical Spectroscopy, 2007.

Optical characterization of artist's materials in ancient paintings by spectral imaging in the VIS-IR range

Nicole de Manincor[1], Giacomo Marchioro[1], Vittorio Barra[1], Ornella Salvadori[2], Claudia Daffara[1]

[1] Department of Computer Science, University of Verona
Strada le Grazie 15, 37134 Verona, Italy
[2] Gallerie dell'Accademia di Venezia, Laboratori della Misericordia
Cannaregio 3553, 30121 Venezia, Italy

Abstract In the last few years, the non-invasive infrared reflectography (IRR) imaging technique has been improved by means of the multispectral option both in the VIS and in the NIR range in order to achieve more reliable and accurate results. Hence, the collected data can be visualised and studied both in the spatial and in the spectral domain, being processed as reflectographic images or as punctual reflectance spectra of the materials composing the painting.

This work presents the formulation and application of an easy-to-use methodology to identify and map the original artist's pigments in ancient paintings starting by a set of spectral data acquired with multispectral imaging technique in the VIS-NIR range. The preliminary results shown are obtained on a painting by Vittore Carpaccio, belonging to the collection of *Gallerie dell'Accademia* in Venice, Italy.

Keywords: Multispectral imaging, VIS-NIR, ancient paintings.

1 Introduction

1.1 Infrared reflectography

Since its introduction in the first half of the twentieth century [1], and the following work of Van Asperen de Boer [2], Infrared Reflectography

(IRR) has been increasingly employed for the analysis of ancient paintings, and becoming routinely utilized either in situ or in conservation laboratories as a major non-invasive imaging tool for the diagnostic process before any planned intervention.

This technique is based on the ability of NIR wavelengths (0.8 – 2.5 μm) to penetrate the pictorial layers – thanks to the partial transparency of most of the pigments in this spectral region – down to the preparatory ground (consisting in chalk or gypsum and glue) that is generally highly reflective, and thus allowing the detection of features beneath the paint surface, such as, for instance, the underdrawing (executed by means of a carbon black medium) that results in absorption. These differences in reflectivity also allow the detection of *pentimenti*, retouchings, paint losses, paint integrations and subsequent restorations.

The traditional reflectographic imaging method is performed in wide-band modality by irradiating the artwork with a single large band in the NIR range and by acquiring the backscattered radiation with suitable devices, and so obtaining an IR image, called reflectogram.

The capability to detect underlying features relies on the composition (materials and technique) of the investigated painting as well as on the characteristics of the employed imaging system [3].
Down the years, different NIR imaging devices have been used and implemented for IRR analyses, such as the early PbO-PbS Vidicon cameras used by Van Asperen De Boer [4], Si-based CCD cameras [5], up to the most recent scanning systems with InGaAs or PtSi detectors [6].

1.2 Multispectral imaging in the VIS-NIR range

In the last few years, the application of the multispectral imaging (already employed in geophysical remote sensing [7]) in the field of cultural heritage has improved the traditional wide-band IRR [8] [9], allowing the most effective range of wavelengths to be tailored to fit the specific case.

Multispectral imaging in the VIS-NIR is performed by irradiating the painting with a broadband source and by collecting the backscattered radiation within narrow spectral VIS-NIR bands. This spectral imaging technique allows the simultaneous collection of both spectral data and spatial information (high-resolution images), thus the result of the

acquisition is a multiband stack of VIS and NIR images, which can be processed to extract the information [10]. The so-called multispectral cube (Fig. 14.1) can be analysed as a set of wavelength resolved images in NIR range (multi-NIR reflectography) or as a series of spatially resolved point reflectance spectra, one for each sampled pixel on the surface, both in the VIS and NIR range (VIS-NIR spectrometry) [6].

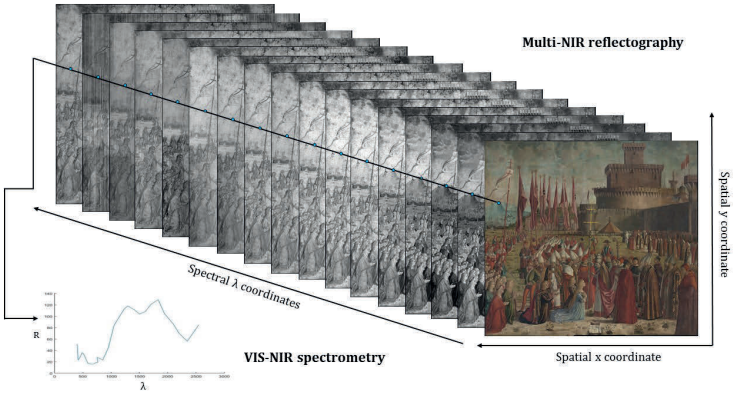

Figure 14.1: Multispectral cube.

In the multi-NIR reflectography method, the visualization of images in each band separately is useful for a manual inspection of the varied reflectance changes of particular areas. Thus, specific hidden features not visible or barely visible in wide-band modality can be detected.

The VIS-NIR spectrometry approach allows the use of the multispectral imaging for the non-invasive pixel-by-pixel qualitative recognition of similar-appearing pigments exploiting their VIS to NIR differences in diffuse reflection spectra [11].

The extraction of the reflectance spectra from the multispectral cube can be made by means of specific scripts or dedicated software. Then, in principle, a comparison between the obtained spectra and reference spectra (e.g. from punctual spectrometry techniques) helps to successfully assign each acquired spectrum to the correspondent pigment.

The identification of pigments by means of VIS-NIR spectrometry depends on the spectral range and on the spectral resolution of the device, as well as on the characteristics of the reflectance spectra of the materials under investigation. A spectral resolution in the device of about 100 nm seems to be sufficient to discriminate most of ancient pigments, which exhibit variations larger than 100 nm in the spectrum [12], otherwise, more sophisticated tools, i.e. hyperspectral devices, are necessary for pigments identification [13].

In the study of real paintings' reflectance spectra, pigments identification is not so straightforward, because the paint layering and the penetration depth of IR radiation through the layers must be taken into consideration, as these variables could lead the acquired spectra not matching the reference ones perfectly.

2 Materials and methods

2.1 The VIS-NIR multispectral scanner

The image dataset was acquired using the multispectral VIS-NIR technology, a multiband scanner available by the Iperion CH infrastructure [14].

The detection unit of the Iperion CH scanner includes a 16 channels IR module (750–2500 nm) and a 16 channels VIS module (380–780 nm), thus providing a set of 32 spatially-registered images at each acquisition. The detectors are Si (380–1000 nm) and InGaAs (1050–2500 nm) photodiodes equipped with interferential filters with a spectral width that ranges from about 20 to 30 nm for the VIS module and from 66 to 120 nm for the IR module. The image data acquired by the multiband scanner are aberration-free and hardware registered, not requiring any post-processing to be corrected or aligned.

2.2 Methodology

In this work, it is discussed a reliable and simple methodology for optical characterization of the original artists' pigments in ancient paintings, starting from the multispectral imaging in the VIS-NIR range and exploiting the dual approach of this technique.

To achieve this result, it was necessary to provide a set of reference material reflectance spectra in the same range.

The data analysis workflow is structured as follows:

1. Retrieving (and/or implementing) a spectral reference database
2. Process the spectral library for an effective comparison with the spectra extrapolated from the multispectral cube of the scanner
3. Visualization of the RGB image in the VIS range to choose the areas suitable for pigments discrimination (ROI, region of interest)
4. Material segmentation to optically discriminate the identified pigments in the image
5. Validation by means of further complementary analysis (e.g. XRF spectrometry)

Since the production of a spectral database using the same instrument employed to collect the multispectral cube is not easy and straightforward, the pipeline here developed uses reference spectra from third party database. In this paper it has been used the FORS database of CNR IFAC [15].

Different devices with different optical configurations and resolutions have been employed to record the reference spectra and the multispectral stack, and this raises the issue of the effectiveness of the comparison between the acquired data.

To overcome this problem, here it has been developed and followed a workflow to homogenize the resolution of the two instruments: the spectra retrieved from the database has been downsampled to the resolution of the multispectral scanner by averaging the reference spectra values in the bandwidth computed at full width at half maximum (FWHM) of the transmittance of each filter of the multispectral scanner:

$$\frac{1}{\lambda_f - \lambda_i} \int_{\lambda_i}^{\lambda_f} \lambda \, d\lambda$$

where λ_i and λ_f are the bandwidth limits.

The figure 14.2 shows the reference spectrum, the reflectance recorded for each scanner band, and the computed average reflectance in the bandwidth interval of each single band.

To achieve more accurate results, the transmittance curve – characteristic of each filter – could be calculated to retrieve the average reflectance data, even if this information is not always available or easy to find for online databases.

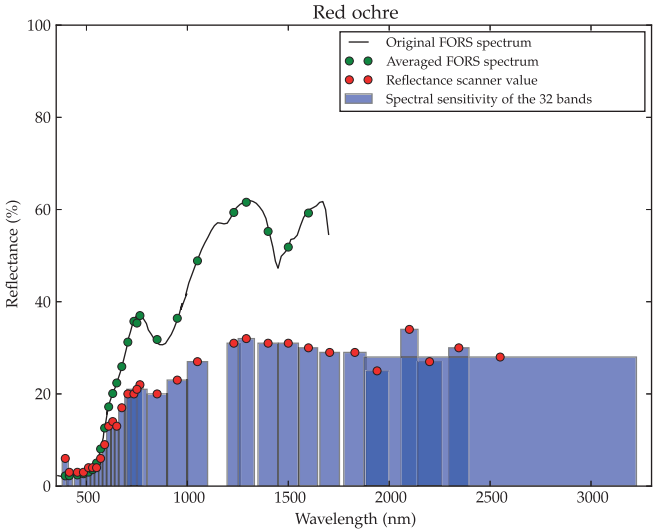

Figure 14.2: Comparison between the reference spectrum, the values recorded by the multispectral scanner (red dots) and the averaged reference values (green dots) computed in the FWHM interval of the spectral bands (blue bars).

Once the reference spectra have been processed in a single matrix, each spectrum extrapolated from the multispectral cube can be then compared with the reference from the library. For this purpose, two different algorithms commonly used in remote sensing have been implemented using Python and tested: the minimum distance and the spectral angular mapping (SAM).

The minimum distance is calculated using the following formula:

$$\frac{1}{N}\sum_{n=1}^{N}\sqrt{(x_{cube}-x_{ref})^2}$$

where N is the number of bands and x is the reflectance values of the single pixel of the band n of the hyper-spectral cube and the reference database. The SAM algorithm has been implemented referring to [16].

While for the SAM method no normalization has been necessary to achieve an effective classification, for the minimum distance method a min-max normalization of the spectra has been performed before computing the distances.

The pixel is attributed to the pigment whose reference spectra shows the lowest spectral distance and/or the lowest spectral angle.

In the end, the attribution can be eventually validated comparing the results with other data, for instance performing XRF analysis over the different areas.

Figure 14.3: RGB visible image of the selected ROI under study.

3 Results

The above methodology has been tested to identify and distinguish among four red pigments in the canvas *Incontro dei pellegrini con Papa Ciriaco* by Vittore Carpaccio. The ROI selected for pigment identi-

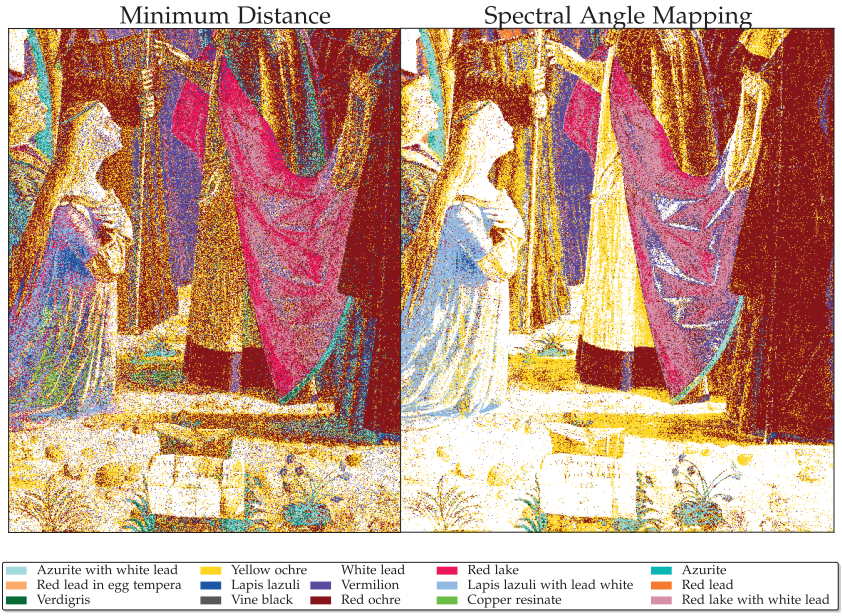

Figure 14.4: Comparison of the two classification of the pigments in the painting using the two algorithms here implemented.

fication represents the meeting of prince Ereo and princess Orsola, knelt down in sign of respect and devotion, and Pope Ciriaco, who is welcoming and baptizing the couple (Fig. 14.3). This area has been chosen because of the great variety of reds, easily distinguishable even in the RGB image.

The final output of the classification is a colour-coded image where a colour has been attributed to a pigment or a mixture of pigments (Fig. 14.4). To have an insight on the quality of the assignment, for every pixel of the image it is plotted the spectral distance and the spectral angle between the spectrum acquired from the hyperspectral cube and the reference spectrum from the database (Fig. 14.5). Low values mean a better matching between the spectra, while high values means that the attribution has been made in spite of the significant difference between the reference and the recorded spectrum.

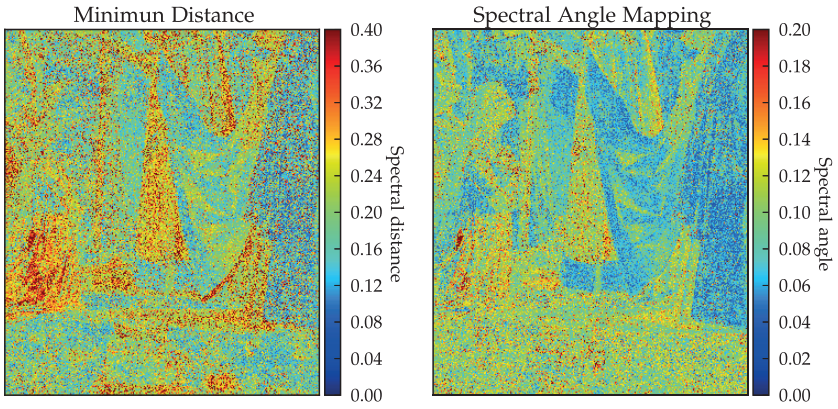

Figure 14.5: The spectral distance and the spectral angle between the reference spectrum and the sample spectrum for every pixel of the image.

4 Summary

4.1 Discussion and conclusions

A short introduction to Carpaccio's artistic technique for the pigments studied here is necessary before presenting the results. Carpaccio was renowned for his vivid and brilliant reds; indeed, red is the most outstanding colour in this painting.

Observing the VIS RGB image, red is present in virgins' dresses, in Pope, clerics and laics' choir dresses, in cardinals' *birettas* (hats) and in the flags.

In spite of the colouristic effects Carpaccio reached with red pigments, from previous studies made on other paintings it is known that his technique in red painted areas is, in fact, simple. He used to obtain the desired effect with the application of only one or two brushstrokes. In red painted layers, all the pigments commonly in use in that period were found: cinnabar, red lead, red ochre, red lake and, less extensively, realgar. Vermilion or red ochre were often used as first paint layers, over which red lake was applied as a glaze in the shadows. Red lead was mostly employed alone [17,18].

The proposed methodology allowed the identification and mapping of different pigments: the minimum distance algorithm succeed in the attribution of vermilion, red ochre and red lake, but failed in identifying red lead, while the SAM algorithm distinguished an area where this pigment is present. XRF analysis[3] on red areas confirmed the attributions.

A comparison between the results obtained by the XRF and those achieved by means of the algorithms here used suggests that spectral angle algorithm performs generally better than the minimum distance one. However, the minimum distance algorithm provides some further information: studying the spectral distance plot (Fig. 14.5), it can be observed an area in Orsola's dress where the distances between the spectra is grater and this area has been identified as a restored area where several retouches have been made. The same plot also highlights the uncertainty of the attribution of the black stripe at the end of Pope Ciriaco's cloak, here attributed to verdigris, while it is probably composed of a black pigment (visually comparing it to other dark areas in the painting).

The preliminary results presented in this work demonstrate the potentiality of the spectral imaging in the VIS-IR range for an effective characterization of the artist's materials in ancient paintings. Further work will be carried out in the framework of an interdisciplinary collaboration with the museum operators.

[3] Dr. Enrico Fiorin personal communication (2015)

Acknowledgments

This work was partially supported by the Scan4Reco project funded by EU Horizon 2020 Framework Programme for Research and Innovation under grant agreement no 665091. The diagnostic procedure on Carpaccio has been made possible by a collaboration between the *Laboratorio Scientifico della Soprintedenza speciale per il Patrimonio storico, artistico ed etnoatropologico e per il Polo museale della città di Venezia e dei comuni della Gronda lagunare*, the University of Verona and the Italian infrastructure IPERION_CH.it, as part of the project Iperion CARP-ID.

References

1. R. Mancia, *L'esame scientifico delle opere d'arte ed il loro restauro*. Ulrico Hoepli, 1944.
2. J. R. J. Van Asperen De Boer, "Infrared reflectography: a method for the examination of paintings," *Applied Optics*, vol. 7, no. 9, pp. 1711–1714, 1968.
3. E. Walmsley, C. Metzger, J. K. Delaney, and C. Fletcher, "Improved visualization of underdrawings with solid-state detectors operating in the infrared," *Studies in Conservation*, vol. 39, no. 4, pp. 217–231, 1994.
4. J. R. J. Van Asperen De Boer, "Reflectography of paintings using an infrared vidicon television system," *Studies in Conservation*, vol. 14, no. 3, pp. 96–118, 1969.
5. E. Walmsley, C. Fletcher, and J. Delaney, "Evaluation of system performance of near-infrared imaging devices," *Studies in Conservation*, vol. 37, no. 2, pp. 120–131, 1992.
6. C. Daffara, E. Pampaloni, L. Pezzati, M. Barucci, and R. Fontana, "Scanning multispectral IR reflectography SMIRR: an advanced tool for art diagnostics," *Accounts of chemical research*, vol. 43, no. 6, pp. 847–856, 2010.
7. J. Solomon and B. Rock, "Imaging spectrometry for earth remote sensing," *Science*, vol. 228, no. 4704, pp. 1147–1152, 1985.
8. C. Fischer and I. Kakoulli, "Multispectral and hyperspectral imaging technologies in conservation: current research and potential applications," *Studies in Conservation*, vol. 51, no. sup1, pp. 3–16, 2006.
9. M. Gargano, N. Ludwig, M. Milazzo, G. Poldi, G. Villa, C. Parisi, G. Buzzanca, and A. Paradisi, "A multispectral approach to ir reflectography," in *Art '05–8th International Conference on Non-Destructive Investigations and*

Microanalysis for the Diagnostics and Conservation of the Cultural and Environmental Heritage., Lecce, Italy A, vol. 148, 2005.

10. C. Daffara and R. Fontana, "Multispectral infrared reflectography to differentiate features in paintings," *Microscopy and Microanalysis*, vol. 17, no. 5, pp. 691–695, 2011.
11. A. Casini, F. Lotti, M. Picollo, L. Stefani, and E. Buzzegoli, "Image spectroscopy mapping technique for noninvasive analysis of paintings," *Studies in conservation*, vol. 44, no. 1, pp. 39–48, 1999.
12. J. K. Delaney, E. Walmsley, B. H. Berrie, and C. F. Fletcher, "Multispectral imaging of paintings in the infrared to detect and map blue pigments," *Proceedings of the National Academy of sciences*, pp. 120–136, 2005.
13. J. K. Delaney, J. G. Zeibel, M. Thoury, R. Littleton, M. Palmer, K. M. Morales, E. R. De La Rie, and A. Hoenigswald, "Visible and infrared imaging spectroscopy of picasso's harlequin musician: mapping and identification of artist materials in situ," *Applied Spectroscopy*, vol. 64, no. 6, pp. 584–594, 2010.
14. R. Fontana, M. Barucci, E. Pampaloni, J. Striova, and L. Pezzati, "From leonardo to raffaello: insights by vis-ir reflectography," *Acta Artis Academica, Interpretation of Fine Art's Analysis in Diverse Contexts*, 2014.
15. Fiber optics reflectance spectra (FORS) of pictorial materials in the 270-1700 nm range. [Online]. Available: http://fors.ifac.cnr.it/
16. F. A. Kruse, A. B. Lefkoff, J. W. Boardman, K. B. Heidebrecht, A. T. Shapiro, P. J. Barloon, and A. F. H. Goetz, "The spectral image processing system (SIPS)—interactive visualization and analysis of imaging spectrometer data," *Remote sensing of environment*, vol. 44, no. 2, pp. 145–163, 1993.
17. D. Radeglia and others, *L'arrivo a Colonia di Vittore Carpaccio: Studio e restauro*. Gangemi Editore spa, 2015.
18. G. N. Sciré and S. Rossi, *Vittore Carpaccio: tre capolavori restaurati*. Marsilio, 2007.

Characterization of sizes on textiles by in-line NIR chemical imaging

Gabriele Mirschel[1], Olesya Daikos[1], Carsten Steckert[2], Katja Heymann[1]*, Tom Scherzer[1]

[1] Leibniz Institute of Surface Modification, Chemical Department, Permoserstr. 15, D-04318 Leipzig, Germany
[2] LLA Instruments GmbH, Justus-von-Liebig-Str. 9/11, D-12489 Berlin, Germany

Abstract In the last years, demands on high quality products increases dramatically, e.g. in textile industry. In order to produce high functional textiles a numerous of chemical agents have to be applied to the fabrics, in several wet chemical treatments, in the production process. One auxiliary agent is the size. Sizes are colorless, water soluble substances which improve the mechanically stiffness of threads during weaving process. Usually, sizes have to be wash out of the fabric before further processing since they may affect the following production steps. Up to now, offline process control methods e.g. extraction of the size are the state of the art of process control in textile industry. It is obvious, that the time consuming and punctual analytical methods are no more seasonable for an optimal process control. Thus, alternative process control methods were on demand.

This paper presents a study of the potential of NIR hyperspectral imaging for in-line analysis in textile technology. Application weights and spatial distribution of sizes on polyester fabric are investigated by NIR hyperspectral imaging. In a preliminary study a calibration to the application weight of the size was prepared and a PLS model was established. This PLS model was applied for the quantitative monitoring of the colorless size across the fabrics. Additionally, contaminants on the textile were visualized by NIR chemical imaging. Thus, NIR hyperspectral imaging is presented as a fast, precise and powerful analytical method which also fulfills the requirements of textile industry.

Keywords: Process control, in-line monitoring, technical textiles, chemical treatment, sizing, homogeneity.

1 Introduction

In textile technology, fabrics or threads were usually treated with various chemical agents in order to improve stiffness of the threads or to obtain a specific functionality of the refined textile. These chemical substances can be divided into two main categories: finishes and auxiliary agents. Finishes are responsible for the final characteristic of the textiles and remain on the fibers, whereas auxiliary agents such as sizes are employed to improve the mechanically stiffness of the threads during weaving process and have to be washed out before further processing.

Both finishes and sizes are usually water soluble, colorless substances, which are applied to the fabrics or threads in a wet chemical process. Both fabrics and threads are pulled through a bath, in which the specific agent is dissolved. Afterwards, excess water is squeezed out and fibers are allowed to dry before further processing. Commonly, fabrics or threads pass several impregnation or washing steps until a finished functional textile is engendered. After each dipping step not only the quantitative amount of chemical substances at the fibers is essential for the final product quality, but also its homogeneous distribution is a basic requirement of a high quality product.

It is obvious, that a visual inspection of the distribution of the agents is hardly possible due to the colorless character of the finishes and auxiliary agents. Up to now, the common method for process control is a cost-intensive and laborious work, in which random samples are cut out of the fabric and weighted. Additionally, the specific substance may be also extracted from the textile in analytical laboratories in order to confirm the determined application weight. In the last decades, this kind of off-line process control was the state of the art and was thus considered as a sufficient method.

Nowadays, the requirements regarding the quality of specific products permanently increase. Therefore, powerful methods for process control become more and more important. It is nowhere near enough to determine merely the application weight, but the spatial distribu-

tion of the substances is also of great interest for the textile industry. Furthermore, contaminations of the textile web may occur during processing, when liquids, e.g. finishes, sizes, greases or machine oil, drop down from other parts of the machine. Again, these contaminants are either colorless or have pale color and are hence, invisible or at least difficult to detect by the eyes. Furthermore, the blots may strongly affect further processing such as printing, finishing or lamination. Thus, detection and possibly identification of the contaminants as well as monitoring of their distribution on the textile web is essential for an optimal process control.

In general, spectroscopic methods are commonly used for process control, since they are practicable, fast and mostly contact-free analytical methods. In particular, NIR spectroscopy is employed for product control in agriculture, food and chemical industries for the last three decades [1–6]. With the development of NIR multispectral cameras, the scope of NIR spectroscopy was enlarged. Up to now, NIR hyperspectral cameras may be used as process control instruments, since the monitoring of the spatial distribution of compounds or parameters of interests is a great benefit. On the basis of chemometric approaches powerful calibration models can be developed, which enable both the identification of different compounds as well as quantitative monitoring of the distribution of specific agents across the web. Nowadays, research areas employing NIR chemical imaging as analytical technique cover a wide range. Among others, monitoring of foods, medical or chemical products should be mentioned [7–11].

In textile industries, NIR spectroscopy was occasionally applied for the analysis of textile blends or for the determination of the concentration of some processing additives [12–14]. In a previously published paper, in-line analysis of textile laminates, especially the monitoring of the homogeneity of adhesive layers between the textile fabrics, by NIR chemical imaging was described [15]. However, the distribution of auxiliary agents on textile fabrics has never been analyzed before by NIR spectroscopy or hyperspectral imaging. The present paper is focused on the analysis of sizes as well as the detection of contaminants on textile webs by NIR chemical imaging.

2 Experimental

Sample preparation Polyester fabrics investigated in this study were kindly provided by a textile finishing company. Sizes were applied to the fabrics by padding the fabrics in a size-containing solution in a laboratory foulard (HVF 58401, Werner Mathis AG, Oberhasli, Switzerland). Subsequently, fabrics were spanned in a tentering frame (LTE-S 54101, Werner Mathis AG) and were dried at 100°C. The size of the fabrics was approximately 100 x 170 mm. The application weights of the size were determined by a textile laboratory (CHT/Bezema, Tübingen, Germany) by extracting the size from the fabric with petrol ether. These application weights were used as reference data for chemometric calibration models.

Hyperspectral camera and chemical imaging A NIR hyperspectral camera system KUSTA1.9MSI (LLA Instruments GmbH, Berlin, Germany) was employed for recording NIR spectra. The NIR camera was installed above a conveyor with a black polyurethane belt with a width of 500 mm (Axmann Fördersysteme GmbH, Zwenkau, Germany). The sensor of the camera is based on an InGaAs photodiode array (192 x 96 pixels) with Peltier cooling. It covers a spectral range from 1320 – 1900 nm. A NIR objective F2.0/15 mm purchased from Specim (Oulu, Finland) was used for imaging. The line speed of the conveyer belt was set to 10 m min^{-1}. With this setup, a lateral resolution of 2.6 mm per pixel is achieved. Further details about the measuring system are described in [15].

The partial least squares (PLS) algorithm was employed for chemometric calculations. The software package KustaSpec 16.6.3 was provided by the manufacturer of the camera system. Details about the creation of the specific PLS model are described in the Results and Discussion section. Chemical images were generated on the basis of the NIR spectra by applying the optimized PLS model.

3 Results

As it was mentioned in the Introduction section, the control of the impregnation or washing steps in textile industry is usually done by gravimetric determination of the application weight or by extraction of the agents from the textile, respectively. Both procedures are laborious and cost intensive. Therefore, there is great interest in an alternative process control method, which is easier, faster, cheaper and which can be used in-line. NIR spectroscopy in combination with chemometric approaches usually fulfills these requirements with respect to fast and powerful in-line measurements of various parameters of interest. However, the prediction of the application weight of size on polyester fabrics by NIR hyperspectral imaging was expected to be a very challenging task, since the absorbance of NIR light by the fabric is commonly much stronger than that of the size. Thus, this paper presents a preliminary study on the determination of the application weight of size by NIR hyperspectral imaging. Results of a more comprehensive study of the determination of the application weight of e.g. several auxiliary agents by NIR hyperspectral imaging will be published elsewhere.

Samples were prepared by padding polyester fabrics in size solution in a foulard. In a second step, some of the sized samples were washed in a desizing solution also in the foulard. After drying, application weights of both sized and desized fabrics were determined by an analytical laboratory. The application weight of the sized and the washed fabrics were determined to be ~19 g m^{-2} and ~2 g m^{-2}, respectively. For spectroscopic investigations, approximately 26000 NIR spectra per sample were collected with a NIR hyperspectral camera. Subsequently, the samples were divided into 10 rectangular regions by defining a grid of 5 columns x 2 rows. The spectra in each rectangle (~ 2600) were averaged. This procedure resulted in 10 averaged spectra that were assigned to the application weight of the sample. In this way, an unintended but unavoidable variation of the size on the fabric is included in the calibration, which leads to a more stable PLS model than without inclusion of the variance. The PLS model was calculated on the basis of the test set calibration method. Samples were split into two independent sets, a calibration set and an internal test set. In order to optimize the PLS model, different preprocessing methods were applied to the spectral data such as baseline correction, differentiation

or normalization. For further processing, a PLS model with a high coefficient of determination (0.94) and a low root mean square error of prediction (RMSEP) of 1.3 g m^{-2} was chosen. This model was based on baseline corrected spectral data, and the spectral range was limited to 1325–1841 nm. The optimum number of eigenvectors was found to be three.

The prediction power of the PLS calibration model was tested with independent test samples, which were prepared in analogy to the calibration samples. The application weight of the size was predicted from the NIR spectra using the PLS calibration. All values of the predicted application weight (26000) of each sample were averaged. Data obtained by the PLS model and the application weights determined by the external laboratory were compared. Results are shown in Tab. 15.1.

Table 15.1: Comparison of the application weights determined by an external laboratory and the values of the application weight predicted by the PLS model

Sample	State of the fabric	Reference data [g m^{-2}]	Predicted application weight from NIR [g m^{-2}]	Difference [g m^{-2}]
1	sized	18.9	18.1	-0.8
2	sized	18.9	18.5	-0.4
3	desized	2.0	2.4	0.4
4	desized	2.0	2.6	0.6

It is obvious that the predicted values and the reference data of the application weight show a close correlation. This result clearly demonstrates the feasibility of the determination of the application weight of the size on sized or desized polyester fabrics by NIR hyperspectral imaging in combination with powerful chemometric models. Chemical images of two samples (one sized and one desized polyester fabric) were calculated on the basis of the NIR spectra by applying the PLS model. In Fig. 1.1 and 1.2 the chemical images of the two fabrics are presented.

A homogenous distribution of the size on the fabric can be easily observed in the chemical images of the sample. Monitoring of the spatial distribution of a parameter of interest such as the local concentration

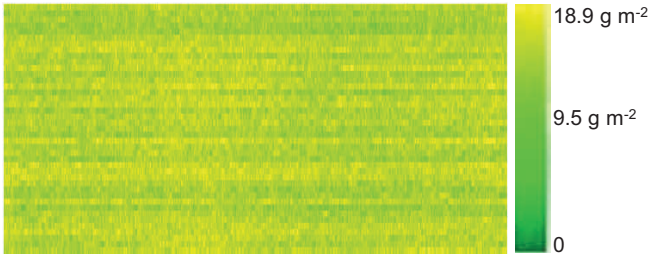

Figure 15.1: Chemical image of a polyester fabric before washing off the size. The application weight of the size was determined to be $\sim$ 19 g m^{-2}.

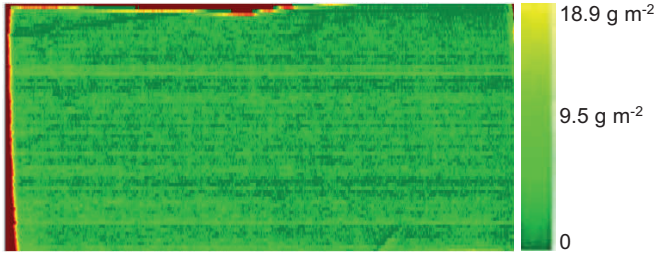

Figure 15.2: Chemical image of a polyester fabric after washing off the size. The remaining application weight of the size was determined $\sim$ 2 g m^{-2}.

of sizes or other finishing agents is a great milestone for the textile industry. Up to now, off-line process control methods, e.g. extraction of the substances, provide only punctual, time-delayed as well as cost intensive results. Thus, using NIR hyperspectral cameras in combination with powerful PLS models provides a powerful tool for in-line process control in textile industry.

Nevertheless, NIR hyperspectral imaging does not only enable the monitoring of the spatial distribution of an auxiliary agent etc., but allows also – after a specific calibration procedure – the detection of impurities on the fabric. Fig.1.3 presents an example of a fabric contaminated with blots of an auxiliary agent dripped to the washed and

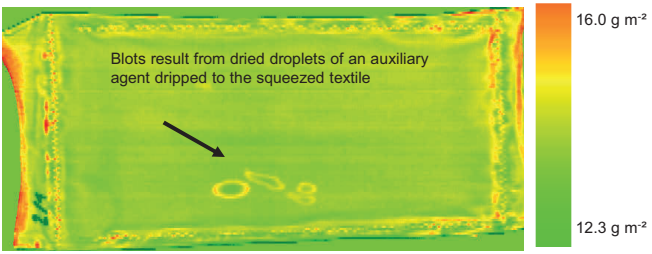

Figure 15.3: Contaminations on a dried fabric. Blots of a colorless auxiliary agent may affect further processing of the textile, e.g. finishing or lamination.

squeezed textile web.The blots are not visible to the eyes, that is, the fabrics show a homogenous surface. NIR hyperspectral imaging for process control enables fast as well as spatially resolved detection of impurities or inhomogeneity on the textile web. Thus, contaminants may be detected efficiently. In this way, waste or products with insufficient quality will be reduced or avoided.

4 Summary

In this study, it was demonstrated that parameters such as the application weight or the distribution of impurities can be visualized with high precision by NIR chemical imaging. In this way, in-line monitoring using NIR hyperspectral cameras has a great potential to open up a new area of process control in textile industry, but also in other branches.

Acknowledgement

The authors thanks the Arbeitsgemeinschaft industrieller Forschungsvereinigungen “Otto von Guericke” (AiF, Berlin, Germany) for financial support under grant no. KF 207 4011 KM3. Futhermore, we would like to thank Marcel Bäuml for the preparation of the samples.

References

1. H. W. Siesler, Y. Ozaki, S. Kawata, and H. M. Heise, Eds., *Near-Infrared Spectroscopy: Principles, Instruments, Application*, Wiley-VCH, Weinheim, 2002.
2. D. A. Burns and E. W. Ciurczak, Eds., *Handbook of Near-Infrared Analysis*, 3rd ed., CRC Press, Boca Raton, 2008.
3. P. C. Williams and K. Norris, Eds., *Near-Infrared Technology in the Agricultural and Food Industries*, 2nd ed., Am. Assoc. of Cereal Chemists, St.Paul/MN, 2001.
4. G. Mirschel, K. Heymann, and T. Scherzer, "Simultaneous In-Line Monitoring of the Conversion and the Coating Thickness in UV-Cured Acrylate Coatings by Near-Infrared Reflection Spectroscopy," *ANALYTICAL CHEMISTRY*, vol. 82, no. 19, pp. 8088–8094, OCT 1 2010.
5. D. L. Chicoma, C. Sayer, and R. Giudici, "In-Line Monitoring of Particle Size during Emulsion Polymerization under Different Operational Conditions using NIR Spectroscopy," *MACROMOLECULAR REACTION ENGINEERING*, vol. 5, no. 3-4, pp. 150–162, APR 13 2011.
6. J. Simpson, S. Staunton, and M. O'Shea, "A review of NIR applications for process control purposes," *INTERNATIONAL SUGAR JOURNAL*, vol. 114, no. 1358, pp. 99–103, FEB 2012.
7. H. Martens and T. Næs, *Multivariate Calibration*, John Wiley and Sons, Chichester, 1989.
8. D. Wu and D.-W. Sun, "Advanced applications of hyperspectral imaging technology for food quality and safety analysis and assessment: A review - Part I: Fundamentals," *INNOVATIVE FOOD SCIENCE & EMERGING TECHNOLOGIES*, vol. 19, pp. 1–14, JUL 2013.
9. A. A. Gowen, C. P. O'Donnell, P. J. Cullen, G. Downey, and J. M. Frias, "Hyperspectral imaging - an emerging process analytical tool for food quality and safety control," *TRENDS IN FOOD SCIENCE & TECHNOLOGY*, vol. 18, no. 12, pp. 590–598, 2007.
10. C. Gendrin, Y. Roggo, and C. Collet, "Pharmaceutical applications of vibrational chemical imaging and chemometrics: A review," *JOURNAL OF PHARMACEUTICAL AND BIOMEDICAL ANALYSIS*, vol. 48, no. 3, pp. 533–553, NOV 4 2008.
11. A. Kulcke, C. Gurschler, G. Spock, R. Leitner, and M. Kraft, "On-line classification of synthetic polymers using near infrared spectral imaging," *JOURNAL OF NEAR INFRARED SPECTROSCOPY*, vol. 11, no. 1, pp. 71–81, 2003.

12. S. Gosh and J. Rodgers, "NIR analysis of textiles," in *Hanbook of Near-Infrared Analysis*, CRC Press, Boca Raton, 2008.
13. M. Blanco, J. Coello, H. Iturriaga, S. Maspoch, and J. Pages, "Use of near-infrared spectrometry in control analyses of acrylic fibre manufacturing processes," *ANALYTICA CHIMICA ACTA*, vol. 383, no. 3, pp. 291–298, MAR 15 1999.
14. M. Blanco, J. Coello, J. Fraga, H. Iturriaga, S. Maspoch, and J. Pages, "Determination of finishing oils in acrylic fibres by near-infrared reflectance spectrometry," *ANALYST*, vol. 122, no. 8, pp. 777–781, AUG 1997.
15. G. Mirschel, O. Daikos, T. Scherzer, and C. Steckert, "Near-infrared chemical imaging used for in-line analysis of inside adhesive layers in textile laminates," *ANALYTICA CHIMICA ACTA*, vol. 932, pp. 69–79, AUG 17 2016.

Infrared spectral imaging for damage detection and prevention of overhead power lines

Gabriela Molinar and Wilhelm Stork

Karlsruhe Institute of Technology,
Institute for Information Processing Technologies,
Engesserstraße 5, 76131 Karlsruhe, Germany

Abstract A proposal for an overhead line monitoring system using infrared imaging is presented as a thermal characterization of a target far from the imaging sensor. The thermal image is used to measure the clearance from conductor to ground, which allows the transmission system operators to regulate the power transmission to prevent possible dangerous events. If the line is too elongated due to high temperatures, the possibility of electrical sparks with objects near the line increases. Additionally, this system can detect hot spots in the connectors and ice loads over the line if the position of the field of view is changed. The design of this system is described in detail, as well as some simulations and experimental results are shown to illustrate the capabilities of the proposed system.

Keywords: Overhead line monitoring system, infrared camera, clearance measurement, hot spot, ice detection.

1 Introduction

Electricity has become a basic need for the modern society and the electric network is used to transport it from power plants to consumers. This medium must be safe and employed in an efficient way for economic reasons. Therefore the transmission system operators (TSO) use monitoring systems to maintain the state of the transmission lines under supervision. Using sensors and optimal control, the capacity of the existent network can be increased up to 20 % [2], reducing the need to construct new lines [3]. Moreover, these monitoring systems help

prevent premature conductor aging due to high temperatures or an electrical discharge with objects below or near the line (clearance to ground too low).

The state-of-the-art of overhead line monitoring systems (OLMS) shows different ways to measure the conductor parameters: Indirect methods, which use only weather data to estimate the conductor temperature, or direct methods, which include sensors installed on the lines, suffering from electromagnetic interference and lacking of energy due to the need to use induction from the line as power source [2, 4]. This paper proposes a new idea for the OLMS, to overcome the inaccuracy of the indirect methods and the problems of sensors installed on a high voltage line: the use of an infrared camera installed on the transmission tower and a passive target attached to the conductor.

The IR-camera will be installed pointing to the target, which must have high thermal conductivity to follow the conductor temperature along time. The target must also have a high emissivity in order to be visible for the camera and to increase the accuracy of the temperature measurement. Based on these conditions, the material and geometry of the target as well as the camera selection are discussed in this paper.

In section 2 the thermal behavior of the overhead lines and its relationship with the elongation of the conductor is explained. In section 3 the proposed design is described in detail and the criteria for the selection of a target and a camera are discussed. Moreover, some simulations and experimental results are shown in section 4 to illustrate the capabilities of the proposed system.

2 Decrease of clearance for high conductor temperatures

The conductor temperature increases proportional to the current square value but also depends on ambient factors as eq. 16.1 shows [2, 5]. The conductor heat losses are on the left side of this equation: convection q_c, which depends on the wind speed and direction; radiation q_r, whose value depends on the emissivity ϵ of the conductor; and the conductor heat storage, where C_p is the heat capacity of the conductor material and m the mass per unit length of the conductor.

The heat gains are on the right side of eq. 16.1: solar radiation q_s and the ohmic heat gain depending on the current flowing through the line and its temperature dependent resistance.

$$q_c + q_r + mC_p \frac{dT_{avg}}{dt} = q_s + I^2 R(T_{avg}) \tag{16.1}$$

The convection heat loss is the greatest term in eq. 16.1. This means that the wind plays an important role in the value of the conductor temperature. The wind direction and velocity normally changes along the line, i.e. a homogeneous conductor temperature cannot be expected. To illustrate this, the study made in [6] demonstrates how a punctual temperature measurement can deviate from the mean conductor temperature. This demonstration was done using punctual temperature sensors installed at several points of a line during a period of 12 hours. The result was a deviation of around $\pm 40^{\circ}$C from the mean conductor temperature value [6]. This means that a single point temperature measurement cannot represent the temperature of the whole line.

On the other hand, as the conductor temperature increases so does its length. The relationship between them is linear and is shown in eq. 16.2 [7]. The constant α is the thermal expansion coefficient of the material and means how easy the conductor elongates for a change of 1K from the reference temperature $T_{c,ref}$. Greater values of α correspond to more elongation of the conductor from the same reference length L_{ref}.

$$L = L_{ref}(1 + \alpha(T_c - T_{c,ref})) \tag{16.2}$$

If the conductor length increases, the clearance from the line to ground decreases. The distance from the span (S, straight line between connectors) and the minimum point of the conductor curve is called the sag D. The sag plus the clearance to ground corresponds to the total height of the conductor connectors The relationship between sag and conductor temperature is shown in the eq. 16.3 [7] as an approximated version only valid for level spans (both poles are at the same height).

$$D \approx \sqrt{\frac{3S}{8}[L_{ref}(1 + \alpha(T_c - T_{c,ref})) - S]} \tag{16.3}$$

As an example, the sag of an ACSR Drake 403 mm^2 26/7 with 300m of span in the temperature range from -15°C to 80°C goes from 6.4 m to

9.1 m, that means a change of 2.7 m. The conductor length, on the other hand, increases 30 cm in the same temperature range. This increment in length could mean a dangerous situation for a transmission line and its surroundings, depending on the line case and weather conditions.

3 Concept description

This article proposes a new design for OLMS: Infrared imaging for a remotely detection and characterization of a target to determine the elongation of a transmission line in real time. Ice load and hot spots detection can also be derived from the same infrared image. Knowing the ambient temperature as well as the clearance to ground, ice loads can be estimated [8]. On the other hand, hot spots on the connections between conductor and insulator can also be detected using servomotors to change remotely its point of view: from the target to the line connections and vice versa. Hot spots are produced by damages on the conductor connectors. They mean loss of energy through heating and a fast detection of them avoids a break of the line [9]. With this system the TSOs can perform remotely manual checks of the line connections when considered appropriate, using the sensor unit already installed.

The camera is mounted on the transmission tower, therefore the need to power-off the line for installation is completely eliminated (normally a disadvantage of state-of-the-art systems with electrical sensors directly installed on the line). The passive target can be hanged on the overhead line using a hot stick, which reduces the system installation time. These advantages, the fact that there is just one sensor installed on the tower to measure clearance, ice loads and hot spots and the possibility to calculate the conductor temperature (if the current is known[1]), make this system a competitive solution compared to the state-of-the-art overhead line monitoring systems.

Clearance measurement can be done through the detection of the position of the target from the images produced by the IR camera. Since the target is following the conductor temperature, which is normally well above ambient temperature, the target can be seen by the IR-camera even at night without the need of extra-illumination. The

[1] A current sensor can be also installed in the tower if the TSO is not able to give a real-time current value.

advantage of using a target hanged on the line is the increment of the detection area from the conductor diameter (0.5 to 5 cm for Aluminum Conductor Steel Reinforced (ACSR)) to the target diameter, reducing the required resolution of the camera, i.e. reducing costs.

3.1 Target design

To design the target several parameters must be considered:

- High thermal conductivity: to maintain the target at a higher temperature than the surrounding ambient.
- High emissivity: To allow the detection of the target by the IR imaging device.
- Type of the line: Single conductor or a bundle.
- Low cost and weight.

The architecture proposed for the target is shown in figures 16.1 and 16.2. On the left side there is a target for the case of a single conductor and at the right side the quad-bundle[2]. In both cases they have a circular and symmetric form.

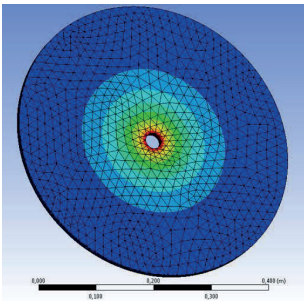

Figure 16.1: Target design for the single conductor case.

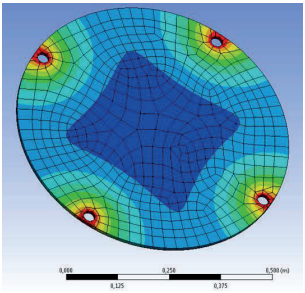

Figure 16.2: Target design for the quad-bundle case.

[2] In practice there are also bundles of two or three conductors, but for simplicity is only considered the four conductors bundle (quad-bundle).

The materials with highest thermal conductivity are the diamond and the copper. To keep the costs as low as possible, copper is the best option to construct the target (with a thermal conductivity of 400 W/m°C and a cost of around 4.2 Euro/kg). The disadvantage of it is its low emissivity (high reflectivity instead), i.e. for an infrared camera it will be invisible as long as it is not reflecting any IR-light coming from other objects. In this case a high emissivity coating like the offered by the company Aremco [10] can be used to cover it completely.

To determine the size of the quad-bundle target, the fact that normally the distance between conductors is 45 cm must be considered. In that case and supposing 3 cm for the conductor diameter, then the target diameter should be at least 68 cm. To reduce weight a meshed inner structure is proposed.

3.2 Camera selection

To select a appropriate camera the following criteria must be considered:

- Operating wavelength: Since normally the temperature of the conductor cannot exceed 80°C, the target temperature will be always below that value and then the imaging device can work in the long wavelength infrared range (LWIR, from 8 to 14 μm).
- Cooled or uncooled camera: Since the imaging in this system should work in the LWIR range, to reduce costs and energy consumption an uncooled camera is chosen.
- Number of pixels: The resolution of the clearance measurement depends on this parameter. The number of pixels should be enough to have at least a pixel for a change of sag of 2 cm (equivalent to approximately $\Delta T = 1°C$). To cover 3 m of change in clearance with this resolution, at least 150 pixels are needed in the vertical direction.
- Field of view (FOV): Since the target will be at a distance around 100 m to 150 m from the camera, the FOV must be narrow enough to have the target covering the most part of the image. For 150 m a FOV of 5°, for 100 m a FOV of 7° (considering a camera of 640x480 pixels and a resolution of 2cm per pixel).

4 Simulations and experiments

The thermal behavior of the target was simulated using the simulation software ANSYS. A conductor temperature was specified as the boundary condition of the target holes where the overhead line should be placed. The graphs in figures 16.3 and 16.4 show how the quad-bundle target follows the conductor temperature in the natural and forced convection cases[3], respectively. In both cases the ambient temperature was fixed at 22°C and the beginning temperature of the target is 50°C.

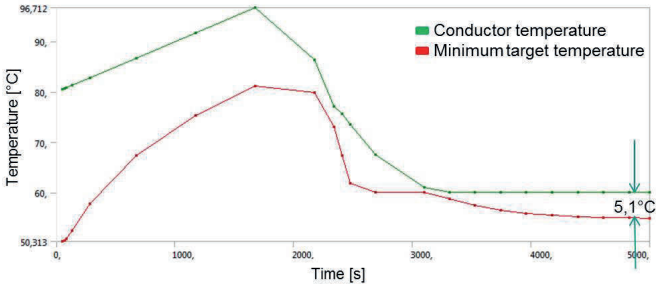

Figure 16.3: Natural convection of the quad-bundle target.

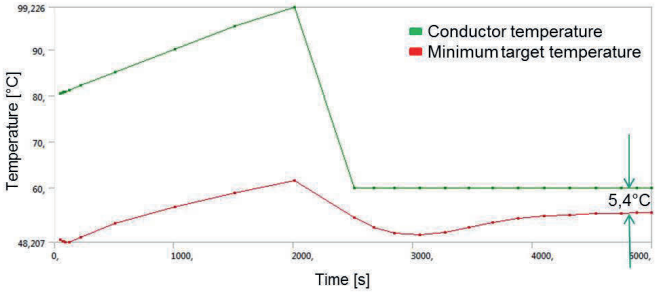

Figure 16.4: Forced convection of the quad-bundle target.

[3] Natural convection means almost no wind (less than 0.5 m/s) and forced convection corresponds to an effective wind velocity of 0.5 m/s or more [5].

In the natural convection case the target is able to follow better the conductor temperature as in the forced convection case. This is due to the fact that the target transfers more heat to the ambient because of forced convection. This result says that the camera will not be able to measure most of the time an accurate conductor temperature, because the target will not have a homogeneous temperature as long as the conductor temperature and the ambient conditions are changing. However, the goal of this system is not to measure temperature but to do a target recognition from an infrared image and hence to determine the clearance from the transmission line to ground. The achievement of this is possible as long as the mean target temperature is higher than the ambient temperature, which will happen providing that the conductor is under electrical load.

The automatic recognition of the target hanging from the conductor and its position measurement is made using image processing applied to the captured infrared data. As a general idea, the program should recognize the circular form of the target and return important parameters as the center of the circle and its radius. Using this information and knowing the camera parameters (FOV, number of pixels) as well as the distance camera to target, the distance from conductor to ground can be calculated.

A first version of the image processing program for this application was done making use of Matlab. Using this high level approach the capabilities of target detection algorithms can be tested. After that the algorithm can be programmed to be executed by the embedded system used in the overhead line monitoring system (a microcontroller, a DSP or a FPGA, for example).

The algorithm used to acquire the following results is based on the circular Hough transform [11]. Several images of a hot target (around 60°C) at different positions to the camera were captured with an infrared camera FLIR A655sc with a 24,6 mm lens (FOV: 25°×19°) and 640×480 pixels.

From the captured images and knowing the radius of the target (7 cm) the distance from the camera to the target was calculated by the software and compared to the distance measured by hand. The manual measurement had a precision of 5 mm and the distance target to camera was between 1.17 m and 1.19 m at each image. The mean error obtained was 9.4 mm between calculated and measured distance,

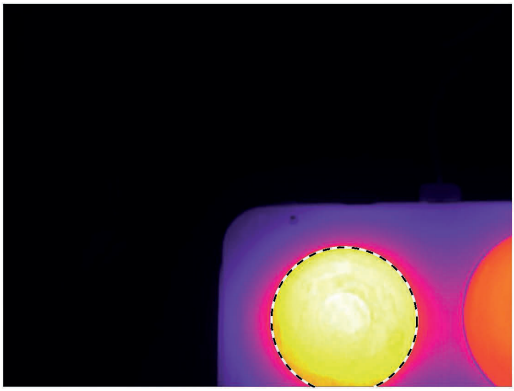

Figure 16.5: Target partially outside of the camera FOV and still recognized by the circular hough transform programmed in Matlab.

which corresponds to a 0.8 % of error. This result is considered interesting because this error includes a target partially outside of the camera FOV, which was still recognized by the software (see figure 16.5).

5 Summary

In this article a new approach for overhead line monitoring systems was presented: the use of an infrared camera to measure the clearance of the transmission line to ground, by detecting a target hanged on the conductor. With the results obtained was shown that the implementation and use of the proposed system is possible. The next step is the implementation of the idea on overhead lines, which implies new challenges as harsh weather conditions and the proximity to high voltage conductors.

References

1. M. Vollmer, "Infrared thermal imaging: fundamentals, research and applications," Weinheim, 2010.

2. D. Douglas, W. Chisholm *et al.*, "Real-time overhead transmission-line monitoring for dynamic rating," *IEEE Transactions on Power Delivery*, vol. 31, no. 3, pp. 921–927, Dec. 2016.
3. Tennet, "Netzausbau in Niederbayern: Stromversorgung zwischen Bayern und Österreich," Deutschland, Apr. 2015.
4. R. Stephen, "Real time monitoring," *Electra*, vol. 197, Aug. 2001.
5. Cigré, "Thermal behaviour of overhead conductors," Cigré, techreport 207, Aug. 2002.
6. G. Biedenbach, "Echtzeitmonitoring von Freileitungen: Leiterseiltemperatur zuverlässig ermitteln." *EW Magazin für die Energiewirtschaft*, vol. 7104, pp. 70–73, 2012.
7. Cigré, "Sag-tension calculation methods for overhead lines," Cigré, techreport 324, Apr. 2016.
8. G. Biedenbach, "Kapazitäten in Stromnetzen Optimal Ausschöpfen. Monitoring macht den Betrieb von Freileitungen sicherer." *EW Magazin für die Energiewirtschaft*, pp. 74–83, 2009.
9. J. Frate, D. Gagnon *et al.*, "Evaluation of overhead line and joint performance with high-definition thermography," in *Transmission and Distribution Construction, Operation and Live-Line Maintenance Proceedings*. IEEE, Oct. 2000.
10. Aremco, "High temperature high emissivity coatings," URL, 2016. [Online]. Available: http://www.aremco.com/high-emissivity-coatings/
11. B. Jähne, "Digitale Bildverarbeitung und Bildgewinnung," Berlin, Heidelberg, 2012. [Online]. Available: http://swbplus.bsz-bw.de/bsz377583960cov.htm

Analysis of plant raw materials and extracts applying various vibrational spectroscopy techniques – possibilities and limitations

Hartwig Schulz, Gennadi Gudi and Andrea Krähmer

Julius Kühn-Institute (JKI)
Institute for Ecological Chemistry
Plant Analysis and Stored Product Protection
Königin-Luise-Strasse 19
D-14195 Berlin-Dahlem, Germany
Email: Hartwig.Schulz@julius-kuehn.de

Abstract New methods using MIR, NIR and Raman spectroscopy in combination with various chemometric algorithms are presented which allow monitoring numerous plant samples very efficiently within a short time. Today portable FT-IR spectrometers are available which only need sample amounts of a few microliters or milligrams. In most cases, the measurements can be performed directly and non-destructively on the individual plant tissues or plant extracts. Generally, with IR and Raman spectroscopic techniques spectra are obtained which present characteristic key bands of individual plant components. These bands provide important information about the chemical composition of the investigated samples. Based on such markers spectroscopic analyses in principle allow the discrimination of different species, and even to classify chemotypes among the same species. Combination of vibrational spectroscopy and hierarchical cluster analysis provides a fast, easy and reliable method for chemotaxonomic characterization. The ability to rapidly monitor various plant components makes it possible to efficiently select high-quality single plants from wild populations as well as progenies of crossing experiments. Furthermore, the vibrational spectroscopic methods can also be used by the processing industry in order to perform fast quality checks of incoming raw materials as well as continuous controlling of production processes.

Keywords: NIRS, Raman, ATR-IR, chemometrics, quality control, in-process control, plant, breeding, cultivation.

1 Introduction

Quality control of cultivated plant species as well as products derived from them usually comprises correct botanical identification of the plant material as well as quantification of the individual active principles. Furthermore, residues (e.g. organic solvents) and contaminants (e.g. pesticides and heavy metals) are determined applying various sophisticated analytical techniques. For this, testing of plant material such as phytopharmaceutical products is usually performed in accordance with validated standard methods described in the Food Chemical Codex, the European Pharmacopeia, the United States Pharmacopoeia and others. Contrary to this approach, there is some need to apply also various rapid high-throughput methods aiming to characterise simultaneously several quality parameters and to reduce efforts for sample preparation to a minimum. In this context new vibrational spectroscopy methods (MIR, NIR and Raman spectroscopy) in combination with various chemometric algorithms are presented which allow efficient monitoring of numerous plant samples within a short time. Especially Raman spectroscopy has been found to be a reliable and non-destructive method for rapid discrimination of different plant species or chemotypes if characteristic key bands can be observed in the spectrum. But also NIR and ATR-IR spectroscopy have made the handling of powdered as well as liquid samples very quick and simple. Today portable IR and Raman spectrometer systems are available which only need sample amounts of a few microliters or milligrams for analysis. In most cases, vibrational measurements can be performed directly on plant tissues as well as on fractions isolated from the plant material by hydro-distillation or solvent extraction. Based on individual marker bands, spectroscopic analyses in principle allow the discrimination of different species, and even to classify chemotypes among the same species. Combination of vibrational spectroscopy and hierarchical cluster analysis provides a fast, easy and reliable method for chemotaxonomic characterization. The ability to rapidly monitor various plant components provides the possibility to efficiently select high-quality

single plants from wild populations as well as progenies of crossing experiments. Today, vibrational spectroscopy is already introduced in industry in order to perform fast quality checks of incoming raw materials and continuous controlling of production processes.

This review presents an overview of some selected applications for NIR, ATR-IR and Raman spectroscopy useful to characterize plant raw materials and extracts produced therefrom.

2 Proteins and amino acids

Several Raman vibrational modes support the interpretation of various amino acids and proteins occurring in plant tissue. In this context, the following three signals are of main interest for the identification of different protein backbone confirmations: amide I to be detected between 1680–1600 cm^{-1} (stretching vibration of C=O), amide II observed in the range between 1580 and 1480 cm^{-1} and amide III to be found between 1300 and 1230 cm^{-1} (both associated with coupled C-N stretching and N-H bending vibrations of the peptide group). Also IR spectroscopy was successfully applied to investigate amino acids and proteins in the plant material as for instance to analyze the distribution of lysine in barley [1].

Applying Raman microspectroscopy the individual content of protein in wheat kernels was measured with high spatial resolution [2]. Specific amino acid structure elements such as S-S and S-H groups of cystine and cysteine, aromatic rings of tryptophan, tyrosine and phenylalanine and the imidazole ring of histidine also provide helpful information for a reliable interpretation of the registered Raman and IR spectra. Identification of compounds containing disulfide bonds can be successfully obtained by using FT-Raman spectroscopy, because the S-S stretching band is polarized and very prominent in the Raman spectra while the IR intensity is usually week due to its nonpolar nature [3]. Also sulfhydryl groups show comparatively strong S-H stretching modes in the Raman spectrum which occur in the region between 2550 and 2580 cm^{-1}.

3 Lipids and fatty acids

Applying discriminant analysis (DA) and principal component analysis (PCA) it has been shown that commercial vegetable oils such as extra virgin olive oil, groundnut oil, corn oil, grape seed oil, olive oil, rape seed oil, sunflower oil, and walnut oil can be properly identified. Furthermore, it has been found that the frequency of concrete absorption bands in the fingerprint region (700–1500 cm^{-1}) provides direct information about the ratio between saturated and cis monounsaturated fatty acid acyl groups. Stretching vibrations of trans and cis olefinic double bonds have been observed around 3025 and 3006 cm^{-1}, respectively. Beside C-H stretching vibrations between 3000 and 2850 cm^{-1}, the C=O group of triglycerides shows strongest absorption bands at approx. 1746 cm^{-1} [4]. A partial least squares (PLS) calibration model for the prediction of the peroxide value was developed based on spectral information in the range between 3750-3150 cm^{-1} which exhibits the characteristic hydroperoxide absorption bands, centered at 3444 cm^{-1} [5]. The reproducibility of this FTIR method was found to be more reliable than the usually applied chemical titration method.

The intensities of Raman bands near 1660 cm^{-1} and 1670 cm^{-1} have been assigned to the individual cis and trans isomer contents, present in various edible oils [6]. It has been also reported that the ratio of scattering intensity arising from the C=C stretching vibration (1600 cm^{-1}) to that obtained from the CH2 scissoring mode (1444 cm^{-1}) was used to reliably predict the iodine values of triglycerols and unconjugated vegetable oils. These Raman measurements are extremely useful for quality control purposes in the food industry, particularly the option to perform remote on-line control measurements through optical fibers to monitor simultaneously the degree of unsaturation and isomer formation during hydrogenation processes of edible oils.

Raman spectroscopy has been also applied to study the arrangement of the acylglycerol molecules, which leads to different melting behavior and other properties of oils. Especially the C-H stretching region (signals at 2850 cm^{-1} and 2885 cm^{-1}) in the Raman spectrum provides valuable information on the environment of hydrocarbon chains in lipids due to different liquid-crystalline lipid-water phases [7].

4 Carbohydrates

Most FT Raman spectra obtained from measurements of various mono-, di-, oligo- and polysaccharides show characteristic bands which can be used for discrimination purposes. The spectrum of sucrose presents the characteristic bands of α-glucose (847 cm^{-1}) and β-fructose (868 cm^{-1}); in the spectrum of maltose besides α-glucose signals the band due to β-glucose (898 cm^{-1}) can be seen, whereas cellobiose shows only a signal at 885 cm^{-1} representative for the β-anomer. Distinctive bands at 1462 cm^{-1}, 1126 cm^{-1}, 840 cm^{-1}, due to sugar vibrational modes, can be used to determine the distribution of these components in various plant tissues such as carrot roots [8]. ATR-IR spectroscopy combined with PLS algorithm allows the quantification of the three main monosaccharides (glucose, maltose and fructose) in glucose syrups [9]. Furthermore, infrared spectroscopy has been successfully applied for monitoring wine fermentation. A reliable PLS calibration model was developed and proved to be effective for analyzing cv. Cabernet Sauvignon for e.g. glucose and fructose content [10].

Generally, FT Raman spectroscopy was found to be a powerful tool for investigation of higher plant cell walls and their components providing complementary information to that obtained by FT-IR microspectrometry [11].

Amylose and amylopectin can be also successfully analyzed by application of Raman spectroscopy. It has been reported that the structural differences of both starch materials can be detected in the C-H stretching region between 2700 and 3100 cm^{-1} [12].

5 Phenolic substances

Most studied plant secondary metabolites are flavonoids, which show a wide distribution in each part of vascular plants. Here, individual flavonoid types can be modified by hydroxylation, methylation, acylation, and glycosylation.

Anthocyanins belong to the most important group of plant pigments that are visible to human eyes. In general, their concentration in most fruits and vegetables varies between 0.1 and 1 g/100g dry matter. Resonance Raman (RR) spectroscopy has been applied to determine the

influence of glycosylation on the benzopyrylium part of the flavonoid molecule, and provided some characteristic spectral features of these phenomena [13,14]. In this context, characteristic spectral features were observed in the spectral range between 500 and 900 cm^{-1}. When the C(5) position of the anthocyanin molecule is glycosylated, significant perturbations of spectral features between 640 and 750 cm^{-1} are visible, but they depend also on the nature of the individual sugar. Resonance Raman spectra obtained directly from vacuoles of the skin of cv. Pinot noir wine berries (Vitis vinifera) showed that its main pigment is malvidin 3-glucoside, which occurs in the quinonoidal base form inside the skin whereas in the outer face of the skin it is mainly present in the flavylium form [15]. In the epidermis of petals of the common mallow (Malva sylvestris), only malvidin 3,5-diglucoside has been detected, entirely in the cationic flavylium form [15].

Several phenolic compounds biosynthesized in the phenylpropane pathway such as anethole, eugenol, carvacrol, and thymol, have been identified as major essential oil components. They are widely used in the production of perfumes, flavorings and phytopharmaceuticals or as additives for pet food relating to their antibiotic properties.

Both IR and Raman spectroscopies allow identifying these substances. They demonstrate strong IR bands due to C-H wagging vibration between 800 and 920 cm^{-1}, whereas in the FT-Raman spectrum ring deformation vibration is observed between 740 and 760 cm^{-1} [16–18]. Significant differences are seen for isomeric compounds like thymol /carvacrol in FT-Raman as well as in ATR-IR spectra. In FT-Raman spectra ring vibration of thymol is seen at 740 cm^{-1}, while for carvacrol this signal is shifted to 760 cm^{-1}. In the ATR-IR spectrum the most intense bands are seen at 804 cm^{-1} (thymol) and 811 cm^{-1} (carvacrol) [16,17].

FT-Raman spectroscopy was also used for investigation of curcumin, which is a valuable dyeing component of curcuma root (Curcuma sativa). The most intense bands appearing at 1630 and 1601 cm^{-1} can be assigned to the benzene ring, whereas bands at 1185 and 965 cm^{-1} are due to COC and COH vibrations [19]. The presence of characteristic curcumin bands in the spectrum of curcuma roots provide very good pre-conditions to apply selective Raman maps in order to determine the curcumin distribution in a sprouting curcuma root [20].

6 Terpenoids

Terpenes occurring in flowers, stems, leaves, and roots of numerous plant species are frequently used in perfume compositions as well as in flavours of food-stuffs or mouth care products. For numerous essential oil plants such as basil (Ocimum basilicum) [21], fennel (Foeniculum vulgare) [20, 22], oregano (Origanum vulgaris), thyme (Thymus vulgaris) [16–18, 23–25], marjoram (Origanum majorama) [16, 17], pepper (Piper nigrum) [26], chamomile (Chamomilla recutita) [20,23], eucalyptus species [27] and various citrus fruits [28] calibration models have been developed which allow to quantify valuable components and to discriminate different chemotypes.

Acyclic monoterpenes show the most intense bands due to stretching vibrations of C=C bonds at about 1670 cm^{-1} in the Raman spectrum, whereas IR spectra are more miscellaneous. Both, monocyclic and bicyclic terpenes, demonstrate strong IR bands due to C-H wagging vibration between 800 and 920 cm^{-1}, however by using Raman spectroscopy differentiation between these groups is more clear. Ring deformation vibration observed in the FT-Raman spectrum of monocycles between 740 and 760 cm^{-1}, in the case of bicycles is shifted about hundred to lower wavenumbers and can be therefore recognized in the range between 645 and 666 cm^{-1} [16–18]. Significant differences are seen for structural isomers like α-terpinene/γ-terpinene in FT-Raman as well as in ATR-IR spectra. In the FT-Raman spectrum characteristic C=C stretching vibrations appear at 1611 cm^{-1} for α-terpinene and at 1701 cm^{-1} for γ-terpinene reflecting the difference between a conjugated and a nonconjugated system, respectively.

More than 600 carotenoids have been found in plants, but only α, β and a few other carotenes (not lycopene and lutein) can be converted into vitamin A by human beings. Although these natural pigments occur in plants as minor components at the ppm level a very sensitive detection can be achieved by Resonance Raman in the visible region, when the wavenumber of the laser excitation coincides with an electronic transition of the individual carotenoid [29, 30]. FT-Raman spectroscopy also gives a strong enhancement of carotenoids due to the known pre-resonance effect; furthermore disturbing fluorescence effect of biological material usually observed when laser excitation is performed in the visible range, is avoided. Strong bands of carotenoids

are observed in the Raman spectrum within the 1500–1550 and 1150–1170 cm^{-1} ranges due to in-phase C=C (v1) and C-C stretching (v2) vibrations of the polyene chain. Additionally, in-plane rocking mode of CH3 groups attached to the polyene chain and coupled with C-C bonds are seen as a peak of medium intensity in the 1000–1020 cm^{-1} region. It has been shown that the wavenumber location of these bands is strongly dependent on the length of the carotenoid chain, and generally, carotenoids with 11, 9, 8, 7 conjugated C=C bonds have their characteristic bands at about 1510, 1524, 1530, 1536 cm^{-1} [31,32].

7 Alkaloids

In spite of the fact that alkaloids show a broad range of different chemical structures only a few vibrational measurements of these plants substances have been published. FT Raman spectra obtained from green berries of pepper (Piper nigrum), ground black pepper and black pepper oleoresin predominantly show significant key signals of piperine [26]. Apart from the intense –C-H stretching vibrations between 2800 and 3100 cm^{-1}, the main Raman signals occur in the fingerprint range between 1100 and 1630 cm^{-1}. On the basis of ATR-IR and Raman measurements chemometric equations have been developed for calibration of piperine content in pepper samples, showing a comparatively high prediction quality [26].

Both, ATR-IR technique and FT Raman spectroscopy have been demonstrated to be very promising tools for fast and reliable determination of the main alkaloids (morphine, codeine, papaverine, thebaine and noscapine) occurring in poppy plant material and related pharmaceutical products [32]. Raman spectra in the fingerprint range between 700 and 1500 cm^{-1} show numerous sharp bands which are mainly assigned to deformation and stretching vibrations of the alkaloid ring system. Raman spectra obtained from poppy milk presents most relevant morphine bands (e.g. peaks at 631, 1620, 1642, 3044 and 3073 cm^{-1}) and aqueous-ethanolic extracts prepared from unripe poppy capsules show several specific peaks which can be assigned to vibrational modes of the mentioned alkaloid substances.

Guarana seeds, which represent an important product of the Amazonian rain forest, were also successfully analyzed by FT Raman spec-

troscopy aiming to determine the individual content of the main alkaloids (caffeine, theophylline and theobromine) [33]. The discrimination between anhydrous caffeine and it's monohydrate form was presented as a key band at 1656 cm^{-1} and it's relative intensity compared to the 1698 cm^{-1} signal, both of which are CO stretching modes. The occurrence of these bands in the Raman spectrum of guarana methanolic extracts confirms that this product contains anhydrous caffeine. Theobromine was distinguished from caffeine and theophylline by the presence of a band at 620 cm^{-1}, whereas the other two alkaloids have a strong feature at 556 cm^{-1} and a medium doublet for caffeine to be seen at 643 and 741 cm^{-1} [33].

8 Polyacetylenes

Generally, polyacetylene spectra show strong and polarized bands, due to the triple bonds in the molecule, in the region around 2200 cm^{-1}. As has been discussed earlier [34], the number of triple bonds as well as substituents influence the frequency of the polyacetylene -C≡C- stretching modes. Thus, the spectral position of -C≡C- vibrations and pattern of Raman bands usually provide enough information to recognize the type of substitution and to support the identification of polyacetylenes [3]. Generally, for compounds containing a -C≡C-C≡C- grouping, the vibrational modes are described as asymmetric and symmetric -C≡C-C≡C- stretching, and accordingly they are IR and Raman active, respectively. The characteristic, strong and polarized, symmetric stretch of the R-C≡C-C≡C-R' structure should be seen in the interval of 2257-2251 cm^{-1} in the Raman spectrum [10].

It has been shown that by using Raman spectroscopy it is possible to distinguish the main polyacetylenes occurring in carrot as well as in ginseng roots. Carrot polyacetylenes possess a similar molecular structure with two adjacent triple bonds substituted with one -OH group (falcarinol) and two –OH groups (falcarindiol) and show their characteristic -C≡C- mode in the Raman spectrum at 2258 and 2252 cm^{-1}, respectively [35,36]. In ginseng roots, beside falcarinol, its epoxy derivative (panaxydol) occurs in higher amounts, and can be characterized by the strong Raman signal at 2260 cm^{-1} [37]. Falcarinol and panaxydol are among the most bioactive polyacetylenes isolated from ginseng

and hence they are very important in relation to their anti-cancer effect and other pharmacological properties of ginseng roots. Furthermore, falcarinol and falcarindiol contribute strongly to the bitter taste of carrot [38,39], but may also have some negative effects when administered in high doses [40].

References

1. "L.G. Thygesen, M.M. Lokke, E. Micklander, S.B. Engelsen, Trends Food Sci. Tech. 14 (2003) 50."
2. "O. Piot, J.C. Autran, M. Manfait, J. Cereal Sci. 32 (2000) 57."
3. "D. Lin-Vien, N.B. Colthup, W.G. Fateley, J.G. Grasselli, The Handbook of Infrared and Raman Characteristic Frequencies of Organic Molecules. Academic Press Inc., San Diego; 1991."
4. "M.D. Guillen, N. Cabo, JAOCS 74 (1997) 1281."
5. "F.R. van de Voort, A.A. Ismail, J. Sedman, G. Emo, JAOCS 71 (1994) 243."
6. "G.F. Bailey, R.J. Horvat, J. Am. Oil Chem. Soc. 49 (1972) 494."
7. "K. Larsson, R.P. Rand, Biochim. Biophys. Acta 326 (1973) 245."
8. "Y. Ozaki, R. Cho, K. Ikegawa, S. Muraishi, K. Kawauchi, Appl. Spectrosc. 46 (1992) 1503."
9. "F. de Lène Mirouze, J.C. Boulou, N. Dupuy, M. Meurens, J.P. Huvenne, P. Legrand, Appl. Spectr. 47 (1993) 1187."
10. "A. Urtubia, J. Ricardo Pérez-Correa, M. Meurens, E. Agosin, Talanta 64 (2004) 778."
11. "C.F.B.Séné, M.C. McCann, R.H.Wilson, R. Grinter, Plant Physiol. 106 (1994) 1623."
12. "B.J. Bulkin, I.C.M. Dea, Y. T. Kwak, Gums and Stabilizers for the Food Industry 3 (eds.: G.O. Phillipps, D.J. Wedlock, P.A. Williams), pp. 485-496, Elsevier."
13. "J.-C. Merlin, A. Statoua, J.-P. Cornard, M. Saidi-Idrissi, R. Brouillard, Phytochemistry 35 (1994) 227."
14. "J.-C. Merlin, J.P. Cornard, Spectrochim. Acta A 50 (1994) 703."
15. "C. Merlin, A. Statoua, R. Brouillard, Phytochemistry 24 (1985) 1575."
16. "M. Baranska, H. Schulz, H. Krüger, R. Quilitzsch, Anal. Bioanal. Chem. 381 (2005) 1241."

17. "D.J. Daferera, P.A. Tarantulis, M.G. Polissiou, J. Agric. Food. Chem. 50 (2002) 5503."
18. "H. Schulz, G. Özkan, M. Baranska, H. Krüger, M. Özcan, Vib. Spectr. 39 (2005) 249."
19. "G.N. Andreev, B. Schrader, H. Schulz, R. Fuchs, S. Popov, N. Handjieva, Fresenius J. Anal. Chem. 371 (2001) 1009."
20. "M. Baranska, H. Schulz, P. Rösch, M.A. Strehle, J. Popp, Analyst 129 (2004) 926."
21. "H. Schulz, B. Schrader, R. Quilitzsch, S. Pfeffer, H. Krüger, J. Agric. Food Chem. 51 (2003) 2475."
22. "M.A. Strehle, P. Rösch, M. Baranska, H. Schulz, J. Popp, Biopolymers 77 (2005) 44."
23. "H. Schulz, R. Quilitzsch, H. Krüger, J. Mol. Struct. 661 (2003) 299."
24. "N.G. Siatis, A.C. Kimbaris, C.S. Pappas, P.A. Tarantilis, D.J. Dafarera, M.G. Polissiou, J. Agric. Food. Chem. 53 (2005) 202."
25. "H. Schulz, M. Baranska, H.-H. Belz, P. Rösch, M.A. Strehle, J. Popp, Vib. Spectr. 35 (2004) 81."
26. "H. Schulz, M. Baranska, R. Quilitzsch, W. Schütze, G.J. Lösing, J. Agric. Food Chem. 53 (2005) 3358."
27. "M. Baranska, H. Schulz, S. Reitzenstein, U. Uhlemann, M.A. Strehle, H. Krüger, R. Quilitzsch, W. Foley, J. Popp, Biopolymers 78 (2005) 237."
28. "H. Schulz, B. Schrader, R. Quilitzsch, B. Steuer, Appl. Spectr. 56 (2002) 117."
29. "R. Withnall, B.Z. Chowdhry, J. Silver, H.G.M. Edwards, L.F.C. de Oliveira, Spectrochim. Acta A 59 (2003) 2207."
30. "B. Schoefs, Trends Food Sci. Tech. 13 (2002) 361."
31. "H. Schulz, M. Baranska, R. Baranski, Biopolymers 77 (2005) 212."
32. "R. Baranski, M. Baranska, H. Schulz, Planta 222 (2005) 448."
33. "H.G.M. Edwards, D.W. Farwell, L.F.C. de Oliveira, J.-M- Alia, M. L. Hyaric, M.V de Ameida, Anal. Chim. Acta 532 (2005) 177."
34. " B. Schrader, H. Schulz, M. Baranska, G.N. Andreev, C. Lehner, J. Sawatzki, Spectrochim. Acta A 61 (2005) 1395."
35. "M. Baranska, H. Schulz, Analyst 130 (2005) 855."
36. "R. Baranski, M. Baranska, H. Schulz, P.W. Simon, T. Nothnagel, Biopolymers 81 (2006) 497."

37. “M. Baranska, H. Schulz, L. Christensen, J. Agric. Food Chem. 54 (2006) 8995.”
38. “A. Czepa, T. Hofmann, J. Agric. Food Chem. 51 (2003) 3865.”
39. “A. Czepa, T. Hofmann, J. Agric. Food Chem. 52 (2004) 4508.”
40. “D.G. Crosby, N. Aharonson, Tetrahedron 23 (1967) 465.”

Inline monitoring of structural quality and thermal conductivity of plastics in the hot extrusion process by means of infrared thermography

Peter Meinlschmidt, Jochen Aderhold and Friedrich Schlüter

Fraunhofer-Institute for Wood Research (WKI),
Bienroder Weg 54E, D-38108 Braunschweig

Abstract In a joint project called "Sensoren und Auswertestrategien zur autonomen Überwachung von kontinuierlichen Kunststoffprozessen" (KontiSens), the Fraunhofer Institute for Chemical Technology (ICT), the WKI, and partners from industry work on the development of sensors and evaluation strategies for the autonomous monitoring of continuous plastics production processes. The task of the WKI is to develop a monitoring technology based on infrard imaging for the production of insulating materials by hot extrusion.

Keywords: Thermography, thermal conductivity, insulating materials, image processing, hot extrusion.

1 Introduction

Hot extrusion is a widespread production process for plastics products with a cross-section which is constant lengthwise. The raw material is melted and pushed through the extrusion tool with a speed in the range of one metre per minute. Extrusion gives a very smooth surface and is able to process brittle materials such as expanded polystyrene. However, changes in the composition of the raw materials and variations in temperature and pressure can result in structural defects such as air inclusions or in an inhomogeneous distribution of material parameters such as thermal conductivity.

When the product leaves the extrusion tool, heat is dissipated by heat flows from the interior to the surfaces. The heat flow pattern in defective areas is different from that in good parts of the structure, if the defects differ in thermal conductivity and/or thermal capacity from the faultless material. This is especially true for air inclusions and density fluctuations. The different heat flows are mirrored in the temperature distribution on the product's surface. These temperature patterns and consequently the defects can be made visible with an infrared camera (thermography). Since infrared thermography is an imaging technique, many established procedures and algorithms from conventional image processing for automatic defect recognition can be adopted.

Furthermore, the thermal conductivity of the material can be characterized by means of thermography if it is subjected to a sequence of laser pulses. The laser pulses heat up the insulating material locally and generate a characteristic temperature profile. After the pulse, horizontal and vertical heat flows broaden the temperature profile and decrease its peak height.

2 Theory

The idea of thermography for structural quality control is to generate temperature differences between "good" and "bad" regions which can subsequently be detected by infrared imaging. The flow of heat in solid matter in the absence of internal heat sources is described by Fourier's law:

$$\nabla(\nabla\kappa T)) = \frac{\partial T}{\partial t}$$

with the heat diffusivity κ defined by

$$\kappa = \frac{\lambda}{\rho C_{sp}}$$

where λ is the thermal conductivity, ρ the mass density, and C_{sp} the specific heat capacity. In order to have heat flows ($\nabla T \neq 0$), one needs a change of temperature in time ($\partial T/\partial t \neq 0$). A change of temperature in time can conveniently be achieved by letting cool down the material which was heated in a preceding production step (passive heat flow

thermography). The monitoring of material coming out of an extrusion machine is a typical example for this method.

For a laser beam with intensity distribution I(x,y) moving in x direction at speed v with radial symmetry and diameter d, the maximum temperature in the irradiated area is given by [1]

$$T_{max} = T_0 + \frac{\epsilon}{2\lambda\pi d} \iint\limits_A \frac{I(u,v)e^{-P_n[r-(x-u)]}}{r}\, du\, dv$$

where T_0 is the environment temperature and ϵ the absorbtivity of the material. The Peclet number P_n is defined by

$$P_n = \frac{2dv}{\kappa}$$

The dimensionless variables u and v are the coordinates x and y divided by the beam diameter. The denominator of the integrand r is given by

$$r = \sqrt{(x-u)^2 - (y-v)^2}$$

It can be easily seen that the maximum temperature is inversely proportional to the thermal conductivity. If all other parameters are kept constant, monitoring the maximum temperature is sufficient to discover any changes in thermal conductivity.

Another way to do this is to observe the evolution of temperature over time. For a Dirac pulse with specific energy Q_0 in J/m^2, the surface temperature as a function of time is given by [2]

$$T(t) = T_0 + \frac{Q_0}{2\sqrt{\pi\kappa t}}$$

By fitting a appropriate function to the observed temporal evolution of the laser spots, κ can be obtained.

If the thermal pulse meets an interface between materials with different values of κ,the pulse is partially reflected with the reflection coefficient given by

$$R = \frac{1 - \sqrt{\frac{\kappa_2}{\kappa_1}}}{1 + \sqrt{\frac{\kappa_2}{\kappa_1}}}$$

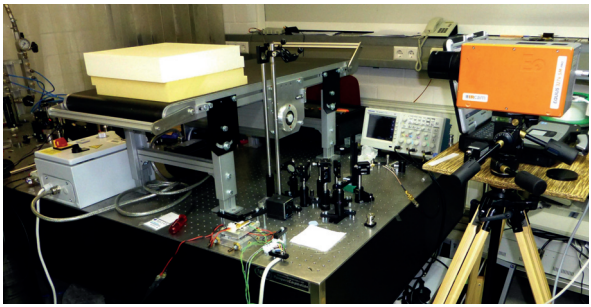

Figure 18.1: Setup used for the first experiments

This allows again for finding structural inhomogeneities in the direction of the laser beam which would change the surface temperature as a function of time in the described way.

3 Experimental

A first set of experiments was executed in co-operation with the Laser Zentrum Hannover e. V. on ready-made samples at room temperature. The aim of these experiments was to check if temperature profiles generated by laser beams can be recorded with an infrared camera and automatically extracted by image processing with sufficient precision.

In order to simulate the transport through the extrusion machine, a small conveyor belt was adjusted to have a transport velocity of 3 metres per minute. A pulsed solid state laser with a wavelength of 960 nm and a maximum power of 25 W was used to thermally excite the samples while they were moving along the laser beam on the conveyor belt. Pulse rate and spot diameter were 1 Hz and 1 cm, respectively. An infrared camera manufactured by IRCAM GmbH (Erlangen, Germany) recorded thermal images of the excited samples. In such a way, thermal signatures of up to four laser spots on the samples could be registered. The camera had an infrared detector made in InSb technology with 512 x 640 pixels with a noise equivalent detection threshold of 15 mK. It was operated at rate of 25 frames per second. The setup is illustrated in figure 18.1. The amount of heat absorbed depended strongly on the colour of the sample.

Figure 18.2: Passive thermography using the extrusion machine

A certain white material showed a temperature rise of only 2.5 K whereas some other (greenish) material was already melted in the centre of the laser spots.

A second set of experiments was carried out using the extrusion machine of Fraunhofer ICT in Pfinztal, Germany (figure 18.2). The objective was to check if structural inhomogeneities in the extruded material can be seen by passive heat flow thermography.

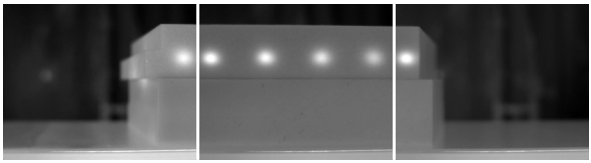

Figure 18.3: Typical infrared image from the initial, middle and final section of the series (right to left)

4 Image Processing for Data Extraction

The aim of the image processing part of the work was to write an algorithm which can extract the spatial intensity profiles of the laser spots over time automatically. This is of course necessary in the final application of the method, but even in the development stage it is not feasible to extract the information manually since every single measurement has typically more than 200 frames. For the sake of robustness, the algorithm should get as much information as possible from the image series itself. Only the following assumptions were made:

- The laser spots are brighter than their immediate surrounding, but not necessarily the brightest items in the image.
- The laser spots are moving through the field of view from left to right at constant speed and with constant distance.
- The laser spots are more or less round.

A typical infrared image series has an initial section, when the object under inspection enters the field of view, a middle section, and the final section, when the object leaves the field of view. Figure 18.3 shows one image for each section. The laser spots are clearly visible and show decreasing intensity from the left part of an image to the right part, as expected.

Of course it is much easier to identify the spots in the middle section of the series. However, in the test measurements of the development stage this section represents only a small part of the complete series. Concentrating on the middle section would thus lead to a huge loss of information. Consequently, the extraction algorithm uses the middle section in a first run to identify preliminary information of the peaks with respect to position, gray value, and size.

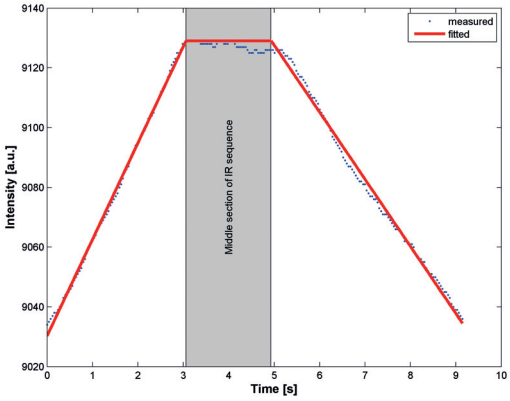

Figure 18.4: Measured and fitted mean intensities of an image series for the estimation of begin and end of the middle section

These information is then extrapolated to the complete series in order to help identifying the spots in every single image.

Thus, the first step of the work is to find the begin and the end of the middle section. For this purpose, the algorithm calculates the average intensities for the single images as a function of time. In the middle section the average intensity is more or less constant while it increases in the initial phase and decreases in the final phase. By fitting a trapezoidal function to the data, the middle section can be identified (figure 18.4). In the second step the average of the frames in the middle section over time is calculated and subtracted from the series in order remove the background. A typical image after background removal is shown in figure 18.5. The laser spots are not averaged out completely since the number of frames is too small, but the important thing is that the intensity in the spot region oscillates over time due to the movement of the spots whereas it is constant in the rest. This can be used to identify the upper and lower boundary of the region where the spots are.

In particular, the algorithm uses the PARAFAC method to analyse the temporal behaviour of the pixels over time. PARAFAC is similar to the better known Principal Component Analysis (PCA), but calculated

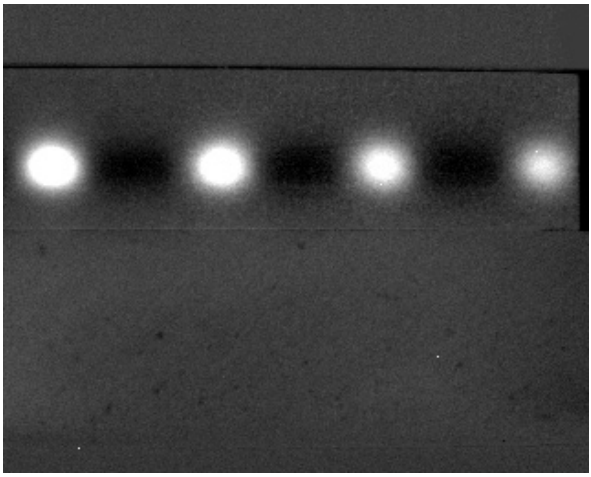

Figure 18.5: Typical image after background removal

in a different way. Whereas PCA diagonalises the covariance matrix, PARAFAC minimizes the error matrix. The result for the third component is shown in figure 18.6. The region of the moving spots is now determined by calculating the maximum of each row and fitting a Gauss profile to the result. Only this part of the image is considered in the subsequent calculations.

The next step is to segment the laser spots by a simple gray value threshold obtained by Otsu's method. In order to remove parasitic objects from the resulting binary image, elongated objects are identified and removed. After this, the image is morphologically opened, and only those objects are kept which exceed the average object size.

By this means the algorithm can find almost every peak. However, it sometimes misses a peak close to the right edge of the image and sometimes finds an object which is not a peak. This is a consequence of the decrease in spot intensity on the way through the field of view. But a simple linear fit to the estimated spot positions over time allows not only the identification of missing spots and outliers, but also calculating an individual region of interest for each single spot. Within these regions of interest, the spots can again be identified by thresholding, but with much better results due to the smaller area.

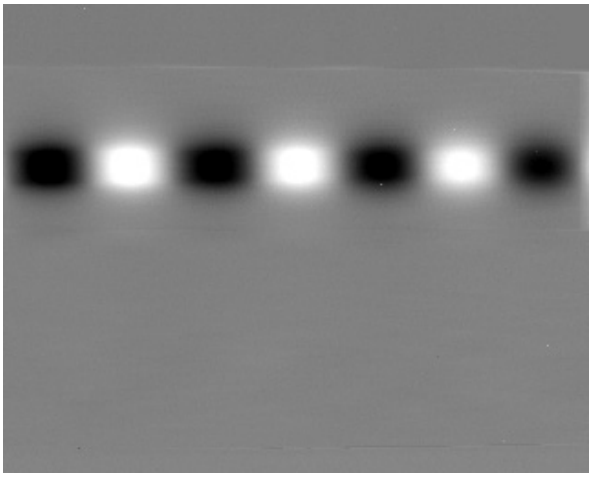

Figure 18.6: Third PARAFAC component of the time dependent iniensities of each pixel

Using this methods, the spot positions within the complete series can be found and used for the final step, the extraction and storage of the two-dimensional intensity profiles around the spots.

5 Results

A typical result from passive thermography using the extrusion machine is shown in figure 18.7. The structure shown in the image is most likely due to unwanted density inhomogeneities. Figure 18.8 shows a typical intensity profile of a peak. The raw data are displayed in the left part while smoothed data are shown in the right part. Smoothing was achieved again using the PRAFAC algorithm assuming a three-dimensional model (two spatial coordinates, one time coordinate).

Peak intensities as a function of frame number are exemplarily shown in figure 18.9. It can be seen that the curves for four peaks are close to each other whereas two peaks have higher intensities. It is not yet clear if this is due to changes in heat diffusivity or in laser power.

Figure 18.7: Inhomogeneities in extruded material in the infrared image

6 Summary and Conclusion

It was shown that structural inhomogenities in extruded plastics can be found using passive heat flow thermography. Furthermore, the intensity profiles of laser induced hot spots can be recorded with infrared imaging and extracted automatically with sufficient precision. In the forthcoming phases of the project, both passive thermography and laser stimulation will be carried out inline using an extrusion machine. Furthermore, thermal properties will be measured by standard methods and compared against the results of thermal stimulation by laser.

References

1. G. R. B. E. Römer and J. Meijer, "Metal surface temperature induced by moving laser beams," *Optical and quantum electronics*, vol. 27, no. 12, pp. 1397–1406, 1994.
2. D. P. Almond and P.-M. Patel, *Photothermal Science and Techniques*. London, UK: Chapman and Hall, 1996.

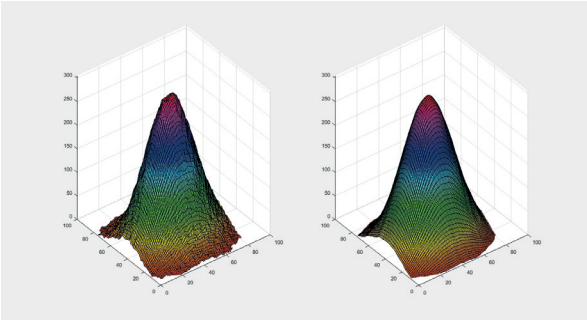

Figure 18.8: Typical peak form with raw data (left) and smoothed data (right)

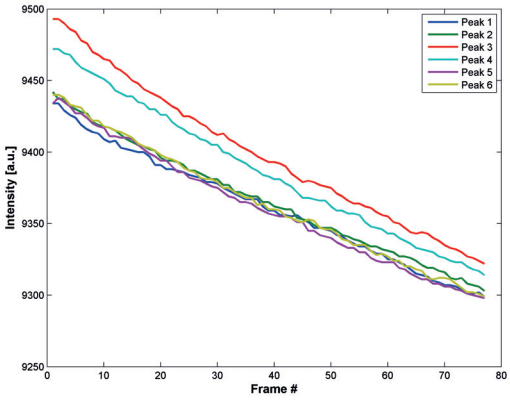

Figure 18.9: Typical peak intensities as a function of frame number

Hyperspectral imaging based approach for monitoring of microplastics from marine environment

Giuseppe Bonifazi[1] and Roberta Palmieri[1] and Silvia Serranti[1] and Cristina Mazziotti[2] and Carla Rita Ferrari[2]

[1] Dipartimento di Ingegneria Chimica Materiali Ambiente
Sapienza – Università di Roma
Via Eudossiana, 18 00184 Rome, Italy
[2] Oceanographic Structure Daphne
ARPAE Emilia Romagna
V.le Vespucci, 2 47042 Cesenatico (FC),Italy

Abstract The possibility to develop a sensor based procedure in order to monitor plastic presence in the marine environment was explored in this work. More in detail, this study was addressed to detect and to recognize different types of microplastics coming from sampling in different sea areas adopting a new approach, based on HyperSpectral Imaging (HSI) sensors. Moreover, a morphological and morphometrical particle characterization was carried by digital image processing. Morphological and morphometrical parameters, combined with hyperspectral imaging information, give a full characterization of each investigated particle, concurring to explain all the transportation, alteration and degradation phenomena suffered by each different polymer particle. Obtained results can represent an important starting point to develop, implement and set up monitor strategies to characterize marine microplastics. Moreover, the procedure developed in this work is fast, not expensive and reliable, making its utilization very profitable.

Keywords: Hyperspectral imaging, microplastics, marine environment.

1 Introduction

Plastic debris in the marine environment are considered as a global problem: the increasing plastic production and its improper disposal when plastics become wastes heighten the build-up of these materials in the environment, contaminating especially oceans [1]. Recent studies have shown as five large-scale accumulation regions of floating plastic debris exist in the oceans [2]. Once in the sea water, plastics undergo degradation processes (i.e. UV radiation, atmosphere oxidative properties and seawater hydrolytic properties) that induce their fragmentation, leading to an increasing amount of small plastic particles, called microplastics. Microplastics are defined as "plastic particles smaller than 5 m" according to the International Research Workshop on the Occurrence, Effects and Fate of Microplastic Marine Debris in September 2008 [3]. Due to their small size, microplastics can easily enter in the marine food chain, being ingested by marine biota [4]. The persistence of microplastics in the sea fauna (i.e. mussels) has implications for predators, including birds, crabs, starfish, predatory whelks [5] and humans. Microplastics can absorb persistent bio-accumulative and toxic compounds from seawater before being transferred to the marine organisms as food [6] causing health problems in each step of the food chain. In particular, toxic chemicals as persistent organic pollutants (POPs) are endocrine disruptors that produce dangerous effects. Moreover, some researches highlighted as the microplastics presence in the circulatory system can impede blood flow, damaging cardiac activity and tissues vascularization but also the ingested plastic can abrade the gut cavity [7]. Several studies indicate microplastic toxicological risks but concentrations in nature are not well known [8]. In order to obtain a better knowledge of the impacts due to the microplastics presence in the marine environment, most studies have focused on quantifying their abundance. A detailed monitoring of microplastics from the sea water is thus needed, in order to assess a reliable evaluation of the marine situation in terms of plastic presence [4]. Indeed, quantitative measurements are important in order to assess the risk and to realize monitoring purposes, but also to allow temporal and spatial comparison of pollutants [9]. In this work, the classical digital imaging and the innovative hyperspectral imaging approaches were combined in order to obtain a full classification of marine microplastic samples. A mor-

phological and morphometrical analysis by digital images was coupled with the investigation of hyperspectral images that allows to identify, to recognize and to classify different types of polymers starting from known reference plastics. The fulfillment of a fast and non-destructive monitoring system, able to characterize and recognize different types of marine microplastics, can make the successive operations, aiming to prevent and combat their production and spread, much more effective and targeted.

2 Materials and methods

2.1 Samples

The investigated marine microplastic samples were collected from the Mediterranean Sea along the northern coast of the Adriatic Sea and off the coast of Forlì-Cesena and Ferrara areas, during two measurement campaigns carried out by ISPRA (Italian National Institute for Environmental Protection and Research) and ARPAE (Regional Agency for Prevention, Environment and Energy of Emilia-Romagna, Italy), in October 2014 in the framework of the international project called Derelict Gear Management System in the Adriatic Region – DeFishGear, funded with the financial assistance of the IPA Adriatic Cross-Border Cooperation Programme [10]. The investigated area was divided in two transects, Cesenatico and Porto Garibaldi, and a station called Lido di Volano: the sampling was carried out in the first few meters of water column where the particles tend to float on the surface. For each transect, samples were collected at 500 m, 3 km, 10 km and 20 km off shore, while for the sampling at Lido di Volano station microplastics were taken at 10 km off shore. The collected number of microplastic samples was 643: 469 in the Cesenatico transect, 153 in the Porto Garibaldi transect and 21 in the Lido di Volano station. According to the particle shape, samples were classified as filaments, films, foam, fragments, granules, other, pellets and uncategorized. For the analyses shown in this work, fragment class was selected and 293 samples were thus analyzed (Table 19.1).

The 293 microplastic samples were grouped in about 10–12 particles and they were acquired by digital camera and hyperspectral imaging working in the short wave infrared range (1000–2500 nm) (Figure 19.1).

Table 19.1: Total and percentage number of microplastic samples belonging to the fragment class in each transect/station.

	Cesenatico Transect	Porto Garibaldi Transect	Lido di Volano Station
N° fragments	186	97	10
% fragments	64	33	3

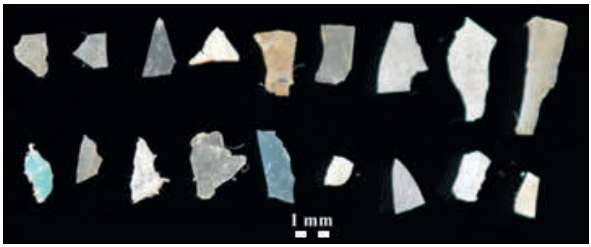

Figure 19.1: Marine microplastics from the Cesenatico Transect sample.

In total 25 digital images for morphological and morphometrical analysis and the corresponding 25 hyperspectral images were thus obtained.

In order to recognize the polymer type of each microplastic fragment, the SWIR spectra of virgin polypropylene (PP), virgin polyethylene (PE) and virgin polystyrene (PS) samples coming from an industrial production plant were used as references. Comparing the particle spectra with those of known reference polymers, the identification of polymer constituting the analyzed microplastic samples was performed. A classification model was also built and validated applying it on hyperspectral images rapresenting marine microplastics (Figure 19.2).

2.2 Image acquisition systems

Both classical and hyperspectral imaging acquisitions were carried out at "RawMaLab" (Raw Materials Laboratory) of the Department of Chemical Engineering, Materials & Environment (Sapienza – University of Rome, Italy). In order to acquire digital images of microplastic samples for morphological and morphometrical analyses, a Nikon D5200 camera was adopted.

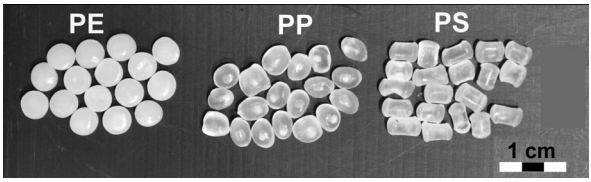

Figure 19.2: Virgin PP, PE and PS samples used as references for the identification of microplastics.

The 25 digital images thus obtained were processed adopting the Image-Pro Plus software by Media Cybernetics. More in detail, the following parameters were measured for each fragment particle:

- Area (mm^2);
- Axis major (mm);
- Axis minor (mm);
- Diameter max (mm);
- Diameter min (mm);
- Diameter mean (mm);
- Perimeter (mm);
- Roundness as the ratio between the perimeter^2 and the $4\pi \cdot area$;
- Fractal dimension.

The 25 hyperspectral images were acquired using the SISUChema XL^{TM} Chemical Imaging Workstation (Specim, Finland) (Figure 19.3), equipped with an ImSpector^{TM} N25E imaging spectrograph (Specim, Finland) working in the short wave infrared range (SWIR: 1000–2500 nm). The analytical station is controlled by a PC unit equipped with specialized acquisition/pre-processing software (Chemadaq^{TM}), to handle the different units and the sensing device constituting the platform and to perform the acquisition and the collection of spectra. Images were acquired scanning line by line the samples, with a width of 320 pixels and a number of frames variables according to the desired length. Calibration for black and white references was automatically performed.

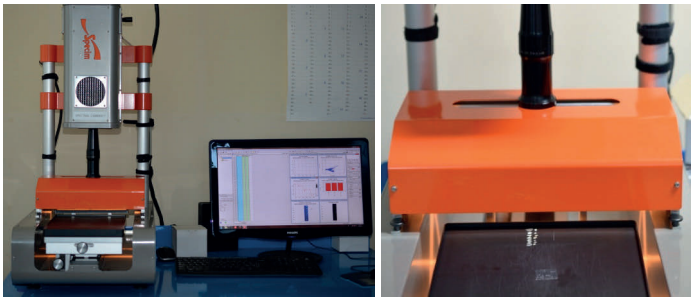

a b

Figure 19.3: An overview of the SISUChema XL^{TM} chemical imaging workstation (Specim, Finldand) (a) and a detail of the macro lens acquiring microplastics (b).

The analyzed images were acquired with a macro lens and a field of view of 10 mm. 256 wavelengths were collected. Spectral data analyses were performed using PLS-Toolbox^{TM} under Matlab® environment.

The procedure for the analysis of the hyperspectral data was developed in different steps. First of all, Regions Of Interest (ROIs) were selected on each acquired particle in the hyperspectral images in order to obtain SWIR spectra to compare with plastic reference spectra for a preliminary sample identification. Starting from reference plastics of known type, Principal Component Analysis (PCA) was applied in order to perform an exploratory analysis, useful to set the classes for the further classification purpose. In order to build a classification model, Partial Least-Squares Discriminant Analysis (PLS-DA) was adopted and it was validated applying the model to the hyperspectral images.

3 Results

3.1 Morphological and morphometrical analysis

Morphological and morphometrical results obtained for the investigated microplasic particles are reported in Table 19.2, in terms of mean, standard deviation, max and min values.

Table 19.2: Total and percentage number of microplastic samples belonging to the fragment class in each transect/station.

	Cesenatico				Porto Garibaldi				Lido di Volano			
	Mean	**St.Dev**	**Max**	**Min**	**Mean**	**St.Dev**	**Max**	**Min**	**Mean**	**St.Dev**	**Max**	**Min**
Area (mm^2)	3.68	4.28	24.65	0.27	3.01	4.52	37.07	0.26	5.04	7.83	26.11	0.47
Axis Max (mm)	2.75	1.51	8.74	0.82	2.24	1.29	7.54	0.15	2.75	1.97	7.3	0.84
Axis Min (mm)	1.51	0.81	4.99	0.31	1.38	0.92	6.57	0.3	1.74	1.28	4.73	0.74
Diameter Max (mm)	2.83	1.59	9.74	0.83	2.29	1.31	8.19	0.68	2.58	1.88	6.96	0.98
Diameter Min (mm)	1.35	0.72	4.42	0.11	1.23	0.8	5.29	0.22	1.5	1.15	3.99	0.56
Diameter Mean (mm)	1.87	0.95	5.49	0.56	1.63	0.98	6.76	0.56	2.02	1.47	5.61	0.77
Perimeter (mm)	7.79	4.2	22.89	2.13	6.4	3.91	27.77	1.92	8.12	5.69	21.18	2.75
Roundness	1.78	2.8	39.21	0.36	1.45	0.35	3.22	1.08	1.59	0.82	3.91	1.17
Fractal Dimension	1.06	0.02	1.13	1.01	1.07	0.04	1.41	1.02	1.06	0.02	1.1	1.02

Area ranges between 0.26 and 37.07 mm^2, Axis Major between 0.15 and 8.74 mm, Axis Minor varies between 0.30 and 6.57 mm, Diameter max ranges between 0.68 and 9.74 mm, Diameter min between 0.11 and 5.29 mm while Diameter mean is between 0.56 and 6.76 mm, Perimeter ranges between 1.92 and 27.77 mm. The mean value for the Roundness is around 1.6: only a very elongated particle was found in the Cesenatico transect with 39.21 as Roundness value. The Fractal Dimension of the analyzed microplastics ranges between 1.01 and 1.41 with a mean value of 1.06.

Starting from the mean diameter of each analyzed particle, according to the ranges set by literature for microplastics [11–13] as small (0.35–1.00 mm), medium (1.00–4.75 mm) and large (4.75–5.00 mm), samples were grouped and counted (Figure 19.4). Medium particles are the most abundant in each transect/station, followed by the small ones. Large microplastics, with mean diameter ranging between 4.75-5.00 mm and more than 5.00 mm, are very few and they are concentrated into the Cesenatico transect mainly. The low presence of large particles is probably due to all the degradation processes occurred in the sea water (i.e. UV radiation and seawater wavy motion) inducing their fragmentation.

3.2 Hyperspectral imaging

In order to collect microplastic particle spectra, some ROIs (Regions of Interest) were selected in each of the 25 HSI acquisitions (Figure 19.5).

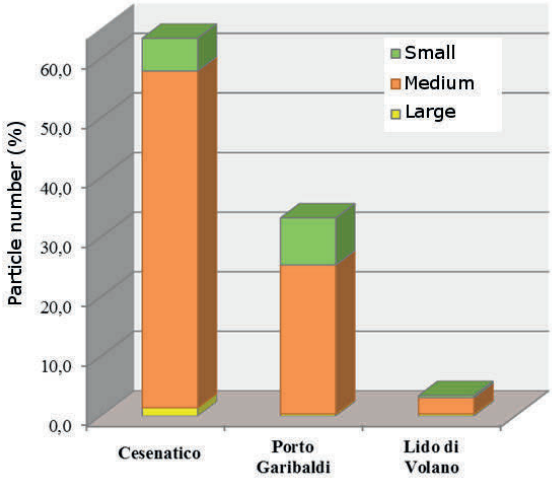

Figure 19.4: Microplastic particle number (%) grouped in small, medium and large per each transect/station according to [11–13].

The analyzed microplastics were classified as PE, PP and PS: 245 are PE particles, 32 are made of PP and 1 particle is constituted by PS (Table 19.3). 14 particles are not identified because of their black color that makes difficult the spectrum recognition. In Cesenatico transect, samples are more affected by the presence of unidentified particles. After the preliminary analysis that allowed to identify the most abundant polymers in the microplastic samples, a procedure for automatic recognition of plastic types was carried out.

Table 19.3: Number of particles and percentage values constituted by PE, PP, PS and unidentified (NI) for each transect/station.

	Cesenatico		**Porto Garibaldi**		**Lido di Volano**	
	n°particles	%	n°particles	%	n°particles	%
PE	160	86	75	77	10	100
PP	12	6	20	21	0	0
PS	0	0	1	1	0	0
NI	14	8	1	1	0	0

Figure 19.5: An example of the ROI selection on a SWIR-HSI image.

The acquired raw and preprocessed spectra of PP, PE and PS references plastics are reported in Figure 19.6. After pre-processing stage, PCA was applied as exploratory data analysis. The analysis of the score plot allows to identify three different groups according their spectral signature.

In Figure 19.7 score plot PC1-PC2 obtained after removal of some border pixels is shown. All the pixels represented in Figure 19.7 were selected as training dataset for PLS-DA model.

The obtained values of Sensitivity and Specificity are shown in Table 19.4.

Table 19.4: Sensitivity and specificity for the PLS-DA model built for the recognition of microplastic types: PP, PE and PS.

	Sensitivity		**Specificity**	
	Calibration	*Cross validation*	*Calibration*	*Cross validation*
PE	1.000	1.000	0.999	0.999
PP	1.000	1.000	1.000	1.000
PS	1.000	1.000	1.000	1.000

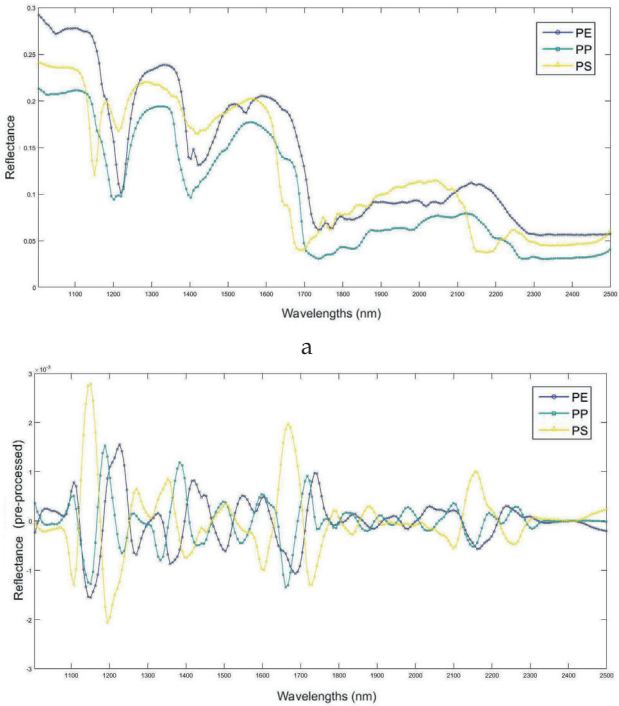

Figure 19.6: Raw spectra (a) and preprocessed spectra (b) after the application of 2nd derivative and mean center algorithms of PE, PP and PS reference samples.

The results in terms of "class most probable" predictions are shown in Figure 19.8: the class with the highest probability is assigned to each pixel in the image. Obtained results are very good, allowing to distinguish 3 PP particles, 9 PE particles and 1 PS particle clearly.

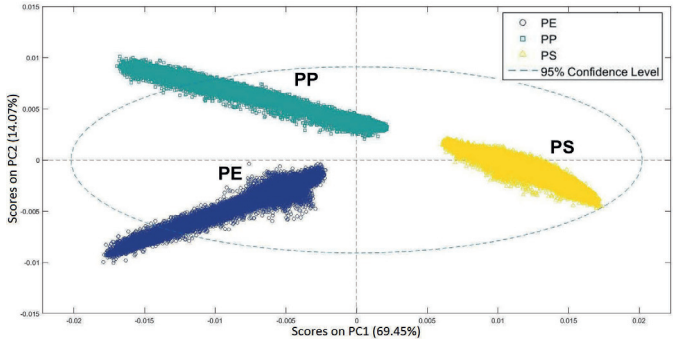

Figure 19.7: PC1-PC2 score plot as resulting after pixels removal from the training dataset in the SWIR wavelength field (1000–2500 nm).

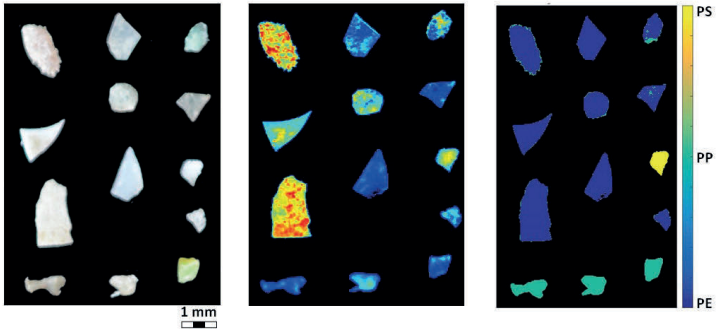

a b c

Figure 19.8: Digital image (a), hyperspectral image (b) and prediction map (c) obtained as result of the PLS-DA classification model.

4 Conclusions

The study was carried out to obtain a full characterization of marine microplastics in order to monitor their presence in the marine environment. A morphological and morphometrical analysis was combined with SWIR-HSI analysis in order to evaluate particle sizes, shapes and polymer types. Moreover, a SWIR-HSI based procedure was developed in order to implement an automatic recognition of PP, PE and PS in a

hyperspectral image representing microplastic particles coming from sea water. More in detail, Partial Least-Squares Discriminant Analysis, after application of Principal Component Analysis, was used to build a model able to recognize/classify PP, PE and PS particles. The proposed HSI-based approach presents a lot of advantages: it is reliable, fast and non-destructive, allowing low-cost analysis. As confirmed by the results, the HSI can be profitably utilized to clearly discriminate PP, PE and PS in the analyzed samples. Obtained results can be considered as an important starting point to develop monitor strategies for marine microplastic characterization. Further studies will be devoted to correlation between morphological and morphometrical parameters and the different degradation processes of marine microplastics related to the polymer types.

Acknowledgment

Special thanks are due to Federica Maffei for her contribution in morphological and morphometrical analysis as part of her master thesis in Environmental Engineering at Sapienza University of Rome.

References

1. M. Claessens, L. Van Cauwenberghe, M. Vandegehuchte, and C. R. Janssen, "New techniques for the detection of microplastics in sediments and field collected organism," in *Marine Pollution Bulletin, Vol. 70*, 2013.
2. A. Cózar, M. Sanz-Martín, E. Martí, J. González-Gordillo, B. Ubeda, J. Gálvez, X. Irigoien, and C. Duarte, "Plastic accumulation in the mediterranean sea," in *PLoS ONE, Vol. 10(4)*, 2015.
3. C. Arthur, J. Baker, and H. Bamford, "Proceedings of the international research workshop on the occurrence, effects, and fate of microplastic marine debris," in *NOAA Technical Memorandum NOS-OR&R30*, 2008 Washington, 9–11 September 2009.
4. V. Hidalgo-Ruz, L. Gutow, R. C. Thompson, and M. Thiel, "Microplastics in the marine environment: A review of the methods used for identification and quantification," in *Environmental Science & Technology, Vol. 46(6)*, 2012.
5. P. S. Petraitis, "Immobilisation of the predatory gastropod, nucella lapillus, by its prey, mytilus edulis," in *Biological Bulletin, Vol. 172 (3)*, 1987.

6. R. Lenz, K. Enders, C. Stedmon, D. Mackenzie, and T. Nielsen, "A critical assessment of visual identification of marinemicroplastic using raman spectroscopy for analysis improvement," in *Marine Pollution Bulletin , Vol. 100*, 2015.
7. R. Thompson, B. Browne, A. Dissanayake, T. Galloway, and D. Lowe, "Ingested microscopic plastic translocates to the circulatory system of the mussel, mytilus edulis (l.)," in *Environmental Science & Technology, Vol. 42 (13)*, 2008.
8. K. Enders, R. Lenz, C. Stedmon, and T. Nielsen, "Abundance, size and polymer composition of marine microplastics $\geq$ 10 µm in the atlantic ocean and their modelled vertical distribution," in *Marine Pollution Bulletin, Vol.100*, 2015.
9. T. M. Karlsson, H. Grahn, B. van Bavel, and P. Geladi, "Hyperspectral imaging and data analysis for detecting and determining plastic contamination in seawater filtrates," in *Journal of near infrared spectroscopy, Vol. 24*, 2016.
10. http://www.defishgear.net/.
11. P. G. Ryan, C. J. Moore, J. A. van Franeker, and C. L. Moloney, "Monitoring the abundance of plastic debris in the marine environment," in *Philosophical Transactions of the Royal Society B Vol.364*, 2009.
12. R. C. Thompson, Y. Olsen, R. P. Mitchell, A. Davis, S. J. Rowland, A. W. G. John, D. McGonigle, and A. E. Russell, "Lost at sea: where is all the plastic?" in *Science, Vol. 304*, 2004.
13. M. Eriksen, L. Lebreton, H. Carson, M. Thiel, C. Moore, J. Borerro, F. Galgani, P. Ryan, and J. Reisser, "Plastic pollution in the world's oceans: More than 5 trillion plastic pieces weighing over 250,000 tons afloat at sea," in *PLoS One, Vol.9 (12)*, 2014.

NIR-SWIR-Hyperspectral-Imaging supported surface analysis for the recovery of waste wood

Frank Hollstein[1], Enrico Pigorsch[2], Burkhard Plinke[3], Markus Wohllebe[1], Peter Meinlschmidt[3]

[1] RTT Steinert GmbH
02763 Zittau, Hirschfelder Ring 9, Germany
[2] PTS Papiertechnische Stiftung
01809 Heidenau, Pirnaer Straße 37, Germany
[3] WKI Fraunhofer Institute for Wood Research
38108 Braunschweig, Bienroder Weg 54E, Germany

Abstract Cascading of waste wood requires a concept for recovery of solid timbers from deconstruction as a source of clean and reliable secondary feedstock for new wood and wood-based products. An essential requirement for the re-use of wood is a sufficient quality of the near-surface areas that must be free of contaminations like coatings or any wood preservatives. Due to the absence of industrial established automatic testing and sorting methods the possible potential for material re-use of recovered wood in the sense of cascading is not utilized so far. Hyperspectral-Imaging (HSI) is a promising method to improve the situation. In the study on hand results according to detection accuracy and limitations of NIR-SWIR-HSI are presented. As input material solid waste wood (e.g. different kinds of hard wood, soft wood, wood with paint or other coatings, particle boards, and medium density fibreboards) obtained from deconstructions is considered. First, the spectral structures of some different kinds of wood and contamination are examined. Desired are the so-called fingerprints according to significant characteristics in the spectra. The results have been incorporated in a database as training set. For classification tasks some decision trees based on PLS-DA (Partial Least Squares Discriminant Analysis) were exploited. These decision trees are then passed to an industrial NIR-SWIR-Hyperspectral-Imager for generating chemical images of the contaminated wood samples. Results

of some sorting experiments are presented. The aim of the tests was to find the limits for sorting throughput and purity. The tests revealed that the spectral differences are mostly large enough for automatic wood classification and sorting operations even at presence of inorganic wood preservatives. In this case the detectability and accuracy of classification depends much on preservative concentrations.

Keywords: NIR-SWIR-HSI, recovered wood, sorting, recycling.

1 Introduction

Cascading use can be defined as the efficient utilization of resources by using residues and recycled materials to extend total biomass availability within a given system [1, 2]. For wood this mainly requires a concept for recovery of solid timbers from deconstruction or demolition waste as a source of clean and reliable secondary feedstock for new wood and wood-based products [3–5]. The re-use of wood presupposes a sufficient quality of the near-surface areas that must be free of contaminations like plastics, coatings or any wood preservatives that are used to extend the service life by preventing biodegradation.

Due to the absence of industrial established automatic testing and sorting methods the potential for material re-use of recovered wood in the sense of cascading is not utilized so far as it would be possible. Waste wood of lower grades e.g. often is a mixture of wood particles with contamination and/or coatings and pure wood particles which could be used as high grade wood – if there were suitable techniques to sort out the particles of lower grade. In addition to cascading use of wood, the production of energy (or better conversion) by combustion of demolition wood – as it is still the preferred method to exploit this kind of waste in most countries – needs an effective presorting. When e.g. CCA treated wood is burned, the resulting ash contains high amounts of chromium, copper and arsenic, may posing an environmental problem [6].

Crucial steps in the re-use of used wood are detection and sorting out of above mentioned contaminated items. Powerful in-line methods are required to perform the task. A holistic solution with industrial importance is not known until now. The separation of treated wood and

other contaminations from clean wood is today mainly based on visual, mechanical, magnetic or gravity sifting techniques and is done at different steps along the recycling chain. Sensor based automatic sorting techniques are the only solution to achieve higher levels of recovery and quality of waste wood from demolition and to increase considerably the proportion of a high value material use of waste wood.

NIR spectroscopy (NIRS), especially the NIR imaging techniques (Hyperspectral-Imaging (HSI) [7]), is best suited for the automated on-line sorting of high volumes of waste wood. It has a high discrimination power for organic contaminations and the necessary measuring speed and spatial resolution. In a recently published review on applications of NIRS in wood science and technology it is pointed out that on-line or at-line monitoring in wood industry is in a starting position. It is desired to bring HSI into industrial applications for the wood branch as next step [8].

The study on hand aims to support this task. Results according to detection accuracy and limitations of NIR-SWIR-HSI are presented. As input material solid waste wood (e.g. different kinds of hard wood, soft wood, wood with paint or other coatings, particle boards, and medium density fibreboards) obtained from deconstruction is considered. Spectral measurements on the input materials in reflection mode have been incorporated into a database as training set. For classification tasks some decision trees based on PLS-DA (Partial Least Squares Discriminant Analysis) were exploited. These decision trees are then passed to an industrial NIR-SWIR-Hyperspectral-Imager for generating chemical images of the contaminated wood samples. Discussion of some sorting experiments sums up the study.

2 State of the art

Matured timbers are divided into different quality groups, in Germany [9] e.g. into classes AI (quasi natural wood), AII (used wood without preservative treatments and without halogenated organic coatings), AIII (used wood with halogenated organic coatings but without preservative treatments), and AIV (preservative treated wood, except PCB waste wood). Unification of quality groups AII and AIII is in a state of thinking about. A fifth group, referred to as PCB waste wood,

falls within the scope of PCB/PCT (polychlorinated biphenyls / terphenyls) waste and should not be considered here deeper because it is quantitatively not of importance for re-use.

For recycling the reclaimed wood of categories AI, AII, and after extensive detachment of coatings also AIII can be used. The two biggest challenges are therefore the detection of halogenated organic coatings (mainly PVC coatings) that must be removed from AIII wood for re-use and the detection of wood preservatives to classify a piece as AIV wood, respectively. For these tasks, there are a number of "classical" analysis methods like Ion-Mobility Spectrometry (IMS) [10, 11], Thermography [12], Color Indicator Techniques [13], Laser-Induced Breakdown Spectroscopy (LIPS), and X-ray Fluorescence Analysis (RFA) [6, 14, 15]. The main disadvantages of all of these analytical methods are that they are either not space-resolved or too slow for on-line operations. One promising method for both space-resolved and fast on-line detection is NIRS in connection with digital image processing. This combination is called Hyperspectral [16] or Chemical Imaging, respectively.

As standalone method, NIRS for detection of wood preservatives is known for over two decades [17]. The non-destructive method has been refined continuously [18–25]. But NIRS only provides a mean spectrum (average measurement) of a sample, irrespective of the area of the sample scanned. As the spectra collected are averaged to provide a single spectrum, the information on spatial distribution of constituents within the sample is lost. The development of NIR-HSI, which combines NIRS with digital imaging, enables both spatial (localization) and spectral (identification) information to be obtained simultaneously. HSI thus have the potential of describing distribution of constituents within a sample. More than one decade after the release of the first affordable digital cameras that were sensitive enough for the NIR spectral range [26], HSI also appeared in the focus of wood research in a laboratory scale [27–30]. The complex of waste wood analysis by HSI regarding detection of contaminations and preservatives is a quite new field of applications and so far just applied on AIII and AIV wood [29, 30].

The investigations in [29, 30] employed a NIR-SWIR-HyperspectralImager[1]. A key objective of the research was to find out whether NIR-SWIR-HSI is suitable to differentiate between various organic and inorganic wood preservatives qualitatively as well as quantitatively. As one result it could be claimed that it was possible to classify the spectra according to the chemical compositions at the surfaces of investigated sample/preservative combinations. Surprisingly this was found to be true not only for organic preservatives, but also for most inorganic ones. An explanation for this finding could be the formation of chemical reactions between the inorganic preservatives and the wood constituents, leading to significant changes in the spectral fingerprints. In at least the case of Cu(II) sulfate the preservatives could be detected quantitatively by NIR-SWIR-HSI.

3 Experimental details and results

For extension and curing of the findings in [29, 30] the authors have launched two experimental series, one in laboratory scale (WKI study) and the other in industrial scale (RTT/PTS study). The first series considered the detection ability of VIS-invisible organic wood preservatives while the second ones deals with measuring of real world waste wood samples of different types and with different contaminations. In both cases the same kind of NIR-SWIR hyperspectral camera (RED-EYE 2.2) has been used. The RED-EYE 2.2 camera from inno-spec GmbH (Germany) is sensitive in the wavelength range from 1.100 nm to 2.200 nm. It consists of a transmission grating based spectrometer and a cooled extended InGaAs detector with 256 x 320 pixels (spectral x spatial). The full-frame-rate is 330 Hz. In both series spectral images were acquired using the push-broom imaging principle [7]. Samples were scanned over conveyor belts with 50 and 200 cm width at speeds of 10 and 200 cm/sec, respectively. For illumination halogen lamps powered with 250 W have been used. Due to the slower conveyor belt speed of

[1] By agreement, the NIR portion of the electro-magnetic spectrum is typically defined as ranging from the end of the visible spectrum (around 800 nm) to 1.700 nm. The SWIR portion of the spectrum ranges from 1.700 nm to around 2.500 nm. A uniform definition does not exist until today. Sometimes the whole region from 800 to 2.500 nm (12.500 to 4.000 cm-1; 120 to 375 THz) is called NIR range.

the laboratory equipment (10 cm/sec to 200 cm/sec for the industrial equipment) the sample illumination was stronger in the first experimental series.

3.1 WKI study – laboratory scale

PCP (pentachlorophenole) and Lindane (hexachlorcyclohexan) were the most widely used wood preservatives in the 1960s until the 1980s. Lindane was also used as insect repellent (insecticide). Much demolition wood from this period is surface contaminated with these toxic ingredients. The preservatives are invisible and have been usually applied in rather low concentrations, typically in the range of milligrams of the agent (without solvent) per kg of wood.

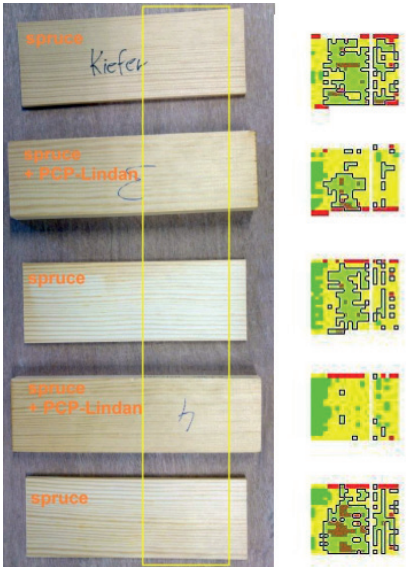

Figure 20.1: (left) Scene with wood samples; three without (from top No. 1, 3, 5), and two with PCP-Lindane treatment (from top No. 2, 4); the yellow box marks the area under evaluation. (right) Results of classification by principal component PC 1, areas probably without treatment are marked by black frames (see text).

For simulation planed samples of spruce wood, artificial treated with PCP-Lindane together with untreated reference samples were placed on a plywood background (Fig. 20.1, left) and scanned using the above mention experimental setup for series one. A region-of-interest of the scene comprising approx. 35 % of each sample's width (yellow box) was taken from the HSI and analyzed using the commercial software Evince from Prediktera (Sweden).

PCP-Lindane and other organic wood preservatives like tolylfluanid or tebuconazole show specific absorptions in a NIR range between approx. 1.300 nm and 2.100 nm [30]. Therefore it is useful to limit the range for HSI data evaluation to these bands and, if possible, to exclude the strong absorption band of water at around 1.900 nm. A principal component analysis (PCA) of the hyperspectral image in Fig. 20.1 (left) was carried out for the wavelength range 1.600 nm to 1.800 nm. Figure 20.2 shows the loadings for the first PC (principal component) – the maxima near 1600 nm correspond to expected absorptions typical for PCP-Lindane around this wavelength [30].

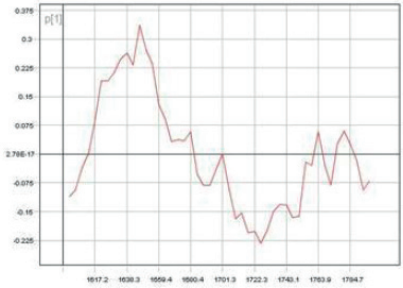

Figure 20.2: Loadings plot of PC 1 for wavelength range 1.600 nm to 1.800 nm.

The scatter plot of the PCs 1 and 2 (Fig. 20.3) shows no significant clusters, which could be used for a clear treated/untreated classification of the samples. But according to Fig. 20.2 information of the PCP-Lindane content can be expected in PC 1, and the values of PC 1 are suitable to classify the pixels in the HSI. At a certain level of the PC 1 value the segmentation correlates well with the apriority classification of the samples. Dark green dots in Fig. 20.3 and black borders in Fig. 20.1 (right) mark the pixels with probably low PCP-Lindane content.

From evaluation of series one it can be concluded that PCP-Lindane in the samples has been detected because wood species and surface properties were the same for all pixels in the HSI. However, these results are valid only for these conditions and material and the classification model must be re-calibrated for new wood material and/or other preservatives. Therefore, the findings can be considered just as a first step – there are several problems to solve for using NIR-SWIR-HSI to classify wood pieces by their content of organic preservatives and to apply this for industrial sorting applications.

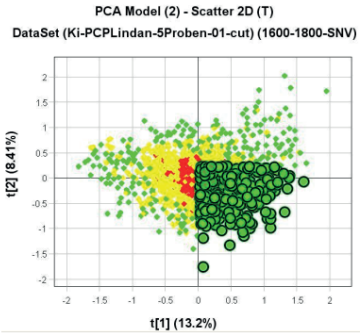

Figure 20.3: Scatter diagram of PC1 / PC2, classified pixels marked as in Fig. 20.1 (right).

3.2 RTT/PTS study – industrial scale

The objectives of second experimental series were the development and testing of NIR-SWIR-HSI measuring methods for the detection of contaminations on surfaces of real world waste wood. Especially in focus have been contaminations with paint or other coatings, wood products others than solid wood, e.g. MDF (medium density fibreboard), and extensive investigations on different wood material types, e.g. soft and hard wood. To be not beyond the topic and scope of the OCM conference only the developed methodology for the detection and separation of different types of wood materials that are painted with different coatings is described subsequently.

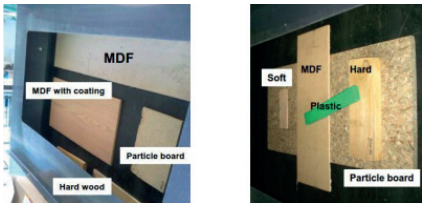

Figure 20.4: Samples of different wood material types and an extra piece of plastics (right, PS).

From a typical mixture of demolition waste wood randomly five different samples were chosen: hard wood (LH), soft wood (NH), wood with paint or other coatings (FA), particle board (SPAN) and medium density fibreboard (MDF), respectively (Fig. 20.4).

On the basis of a previously created database of well pre-treated spectra a multi-stage hierarchical PLS-DA decision tree as it is self-explanatory shown in Fig. 20.5 has been applied.

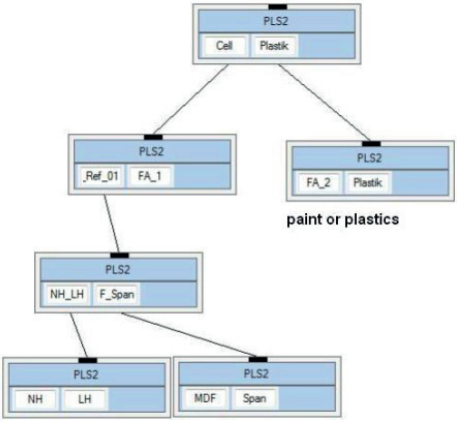

Figure 20.5: Multi-stage hierarchical PLS-DA classification tree.

This decision tree is then passed to an industrial sorting machine with a NIR-SWIR-Hyperspectral-Imager for generating chemical images of the wood samples (Fig. 20.6).

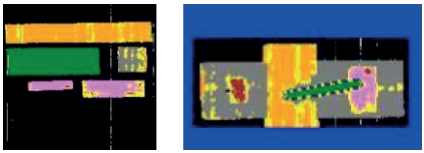

Figure 20.6: Chemical Image of samples from Fig. 20.4.

From Fig. 20.6 it can be slightly derived, that by applying of appropriate procedures of MIA (multivariate image analysis [7,29]) a separation of items and thus an automatic sorting by NIR-SWIR-HSI support is a capability.

4 Summary and Conclusions

The main objective of the study on hand was the extension and curing of published results in [29,30] that deal with the applicability of NIR-SWIR-HSI for the fast detection and sorting of waste wood treated with wood preservatives. It should also be studied whether the developed recognition procedures can satisfy high requirements from industry in terms of accuracy and robustness. Demonstrated on example of toxic PCP-Lindane (today banned as preservatives, however much often present in waste wood from demolition) it was found, that in case of VIS-invisible impregnated waste wood with rather low concentrations of the agent a classification is anyway possible. Nevertheless, much attention must be payed on spectroscopy, chemometrics and multivariate image analysis, respectively. Some pre-skills about the spectral structure of the possible types of impregnation seem to be essential. The perceptibility of organic coatings on different timber and wood products was proven on an industrial scale. As a side effect, even the type of wood material can be determined by NIR-SWI-HSI support.

Acknowledgments

The authors wish to acknowledge the support of the European Commission to the WoodWisdom-Net Research Programme, Project CaReWood (WWN-2013-99), as frame within this research has been conducted.

References

1. T. Sirkin and M. ten Houten, "The cascade chain: A theory and tool for achieving resource sustainability with applications for product design," *Resources Conservation and Recycling*, vol. 10, no. 3, pp. 213–276, 1994.
2. M. W. Vis, U. Mantau, and B. A. (Eds.), "Study on the optimised cascading use of wood," *No 394/PP/ENT/RCH/14/7689. Final report, Brussels, 337 pages*, 2016.
3. L. Sokka, K. Koponen, and J. T. Keraenen, "Cascading use of wood in Finland - with comparison to selected EU countries," *RESEARCH REPORT, VTT-R-03979-15*, 2015.
4. M. W. Vis, P. Reumerman, and S. Gaertner, "Cascading in the wood sector," *Final report, Project No. 1741 (Netherlands Enterprise Agency (RVO))*, 2014.
5. L. Dammer, C. Bowyer, E. Breitmayer, A. Eder, S. Nanni, B. Allen, M. Carus, and R. Essel, "Mapping Study on Cascading Use of Wood Products," *Technical Report, WWF*, 2016.
6. K. Yasuda, M. Tanaka, and Y. Deguchi, "Basic evaluation of sorting technologies for CCA treated wood waste," *Proc. ENVIRONMENTAL TOXICOLOGY 2006, WIT Transactions on Biomedicine and Health*, pp. 319–327, 2006.
7. H. F. Grahn and P. Geladi (Ed.), *Techniques and Applications of Hyperspectral Image Analysis, ISBN 978-0-470-01086-0*, 2005.
8. S. Tsuchikawa and H. Kobori, "A review of recent application of near infrared spectroscopy to wood science and technology," *Journal of Wood Science*, vol. 61, no. 3, pp. 213–220, 2015.
9. "Verordnung ueber Anforderungen an die Verwertung und Beseitigung von Altholz - Altholzverordnung - AltholzV (Ordinance of Requirements for the Recovery and Disposal of Waste Wood - Waste Wood Ordinance), § 2 Terminologies, in German," 2015.

10. W. Schroder, G. Matz, and J. Kubler, "Fast detection of preservatives on waste wood with GC/MS, GC-ECD and ion mobility spectrometry," *Field Analytical Chemistry and Technology*, vol. 2, no. 5, pp. 287–297, 1998.
11. G. A. Eiceman and Z. Karpas and H. H. Hill (Jr.), *Ion Mobility Spectrometry, Third Edition. CRC Press, ISBN 978-1-4398-5997-1*, 2014.
12. P. Meinlschmidt and B. Plinke, *Optical Infrared Detection of Contaminations in Recovered Wood, Proc. Sensor Based Sorting, Aachen*, 2012.
13. G. Sawyer and M. Irle, *Development of color indicator techniques to detect chemical contamination in wood waste for recycling. WRAP, Project Code WOO0034, ISBN 1-84405-204-4*, 2006.
14. H. M. Solo-Gabriele, T. G. Townsend, D. W. Hahn, T. M. Moskal, N. Hosein, J. Jambeck, and G. Jacobi, "Evaluation of XRF and LIBS technologies for on-line sorting of CCA-treated wood waste," *Waste Management*, vol. 24, no. 4, pp. 413–424, 2004.
15. A. R. Hasan, J. Schindler, H. M. Solo-Gabriele, and T. G. Townsend, "On-line sorting of recovered wood waste by automated XRF-technology. Part I: Detection of preservative-treated wood waste," *Waste Management*, vol. 31, pp. 688–694, 2011.
16. L. Wang and Ch. Zhao, *Hyperspectral Image Processing. National Defense Industry Press, Beijing and Springer-Verlag Berlin Heidelberg, ISBN 978-3-662-47456-3*, 2016.
17. R. Feldhoff, T. Huth-Fehre, and K. Cammann, "Detection of in-organic wood preservatives on timber by near infrared spectroscopy," *J. Near Infrared Spectroscopy*, vol. 31, pp. 171–173, 1998.
18. C.-L. So, S. T. Lebow, L. H. Groom, and T. G. Rials, "The Application of Near Infrared (NIR) Spectroscopy to Inorganic Presevertive-Treaded Wood," *Wood and Fiber Science*, vol. 36, no. 3, pp. 171–173, 1998.
19. C.-L. So, S. T. Lebow, T. L. Eberhardt, L. H. Groom, and T. F. Shupe, "Application of Near Infrared Spectroscopy to Preservative-Treated Wood," *Proc. Advanced Biomass Science and Technology for bio-based Products, Beijing, China*, pp. 125–130, 2007.
20. A. Sandak, J. Sandak, W. Pradzynski, M. Zborowska, and M. Negri, "Near Infrared Spectroscopy as a Tool for Characterization of Wood Surface," *FOLIA FORESTALIA POLONICA, Series B*, vol. 40, pp. 31–40, 2009.
21. M. Schwanninger, J. Rodrigues, and K. Fackler, "Near Infrared Spectroscopy as a Tool for Characterization of Wood Surface," *Journal of Near Infrared Spectroscopy*, vol. 19, no. 5, pp. 287–308, 2011.

22. R. Stirling, "Near-infrared spectroscopy as a potential quality assurance tool for the wood preservation industry," *The Forestry Chronicle*, vol. 89, no. 5, pp. 59–63, 2013.

23. S. Tsuchikawa and M. Schwanninger, "A Review of Recent Near-Infrared Research for Wood and Paper (Part 2)," *Applied Spectroscopy Reviews*, vol. 48, no. 7, pp. 560–587, 2013.

24. M. Bouslamti, M. Irle, C. Belloncle, V. Salvador, S. Hulot, B. Caron, and E. Qannari, "Classification of treated wood using Fourier transform near infrared spectroscopy and multivariate data analysis," *International Wood Products Journal*, vol. 4, no. 2, pp. 68–74, 2013.

25. E. Pigorsch, G. Gaertner, F. Hollstein, and P. Meinlschmidt, "Sorting of Waste Wood by NIR Imaging Techniques," *Proc. Sensor-based Sorting, Aachen*, pp. 127–136, 2014.

26. E. Herrala and J. Okkonen, "Imaging Spectrograph and Camera Solution for Industrial Applications," *International Journal of Pattern Recognition and Artificial Intelligence*, vol. 10, pp. 43–54, 1996.

27. A. Thumm, M. Riddell, B. Nanayakkara, J. Harrington, and R. Meder, "Near infrared hyperspectral imaging applied to mapping chemical composition in wood samples," *Journal of Near Infrared Spectroscopy*, vol. 18, no. 6, pp. 507–515, 2010.

28. G. Bonifazi, S. Serranti, G. Capobianco, G. Agresti, L. Calienno, R. Picchio, A. L. Monaco, U. Santamaria, and C. Pelosi, "Study of consolidating materials applied on wood by hyperspectral Imaging," *Proc. SPIE 98620I-1*, 2016.

29. D. Mauruschat, J. Aderhold, B. Plinke, and P. Meinlschmidt, "NIR Spectral Imaging for the In-line Detection of Preservatives in Recovered Wood, Proc. OCM 2015, Karlsruhe, ISBN 978-3-7315-0318-7," 2015, pp. 113–122.

30. D. Mauruschat, B. Plinke, J. Aderhold, J. Gunschera, P. Meinlschmidt, and T. Salthammer, "Application of near-infrared spectroscopy for the fast detection and sorting of wood-plastic composites and waste wood treated with wood preservatives," *Wood Science Technology*, vol. 50, pp. 287–297, 2016.

THz imaging for recycling of black plastics

Andries Küter, Stefan Reible, Thomas Geibig, Dirk Nüßler, Nils Pohl

Fraunhofer FHR, Fraunhoferstr. 20, 53343 Wachtberg

Abstract This paper presents the development of a novel line-camera device in the THz-domain which is capable of measuring minute differences in broadband spectral fingerprints of non-conducting materials. The primary focus is sorting black plastics in industrial recycling contexts, where large scale sorting of different types of black plastics remains a challenge. The system operates from 84 GHz to 96 GHz. As the relevant plastics exhibit no specific absorption lines in this frequency range, a broadband approach is necessary to accumulate slight differences in dielectric properties into enough entropy that a machine learning algorithm can be trained to differentiate between different materials even in the presence of contaminants such as flame retardants, color pigments and dirt. Preliminary results suggest that the blackValue® THz sensor system is capable of achieving these goals.

Keywords: THz imaging, black plastics.

1 Introduction

The thermal recycling of plastics is no longer seasonable for modern industrialized countries; in 2011 unfortunately around 56 % of all plastic scrap in Germany was recycled thermally. These 3 million tons of plastic scrap are an untapped treasure for a resource deficit country. Non perfect sorting results in low-grade plastics granulate which in turn can only be used to produce lower grade products. Today recycled material is mixed together with new raw material to create a high-grade granulate. The drawback of this procedure is, that for 1 t recycled material between 2 t and 3 t new material is needed. For a 100 % material recycling strategy a mono-fraction sorting system is the key to success.

Modern recycling systems use hyperspectral camera systems to distinguish between different plastics. Because of the high carbon content in black plastics most of the photons of optical detector systems are absorbed. For efficient sorting systems new sensor concept are needed.

Test measurements and publications in the last few years have shown the feasibility of plastics separation using THz systems. While plastics can be identified using their distinct absorption lines in the infrared region, in the lower THz region they exhibit no such behavior [1]. To choose the optimum frequency range, a selection of machine learning algorithms was trained with test data sets acquired in the first phase of the project. Test series with commercial systems show that better sorting results can be realized using higher frequency ranges as well as more bandwidth for the analysis. With a limited number of classes, test sets and a first prototype algorithm a probability between 85 % and 95 % for identification was realized [2]. The chosen frequency range is a compromise between the need to design an economically priced commercial system while simultaneously achieving a high purity level.

2 Measurement principle

The blackValue® THz line scan camera system utilizes a stepped-frequency continuous-wave (SFCW) approach. The transmitter illuminates the particles traveling on the conveyor belt with 128 equally spaced frequency lines in the lower THz region ranging from 84 GHz to 96 GHz, yielding a usable bandwidth of 12 GHz. The receiver uses a quadrature mixer to downconvert the received signal to an intermediate frequency (IF) of 3 MHz. This IF signal is sampled using a 25 MSps analog to digital converter (ADC). Only a single sample is captured per frequency step as the information contained in the quadrature signal (I, Q) allows for the reconstruction of instantaneous magnitude $\mathrm{A}(t)$ and phase $\Phi(t)$ of the received signal: $\mathrm{A}(t) = \sqrt{\mathrm{I}(t)^2 + \mathrm{Q}(t)^2}, \Phi(t) = \arctan \mathrm{I}(t)/\mathrm{Q}(t)$. The sample instant has to be timed precisely as a sample captured early or late exhibits artifacts stemming from the system still settling on the current frequency or the most recent frequency step, respectively.

While this approach requires careful timing, it enables us to decrease the acquisition time for a complete measurement frame (128 frequency steps, arbitrary number of sets of 4 channels multiplexed in time) to less that 1.4 ms.

Unless filtered in the analog domain, each sample contains the noise integrated over the whole analog bandwidth of the ADC, thus raising the overall noise floor and decreasing system signal-to-noise ratio (SNR). This effectively puts a lower bound on the IF frequency as lower frequency filters require larger components, making designs below 1 MHz impractical. At higher IF frequencies, sampling jitter leads to inaccuracies in the captured phase of the IF signal.

As the system is intended for recycling applications, a large bandwidth of additives, material mixes and impurities is to be expected in the measured goods. A simple fingerprint analysis comparable to absorption line evaluation is not sufficient to achieve satisfactory sorting results in the used frequency domain. Therefore, a machine learning algorithm is trained to perform the actual classification based on the captured and normalized magnitude and phase information. The principle was demonstrated in [3], while [2] performed measurements using the precursor of our current system.

3 Hardware concept

Typical conveyor belt speeds for this application are in the range of 2.5 to 3 m/s. As the system should be able to provide a resolution of around 1 line per millimeter a measurement-rate of up to 3000 measurements per second has to be achieved. This yields in a interval of less than 333 μs available for the generation of all frequency-lines in the desired range and the synchronous sampling of the down-converted RX-signal, which contains the permittivity-characteristics of the probe. In the following subsections the frontend and the backend of the system will be described in more detail.

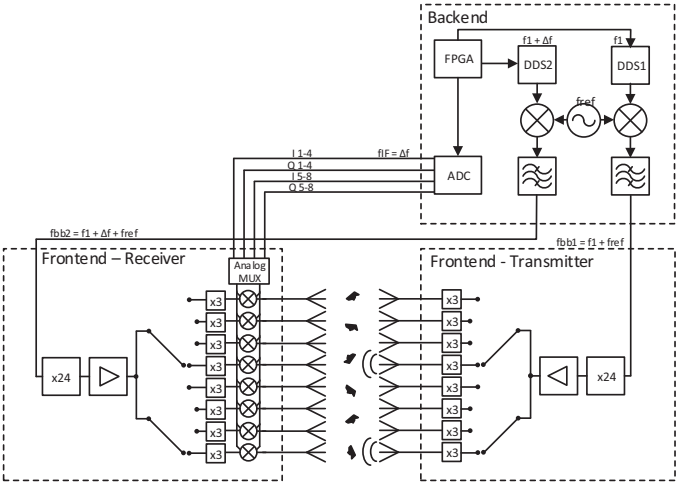

Figure 21.1: Schematic illustration of blackValue® THz Imager.

3.1 Frontend

The frontend consists of an array of transmitters and receivers which can be cascaded in a modular fashion to allow for the required number of channel (or pixels). This is evident of the desired covering width of conveyor belt and the resulting resolution of the THz camera-system. The measurement method is similar to a simplified multi-port heterodyne vector network analyser. The fundamental idea of the blackValue® system is illustrated in figure 21.1.

Two Direct Digital Synthesis (DDS) chips generate fast stepped frequency ramps f_1 from 160 MHz up to 320 MHz in which the ramps are slightly shifted in frequency Δf with respect to each other. Both ramps are upmixed using the same low noise reference oscillator f_{ref} and the resulting conversion product is bandpass filtered. This baseband signals f_{bb} with frequency range from 1,16 to 1,33 GHz feeds into the transmitters and receivers. Using a chain of multipliers the baseband signal gets upconverted further to an RF signal band ranging

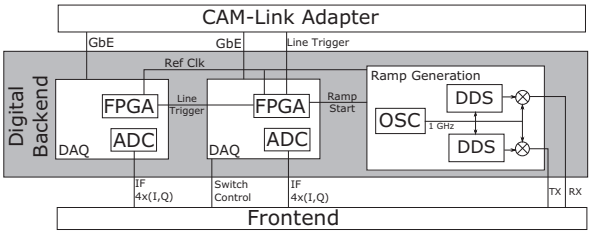

Figure 21.2: Schematic overview of the digital backend of the blackValue® sensor.

from 27,8 to 31,9 GHz. This signal then feeds an RF switch. The switch is controlled by the backend and allows to switch the transmitting antennas in Time Division Multiplex (TDM). this way, a trade-off between optimal performance and economical costs can be achieved.

The spatial separation between active antennas allows for insignificant crosstalk and multiple usage of the 30 GHz LO reduces the system costs. After passing the switch the RF signal gets multiplied again to the targeted millimetre-wave band ranging from 83, 5 GHz to 95, 8 GHz and is radiated by the transmitter antennas. After passing a plastic flake the affected millimetre-wave signal gets detected by the receiver antennas. The receiver involves an IQ-mixer, which converts the affected signal together with the slightly shifted LO signal down to an Intermediate Frequency (IF) of 3 MHz. Depending on the currently active pixel, the corresponding IF signal is switched by an analog multiplexer to the backend.

3.2 Backend

The digital backend of the presented THz camera system consists of multiple distinct subsystems as depicted in figure 21.2 and described in the following paragraph.

A ramp generator board serves as source for local oscillator signals for the receive- and transmit-path as well as source of a digital reference clock signal for synchronous operation with the data acquisition (DAQ) boards. These Signals are generated by a 1 GHz reference-oscillator that drives a clockmanager IC which in turn drives two DDS-ICs.

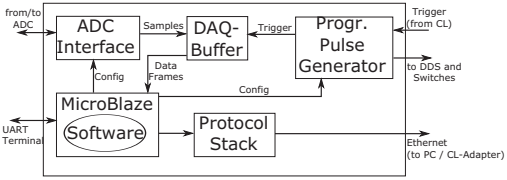

Figure 21.3: Block-diagram of the DAQ-FPGA firmware. Timing- and performance-critical tasks are implemented in hardware-modules which are controlled by software running on an embedded microcontroller.

Coherent sampling of the downconverted RX Signal is accomplished by a set of 8-channel DAQ boards. As for every pixel a complex quadrature IF signal is captured, each of these boards allows simultaneous sampling of 4 Pixels. By time-division multiplexing of 4 IF channels from the frontend, each DAQ board is capable of capturing 16 pixels of the scanline. Multiple DAQ boards can be combined to acquire scanlines containing more than 16 pixels, where one of these boards acts as a master device, controlling the signal-generator board and distributing a synchronous line-trigger signal to all slave DAQ boards as well as controlling the signal mutiplexers.

Figure 21.3 gives a schematic overview of the firmware-logic realized in FPGA-hardware on the DAQ boards. The control signals for sequencing the operation of the signal-generator, the RX/TX switches and the sample-buffer are generated by a programmable pulse generator, which is implemented in FPGA logic-ressources.

Different schedules for these control signals may be loaded to this pulse generator by software running on an embedded microcontroller (MicroBlaze^{TM}). Figure 21.4 illustrates the pattern of pixel-multiplexing and frequency switching as employed in the current version of the sensor. Each DAQ-device transfers its acquired stream of 16 pixels over a Gigabit-Ethernet link via UDP/IP-Packets. A seperate FPGA-based Camera-Link adapter-board bundles these streams for subsequent transmission via camera-link.

	t →			
channel 0	0	1	2	3
channel 1	4	5	6	7
channel 2	8	9	10	11
channel 3	12	13	14	15
frequency	f_0 f_1 ▪ ▪ ▪ f_{126} f_{127}	f_0 f_1 ▪ ▪ ▪ f_{126} f_{127}	f_0 f_1 ▪ ▪ ▪ f_{126} f_{127}	f_0 f_1 ▪ ▪ ▪ f_{126} f_{127}

Figure 21.4: 16 complex-valued pixels are multiplexed to 4 complex channels on the DAQ board.

As the imaging system is intended for industrial applications, serviceability and scalability are a primary concern. While earlier approaches [4, 5] depended on custom-machined housings comprising delicate waveguide structures, these expensive one-off parts are superseded in our current build-up by using commercially available launch connectors and individual printed circuit boards (PCBs) for each channel.

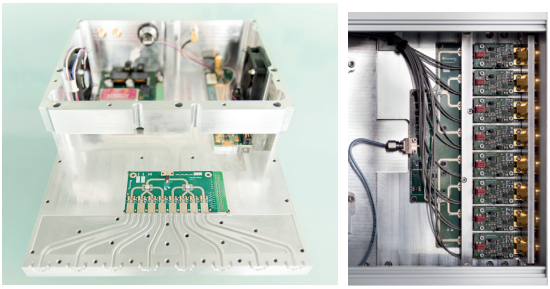

Figure 21.5: Left: Old frontend with machined waveguides. Right: New frontend using single channel PCBs and plug-in wave guide launch adaptors.

Earlier backends were tightly integrated with PCBs stacked in multiple layers. Although layers were functionally independent where possible, 30 GHz gain blocks and reference signal generation had to be placed on the bottom of the casing to facilitate thermal management. While this setup was used to successfully demonstrate the feasibility of our approach [2], it imposed limits on scalability with respect to the number of channels used.

To overcome these limitations, a more modular approach is neccessary. Our current system concept is centered around using a motherboard to distribute power and route all critical RF signals to a multitude of daughterboards. We opt for using PCIExpress-connectors as these provide well defined insertion and return loss specifications over a wide frequency range while as a consumer grade product being readily available at a low price. A basic set of daughtercards is used in the current system: The first one conditions the RF reference signal and controls the RF TDM switches in both the receive and the transmit frontend modules. A second daughtercard implements a 4 channel high pass filter bank for the measurement signals being captured from a single frontend module. This card is also used to control the RX TDM switches in the frontends.

System partitioning is driven by the need to perform a transmissive measurement, meaning the transmitter is situated on top of the conveyor opposing the receiver below. On an industrial scale conveyor, this necessitates cable trunks spanning multiple meters between the backend and the frontend. This limits the frequency distributed by the backend to the low GHz range.

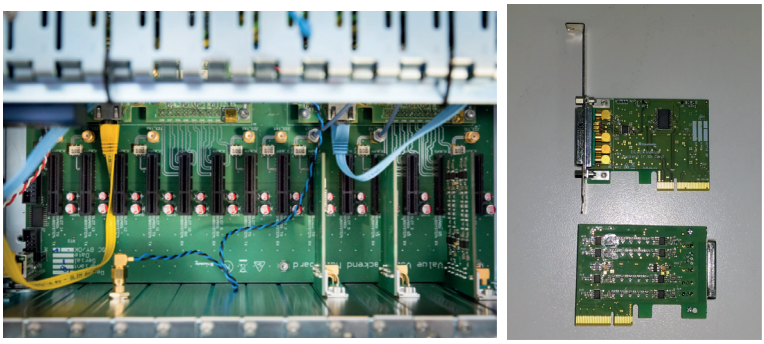

Figure 21.6: New modular backend in COTS case with plug-in cards.

Figure 21.7: Spectral fingerprints of different materials. Channels are oriented vertically while frequency increases from left to right. Top right: No specimen. Bottom right: Aluminium sheet, resulting in noise. Top left: 1 mm ABS sheet. Bottom left: 1 mm PP sheet. Areas containing distinguishing features are highlighted. Signals are intentionally overdriven to enhance visibility of features.

4 Results

To evaluate system performance, pure polymer samples are measured using the blackValue® camera. As the classification algorithm builds on a large database of scanned materials, a different approach is used to assure enough measurement entropy before conducting large scale training data acquisition. Plastic sheets measuring 150 mm ∗ 150 mm with a thickness of 1 mm are placed into the measurement aperture and the resulting spectral fingerprint is recorded. Normalization is performed using a reference measurement without a test specimen. The resulting spectral fingerprints are visualized in Fig. 21.7. Although the differences are quite small, they allow classification of the pure specimen.

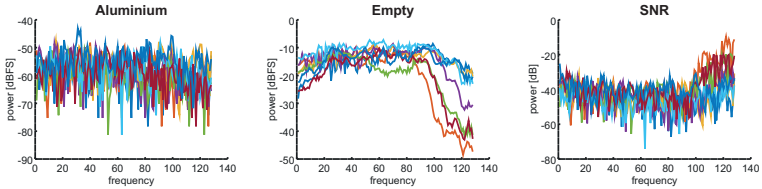

Figure 21.8: Signal-to-noise measurements. The first graph shows the system noise floor for each frequency line and channel. The second graph shows the reference measurement. The last graph shows the calculated system SNR.

The noise level of the receiver is measured using a 3 mm metal sheet isolating the transmitter and receiver. This is compared against the measurement without a test specimen. The difference of these measurements (in dB) defines the frequency and channel resolved system SNR. Fig. 21.8 shows the result of this evaluation. For frequencies up to 93.375 GHz (step 100), system SNR reaches $35 - 40$ dB. As the frequency increases further, some channels show degraded performance. This is to be expected as the 30 GHz switches used in the frontend exhibit insertion loss imbalances across channels at higher frequencies.

5 Future work

The final blackValue® system comprises the THz line scan camera as well as classification algorithms and a sorter that performs particle flow segmentation using an optical line scan camera. The next steps are integration of the THz sensor into the TableSort bench sorter developed by Fraunhofer IOSB and teaching the classifier developed by Fraunhofer IAIS using a wide range of real world particles, i.e., particles originating from recycling processes. Following successful integration, the sensor array will be extended to 32 complex channels (pixels) and integrated into the FlexSort large scale sorter. Additionally, we are working on implementing steeper and narrower IF filters which should further increase the system SNR.

6 Summary

A W-band THz line scan sensor array comprising 8 channels with a bandwidth of 12 GHz was realized. We demonstrated the fitness of the blackValue® THz sensor for the task of sorting black plastics by evaluating its RF performance and noise level.

References

1. Y.-S. Jin, G.-J. Kin, and S.-G. Jeo, "Terahertz dielectric properties of polymers," in *Journal of the Korean Physical Society, Vol. 49 No. 2*, August 2006.
2. C. Brandt, M. Kieninger, C. Negara, R. Gruna, T. Längle, A. Küter, and D. Nüßler, "Sorting of black plastics using statistical pattern recognition on

terahertz frequency domain data," in *7th Sensor-Based Sorting & Control 2016*, Aachen, Germany, February 2016.

3. K. Hein, D. Stein, M. Stadtschnitzer, M. Demming, and J. Küls, "Classification of polymers using gmm-ubm on high-frequency data," in *6th Sensor-Based Sorting & Control 2014*, Aachen, Germany, March 2014.
4. D. Nüßler, P. Warok, and N. Pohl, "High frequency line cameras for sorting applications," in *OCM 2015 2nd Conference on Optical Characterization of Materials*, Karlsruhe, Germany, March 2015.
5. D. Nüßler, R. Gruna, C. Brandt, A. Küter, T. Längle, M. Kieninger, and N. Pohl, "Innovative technologies as enabler for sorting of black plastics," in *WCNDT 2015 19th World Conference on Non-Destructive Testing*, Munich, Germany, June 2016.

IM Chapter IEEE GERMANY SECTION [KCM] Karlsruhe Center for Material Signatures KIT Karlsruhe Institute of Technology Fraunhofer IOSB

INTERNATIONAL CONFERENCE ON OPTICAL CHARACTERIZATION OF MATERIALS

Each material has its own specific spectral signature independent if it is food, plastics, or minerals. New trends and developments in material characterization have been discussed as well as latest highlights to identify spectral footprints and their realizations in industry.

CONFERENCE TOPICS:

- Food Inspection
- Plastic Recycling
- Waste Recycling
- Mineral Characterization
- Industrial Solutions
- Spectral Data Processing

The International Conference on Optical Characterization of Materials (OCM-2017) was organized by the Karlsruhe Center for Material Signatures (KCM) in cooperation with the German Chapter of the Instrumentation & Measurement Society of IEEE.

KCM is an association of institutes of the Karlsruhe Institute for Technology (KIT) and the business unit Automated Visual Inspection of the Fraunhofer Institute of Optronics, System Technologies and Image Exploitation (Fraunhofer IOSB).

ISBN 978-3-7315-0612-6
9 783731 506126 >

Gedruckt auf FSC-zertifiziertem Papier